Dynamics and Pattern Formation in Active Viscoplastic Droplets

July 2025

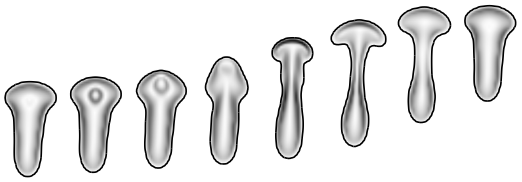

Maxim Marshall

Under the supervision of Pedro Cosme and Mazi Jalaal.

UvA

VU

Dynamics and Pattern Formation in Active Viscoplastic Droplets

UNIVERSITY OF AMSTERDAM

FluidLab
University of Amsterdam
Science Park 904
1098 XG Amsterdam, The Netherlands

Abstract

Pattern formation, dynamics, and compartmentalisation are fundamental to living systems. To explore their coupling, we study a reaction-diffusion-advection system confined to a deformable viscoplastic droplet, where active stresses arise from chemical concentration gradients. Given the system's strong nonlinearity and coupling, isolating inherent phenomena presents significant challenges. Here, we address this by constructing a minimal model that is capable of a broad range of dynamics: we retain only the lowest-order gradient terms in the active stress and develop a direct numerical simulation for the fully coupled system. Our simulations reveal a rich spectrum of behaviours, including droplet fragmentation, persistent network structures, pulsation, motility, stable non-circular shapes, and fingering instabilities. Focussing on the pulsatory motile state, we demonstrate that viscoplastic rheology stabilises the droplet and gives rise to persistent unidirectional motion.

to Julie

Contents

Chapter 1

Introduction

Pattern formation is a universal phenomenon, largely dominated by the study of convection. In that scenario, a temperature gradient causes a body of fluid to heat up, expand, and flow to a colder region, where it cools down, contracts, and sinks back to the warmer region, forming a pattern of rolls in the flow[1].

Convection forms patterns strikingly similar to reaction-diffusion systems, as both of these systems of partial differential equations (PDEs) are invariant under translation, rotation and reflection on an infinite plane[2]. Other such systems include the geometric hallucination patterns in the visual cortex, stripes and spots on animal skins, and nematic liquid crystals[2].

Further examples are to be found, some even of planetary length scales. Saturn exhibits a clear instance of pattern formation in its persistent hexagonal flow pattern located near its north pole[3]. It is considered an example of turbulent self-organisation, but the precise mechanism for the pattern's formation remains unknown[3].

Perhaps unsurprisingly, rich pattern dynamics are also characteristic of active or biological systems. Recent developments in the field of ecology allowed ecologists to explain regular pattern formation in real ecosystems using scale dependent feedback between organisms and their environment[4]. The combination of long range negative feedback (e.g. the depletion of a resource) and short range positive feedback (e.g. cooperating organisms) is key to the formation of patterns in these ecosystems. These components are to be identified with the long term inhibition and short range activation from the theory developed by Turing[5]. In his theory, Turing showed that diffusion can destabilize a homogeneous steady-state. This so called Turing instability was at the time unintuitive, as diffusion was seen to have only a stabilising effect. Wetlands, savannas, coral reefs, mussel beds, marsh tussocks, and intertidal mudflats all clearly display Turing patterns in one way or another[4].

In network theory, too, can we speak of pattern formation. Large, random networks that can facilitate the Turing instability were shown to have their nodes spontaneously

divide into activator-rich and activator-poor groups[6]. In fact, Othmer and Scriven observed that in the early stages of morphogenesis, an embryo would be best modeled by a multicellular network, as opposed to a continuous reaction-diffusion system[7]. Such a network has since been identified in the embryo of *Caenorhabditis elegans*[8,9].

In the realm of active and biological systems, certainly one of the most captivating phenomena to study is that of morphogenesis and histological dynamics in general, which serve as a motivation for the present work.

This thesis develops a framework for directly simulating mechano-chemical pattern formation in an active viscoplastic two-dimensional droplet through four interconnected parts.

Introduction to pattern formation. This part revisits foundational concepts of reaction-diffusion systems on a static substrate, introducing analytical methods for linear stability assessment. Moreover, we also detail the model for the chemical sector: the Brusselator.

Continuum mechanics of active systems. Here, the framework is extended by integrating mechanical stresses into the reaction-diffusion system—covering passive transport laws, active stresses, and non-Newtonian rheology.

Direct numerical simulations via Basilisk. Direct simulation of this coupled system appear to be unexplored in the literature. We address this gap by developing a model using the open-source PDE solver Basilisk[10]. Given the limited documentation for Basilisk, we present the implementation details pedagogically.

Confinement to a deformable droplet. Lastly, the active viscoplastic fluid will be confined to a two-dimensional deformable droplet having surface tension. Emergent phenomena will be explored; in particular, pulsatory and motile behaviour.

1.1 Formation of Patterns in Nature

In his late years, Alan Turing was formulating a novel mathematical framework for the formation of patterns in nature[11]. His works at the time aimed to elucidate the problem of phyllotaxis: the mechanism behind the arrangement of leaves on a plant[11]. It is in these works that Turing formulated his theory of morphogenesis on the basis of reaction-diffusion systems, published in 1952—two years prior to his death[5,11].

Shortly after the publication of the theory of morphogenesis, the biologist Claude Wardlaw had the following comment on it:[12]

> It will be appreciated that a theory, based essentially on laws of physical chemistry that must apply to every growing system, is of the kind that may well account for the general occurrence of certain organizational features in plants.

In this model, a system in a homogeneous state will indefinitely remain homogeneous (regardless of the shape of the mass). However, any instability in the dynamical

evolution of the system will cause the most minute fluctuations from this homogeneous state to develop into distinct states far removed from this equilibrium state[5]. Real systems are always subject to such fluctuations, and thus such departures from homogeneity are certain to occur spontaneously (in unstable configurations).

It is then appropriate to speak of self-organisation[13]. Turing based his theory on this feature, and went further to suggest the possibility that a minute examination of the organism just at the onset of instability but no earlier, will be conclusively telling of how it will develop in later stages of development[5]. The genius of his theory lies in showing that diffusion (usually regarded as a stabilising actor) can drive the system into a state of instability. This will be shown shortly.

Reasoning from experimental data about the shape forming of early-stage organisms implies that any polarity due to this shape forming is due to an asymmetric distribution of some scalar property, rather than, for example, to a definite orientation of asymmetric cells[14]. This scalar field is the concentration of a morphogen. The reaction-diffusion system no longer necessarily describes chemical reactions and Brownian diffusion of a chemical, but may model reaction through consumption and creation of molecules by cells, and diffusion by more elaborate transport behaviour through biological tissue[15].

The theory of morphogenesis remains one of the most probable for numerous natural phenomena, including vertebrate limb pattern formation[15]; embryonic feather branching, for which experimental evidence identifies the molecules serving as activators and inhibitors[16]; skin colouration patterns[17]; the placement and number of teeth in mammals[17]; and limb development[17].

Taken independently to the rest of the model, the diffusion sector dictates that each morphogen moves from regions of high concentration to less concentrated regions at a rate proportional to its concentration, and to the diffusivity of its containing substance. In an unbounded system (infinitely large), the diffusivities would be inversely proportional to the square root of the molecular weights[18].

The rate at which the chemical reactions take place is assumed to obey the law of mass action, which states that this rate is proportional to the concentration of the reacting substances[19]. Note that this law only applies to elementary reactions, and not to composite reactions[5]. The former, in contrast to the latter, involves only one reaction step.

The system's state can be divided into a mechanical and a chemical part. The former concerns the stress, velocity, density and elasticity of the matter, while the latter involves the chemical composition at each point in the substance. It will be shown that the rich behaviour of the model in development is to be attributed to the coupling of the mechanical properties to the chemical data.

What is meant with the chemical composition at a point is the limiting value of the chemical composition of a small region of the substance as this region is taken to be infinitesimally small about some point. It is hereby possible to talk of morphogenetic fields—the continuous concentrations of shape forming chemicals[5]. We will work with the assumption that all of the fields are continuous.

In his 1952 paper where the term morphogenesis is introduced, Turing opted to ignore the interdependence of the chemical and mechanical parts, stating that this coupling adds enormously to the difficulty[5]. It is fascinating that he should consider the coupling of these parts important in the context of biology, given that the motor proteins dynein and kinesin were only discovered some decades later. The computational freedom granted by modern computers permits one to simulate a system where the mechanical and chemical parts do influence each other. This thesis will investigate the resulting phenomena, starting with a reaction-diffusion model on a static substrate, as was the case in Turing's paper[5], then considering the influence of the chemical concentration on a dynamic substrate, and vice versa once the chemicals are made to advect with the resulting flow. Next, the chemicals will be confined to a thin droplet having surface tension, and finally, the effects of viscoplastic rheology will be analysed.

Any model has simplifying assumptions that distance its relation to the real world, and this one is no exception. At first one might be opposed to ignoring the internal structure of the cells, but this proves to be of no concern. The reaction-diffusion model has been shown to apply universally to a great many organisms, and the predictions of this model relate to emergent observables in real life[13]. That is to say, the behaviour concerned here is universal among biological organisms and independent of the detailed structure of the system's constituents.

1.2 Reaction-Diffusion Systems

The evolution of the morphogenetic fields is governed by reaction-diffusion equations. For chemical reactions, the reaction equations are derived using the law of mass action, and it is further assumed that each chemical diffuses through the medium it resides in. But all other effects, such as advection, are considered irrelevant at this stage. Advection effects will be introduced later so as to bridge the mechanical and chemical sectors of this system.

The law of mass action regards the chemical reaction network[19]

$$\sum_{n=1}^{N} g(n,r)C_m \xrightarrow{k(r)} \sum_{n=1}^{N} h(m,r)C_n, \quad (r = 1,2,\ldots,R), \tag{1.1}$$

where $g(n,r)$ is the stoichiometric coefficient of the chemical C_n on the left hand side of the rth reaction, $h(n,r)$ is the coefficient on the right hand side, and $k(r)$ is the rate at which the rth reaction occurs. The mass action law then states that this reaction network is modeled by the N autonomous polynomial differential equations[19]

$$f_n \equiv \frac{\mathrm{d}C_n}{\mathrm{d}t} = \sum_{r=1}^{R} \left[h(n,r) - g(n,r)\right] k(r) \prod_{n=1}^{N} C_n^{g(n,r)}, \quad (n = 1,2,\ldots,N), \tag{1.2}$$

Note that the concentration of the chemical C_n has been given the same symbol as the representation for the chemical itself. It is granted that context will be sufficient to differentiate the two.

The equation of motion for the chemicals is given by the sum of the diffusive and mutual reaction components

$$\frac{\partial C_n}{\partial t} = D_n \nabla^2 C_n + f_n(C_1, \ldots, C_N), \tag{1.3}$$

where we will consider in this chapter a stationary, two-dimensional, two-way periodic domain $\mathscr{D} = \mathbb{T}^2$. Using Turing's terminology, $C_1, \ldots C_N$ are the morphogenetic fields (chemicals), $D_1, \ldots, D_N$ are diffusion constants, $\nabla^2 = \partial_x^2 + \partial_y^2$ is the Laplace operator, and $f_1, \ldots, f_N$ are non-linear local sources that describe the chemical reactions. Unless the chemical mixture is very simple, one cannot easily make predictions about the shape of f_n, since the reaction rates $k(r)$ are, in general, non trivial functions of the concentrations C_n[13,19].

Lastly, we will not consider explicit cross diffusion by means of a non-diagonal diffusion matrix (e.g. the coefficient of the Laplace operator is taken to be D_n and not an $N \times N$ matrix). Cross diffusion relaxes the conditions for pattern formation, and is the norm in living systems[20]. But, later on, when the chemicals are allowed to be advected by the medium they reside in and can accelerate its flow, this advection and acceleration will serve a similar role to cross diffusion.

At the early stages of development, when the biological tissue consists of tens to hundreds of cells, the morphogenetic fields are taken to be homogeneous. This is reflected in the model by the enforcement of the existence of a spatially homogeneous and stationary solution to the system of equations, also called a thermodynamic branch. To guarantee the existence of a thermodynamic branch, a bounded system must have the flux of the morphogenetic fields vanish at the boundaries, be fixed in value at the boundaries, or have periodic boundaries[13].

When there is only one morphogenetic field ($N = 1$), spatial homogeneity is never broken by an instability, as shown in appendix A[13]. Furthermore, even if a system was started in a non-homogeneous state, it will certainly decay to one eventually since inhomogeneous stable states cannot exist given the stated boundary conditions, regardless of the form of f_1[13]. This can be shown by considering the stability of the Fourier transformed linearised system, an analysis which shows that the first spatial mode to grow exponentially is the homogeneous zero-frequency mode. Linear stability analysis will be handled in the following section. We will therefore consider the most simple model, consisting of two chemicals, that can produce non-homogeneous steady-states.

1.2.1 Linear Stability Analysis

The precise way in which a homogeneous steady-state—that is, a spatially uniform and time-independent state—loses its stability to inhomogeneous modes is the subject matter of linear stability analysis. Its approach is to consider a small, inhomogeneous perturbation, and to study the evolution of this perturbation on the linearised system. If one finds that the perturbation grows exponentially, then one claims that the system is unstable with respect to that perturbation, and a spatial pattern is expected to

develop. Vice versa, if the perturbation decays exponentially, then the system is said to be stable with respect to the perturbation, and no pattern will develop. In this way, it is possible to map out the stability of perturbations across all spatial wavelengths, and make statements about the initial pattern development.

Consider a general second order PDE in f of the form

$$a_{11}\frac{\partial^2 f}{\partial \xi^2} + 2a_{12}\frac{\partial}{\partial \xi}\frac{\partial f}{\partial \eta} + a_1\frac{\partial f}{\partial \xi} + a_2\frac{\partial f}{\partial \eta} + a_0 f = 0 \tag{1.4}$$

where a_i are coefficients. One can classify this PDE into three distinct classes: elliptic, parabolic, and hyperbolic, as follows[21].

Elliptic If $a_{12}^2 < a_{11}a_{22}$. Then, the PDE reduces to $\partial_\xi^2 f + \partial_\eta^2 f + \ldots = 0$. Here, $(\ldots)$ denotes terms of order 1 or 0. Examples are Laplace's equation and Poisson's equation. One key feature of linear elliptic PDEs is that their solutions are not smooth where and only where the coefficients a_i are not smooth. Different classes of PDEs tend to reduce to elliptic PDEs when solving for the steady-state.

Hyperbolic If $a_{12}^2 > a_{11}a_{22}$. The PDE reduces to $\partial_\xi^2 f - \partial_\eta^2 f + \ldots = 0$. The solutions to hyperbolic PDEs are wave-like; one can speak of a speed at which information propagates. This is in stark contrast to elliptic and parabolic PDEs, for which the solution instantly and globally responds to disturbances in the initial value or the boundary conditions. Such hyperbolic PDEs are associated with conservation laws.

Parabolic If $a_{12}^2 = a_{11}a_{22}$. Then, unless $a_{11} = a_{12} = a_{22} = 0$, the PDE reduces to $\partial_\xi^2 f + \ldots = 0$. An example is the one-dimensional heat equation. Linear parabolic PDEs have the property that an initial-value or a boundary-value problem has a solution for all time.

The steady state of equation (1.3) is found by solving the elliptic equation

$$D_n \nabla^2 C_n + f_n(C_1, \ldots, C_N) = 0, \tag{1.5}$$

however, we might assume that an analytical solution to the above equation is not obtainable because of the non-linearities of f_n. If a homogeneous steady state is known, linearising equation (1.3) allows for testing the stability of this state with respect to small perturbations. If the system is unstable to a plane wave perturbation of non zero spatial frequency, then there is the possibility for pattern formation.

We will focus on the case of two fields. To analyze the stability of equation (1.3) with regards to a small deviation from a homogeneous, stationary state $(\overline{C}_1, \overline{C}_2)$, we will linearise it with regards to that state by defining $\delta C_1 \coloneqq C_1(\boldsymbol{r}, t) - \overline{C}_1$, $\delta C_2 \coloneqq C_2(\boldsymbol{r}, t) - \overline{C}_2$, which can be cast as

$$\frac{\partial \boldsymbol{\Phi}}{\partial t} = \mathsf{A}\boldsymbol{\Phi}, \tag{1.6}$$

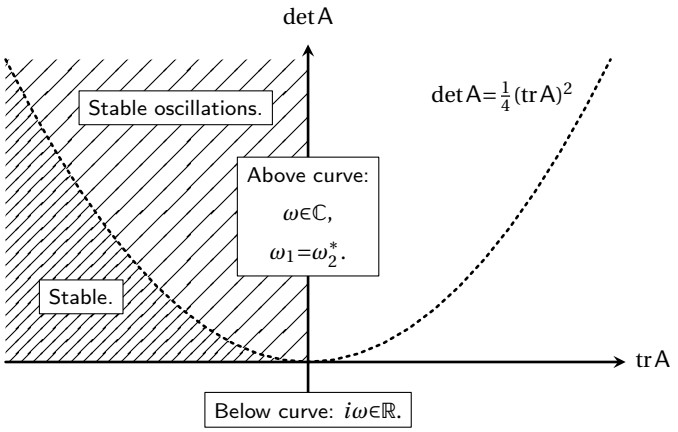

Figure 1.1: The stability of a linearised reaction-diffusion system with linear operator A for different values of det A and tr A. The system is stable with regards to a wave perturbation of temporal frequency ω in the fourth quadrant. Adapted from Cross[22].

with $\mathbf{\Phi} \coloneqq (\delta C_1, \delta C_2)^T$ and

$$\mathsf{A} = f_{ij} + D_{ij}\nabla^2 = \begin{pmatrix} f_{11} + D_1\nabla^2 & f_{12} \\ f_{21} & f_{22} + D_2\nabla^2 \end{pmatrix}. \tag{1.7}$$

Here, D_{ij} are the diffusion coefficients, and the matrix formed by f_{ij} is the Jacobian of the reaction terms f_n. We assume translational symmetry, and so the solution to this equation can be given as a superposition of harmonic modes of temporal and spatial frequency ω_l and $\boldsymbol{k}_l$, respectively, where l is the mode number[2]. The dispersion law is found upon substituting this solution in equation (1.6) and solving for ω_l as a function of $\boldsymbol{k}_l$, and it is given by

$$\omega(k^2) = \frac{i}{2}\left(\operatorname{tr}\mathsf{A} \pm \sqrt{\Delta}\right), \quad \Delta = (\operatorname{tr}\mathsf{A})^2 - 4\det\mathsf{A}. \tag{1.8}$$

Whether $i\omega$ is real or complex valued is decided by the sign of Δ:

$$-i\omega = \frac{1}{2}\begin{cases} \operatorname{tr}\mathsf{A} \pm \sqrt{|\Delta|} \in \mathbb{R} & \text{if } \Delta > 0, \\ \operatorname{tr}\mathsf{A} \in \mathbb{R} & \text{if } \Delta = 0, \\ \operatorname{tr}\mathsf{A} \pm i\sqrt{|\Delta|} \in \mathbb{C} & \text{if } \Delta < 0. \end{cases} \tag{1.9}$$

The homogeneous stationary-state is stable if $\operatorname{Re}\{-i\omega\} < 0$ holds for both eigenvalues for all harmonic modes l. For this to be the case, the trace of A must be negative and its determinant must be positive.

Given a bifurcation parameter χ which changes sign as the system first becomes unstable with respect to small inhomogeneous perturbations, one can classify the system into one of three stability classes[22]:

Type-I The system first becomes unstable at a non-zero wavenumber $k_c > 0$; patterns develop at a characteristic scale of $2\pi/k_c$. When the bifurcation parameter is further increased, a band of wave numbers become linearly unstable and contribute to pattern development in a non-linear fashion.

Type-II The growth rate of the zero frequency spatially homogeneous mode is always zero, hence the system tends to develop patterns of long wavelengths as the bifurcation parameter tends to zero.

Type-III The growth rate is maximal at zero wavenumber for all non-zero bifurcation parameters χ. If the dispersion relation is a decreasing function of the bifurcation parameter, this implies that for any non-zero χ, a finite band of wavenumbers will contribute non-linearly to the pattern development.

For small values of the bifurcation parameter, the pattern formation classified by these stability classes displays universal behaviour independent of the particular model describing the system. Features of the patterns that initially develop according to this theory tend to persist through to the later stages of the system's evolution. That is the strength of this classification scheme.

Each of these stability classes is further divided into two more: a stationary subclass, denoted by a suffix *s* and an oscillatory one, denoted by a suffix *o*. For instance, the stationary instability of the first type is denoted type-I-s. When the system parameters change, and the system drifts from the fourth to the third quadrant, we speak of a stationary instability; when the system transitions from the fourth quadrant to the first, we speak of an oscillatory instability (see figure 1.1).

The Turing instability. The reaction-diffusion systems we will consider are those that are stable in the absence of diffusion ($D_i = 0$). Turing predicted that diffusion can destabilize such a system when it is in its homogeneous steady-state, giving rise to spatial patterns of definite wavelength that grow exponentially, until non-linearities inhibit any further growth[5]. That spatial wavelength is given by

$$\lambda_c = 2\pi\sqrt{\frac{2D_1D_2}{D_1f_{22} + D_2f_{11}}}. \tag{1.10}$$

If the system is stable in the absence of diffusion, then the following are necessary and sufficient conditions for the diffusive instability of a homogeneous steady state (see appendix A):[22]

$$\begin{aligned} \operatorname{sign} f_{11} \operatorname{sign} f_{22} &= -1, & f_{11} + f_{22} &< 0, \\ \operatorname{sign} f_{21} \operatorname{sign} f_{12} &= -1, & f_{11}f_{22} - f_{12}f_{21} &> 0, \end{aligned} \tag{1.11}$$

and

$$D_1f_{22} + D_2f_{11} > 2\sqrt{D_1D_2(f_{11}f_{22} - f_{12}f_{21})}. \tag{1.12}$$

Observe that if one diffusion coefficient is a multiple of the other, then this condition becomes true at the trivial critical diffusion coefficient $D_1^{\text{crit}} = 0$ (if the Jacobian of the reaction terms is taken to be fixed). In that case, any strictly positive diffusion coefficient will allow for the Turing instability to occur.

Defining the two lengths $l_1 = \sqrt{D_1/|f_{11}|}$ and $l_2 = \sqrt{D_2/|f_{22}|}$, this condition can be written as

$$\frac{1}{2}\left(\pm\frac{1}{l_1^2} \mp \frac{1}{l_2^2}\right) > \sqrt{\frac{f_{11}f_{22} - f_{12}f_{21}}{D_1 D_2}}, \tag{1.13}$$

from which it is evident that one length must be sufficiently larger than the other, so as to satisfy the above condition. This condition is considered restrictive, but is relaxed when considering a non-stationary domain, which is in fact more representative for a biological system[23]. This will be the case once the dynamics are confined to a deformable droplet.

Since these lengths involve the diagonal elements of the reaction matrix, and the two rates have opposite signs, one is given the name *inhibitor* and the other *activator*. The rate of the inhibitor is negative and so it inhibits its own growth, while the rate of the activator is positive and so it amplifies its growth. When $\operatorname{sign} f_{11} = \operatorname{sign} f_{21}$, the activator amplifies the production of both chemicals, and the inhibitor, likewise, affects both.

1.2.2 The Brusselator System

In a paper published in 1967, Prigogine and Lefever introduce a simple scheme of reactions that results in spontaneous spatial pattern formation in the chemical concentrations[24,25]. It has since been given the name "the Brusselator", as reference to its origin in Brussels. The Brusselator system is derived from the reactions

$$\text{I.} \quad A \xrightarrow{k_1} C_1, \tag{1.14}$$

$$\text{II.} \quad B + C_1 \xrightarrow{k_2} C_2 + D, \tag{1.15}$$

$$\text{III.} \quad 2C_1 + C_2 \xrightarrow{k_3} 3C_1, \tag{1.16}$$

$$\text{IV.} \quad C_1 \xrightarrow{k_4} E. \tag{1.17}$$

The total reaction is simply $A + B \rightarrow E + D$. Here, A and B are species that are taken to be abundant and equally distributed everywhere in space, and D and E are waste products that are assumed to be efficiently and quickly removed. One can draw an analogy to living systems, which continuously convert reactants high in free-energy to low-free-energy waste products, using the difference to perform work[26]. This scheme serves as a minimal model for pattern forming reaction-diffusion systems. *

The dynamic equations are derived from equation (1.14) using the law of mass action detailed in section 1.2[24]. Defining a reference length scale L—the length of the periodic domain, and a reference chemical concentration $C_0 := Ak_1/k_4$—derived from the steady-state, such that $C_1 := C_0\overline{C}_1$ (and similarly for C_2), the dynamic equations take the dimensionless form

* For similar schemes, refer to Prigogine and Lefever (1967).

$$\begin{aligned}\frac{\partial C_1}{\partial t} &= \nabla^2 C_1 + \mathrm{Da}_1 - (\mathrm{Da}_2 + \mathrm{Da}_4) C_1 + \mathrm{Da}_3 C_1^2 C_2, \\ \frac{\partial C_2}{\partial t} &= D\nabla^2 C_2 + \mathrm{Da}_2 C_1 - \mathrm{Da}_3 C_1^2 C_2.\end{aligned} \tag{1.18}$$

We have dropped the notation $\overline{x}$ for clarity. Here, $D \coloneqq D_2/D_1$ is the ratio of the diffusion coefficients, and the chemical rates take the form of the dimensionless Damköhler numbers

$$\mathrm{Da}_1 \coloneqq \frac{k_1 L^2 A}{D_1 C_0}, \quad \mathrm{Da}_2 \coloneqq \frac{k_2 L^2 B}{D_1}, \quad \mathrm{Da}_3 \coloneqq \frac{k_3 L^2 C_0^2}{D_1}, \quad \mathrm{Da}_4 \coloneqq \frac{k_4 L^2}{D_1}, \tag{1.19}$$

which for notational convenience will be momentarily called a, b, c and d respectively. These numbers are the ratios of the chemical reaction timescales to the diffusive transport timescales.

We will henceforth refer to this system of equations as the classical Brusselator system of equations, when distinction is necessary against modifications that we will present in the following sections.

Only some choices for the value of these dimensionless groups will result in spontaneous pattern formation. We will take b as the control parameter, defining b_c as the critical value at which pattern formation occurs for the first time as it is increased. The dimensionless bifurcation parameter this gives rise to—χ—is constructed so that it changes sign at criticality:

$$\chi \coloneqq \frac{b - b_c}{b_c}. \tag{1.20}$$

Let us investigate the dispersion relation regarding this bifurcation parameter. We assume that the linearised system A is at equilibrium, so that we may obtain the dispersion relation by solving $\det(\mathsf{A}) = 0$. We substitute χ for b in A and plot the dispersion curve (see figure 1.2)

$$\chi(k^2) = \frac{k^2}{b_c} + \frac{a^2 c}{D d b_c}\left(\frac{1}{k^2} + \frac{1}{d}\right) + \frac{d}{b_c} - 1. \tag{1.21}$$

We see that as the bifurcation parameter passes zero, a single non-zero wavenumber becomes linearly unstable. As it is increased further, a finite and increasingly broad band of wavenumbers become unstable. But the real part of the perturbation frequency ω is zero. Evidently, this system's stability class is Type-I-s.

As for the unstable band of wavenumbers: in the limit $k^2 \gg 1$, we may approximate $\chi \approx k^2/b_c$, and we may therefore say that the modes that grow and persist to become spatial patterns lie approximately in the range $k^2 \in (0, \chi b_c]$.

The dispersion curve has a single minimum at a critical wavenumber k_c. It is at this minimum that the trivial solution first becomes unstable as the system is linearly perturbed[2]. Since this minimum occurs at non-zero wavenumber, the system will develop a spatial pattern of wavelength $\lambda_c = 2\pi/k_c$. This wavelength is termed the chemical wavelength.

We conclude that for an appropriate choice of a, c, d, and D, the eigenfunctions of A have a nontrivial spatial dependence, and grow exponentially in amplitude[2]. By plugging in the values of the elements of A in equation (1.10) we see that when the reaction parameters are fixed, the feature size of the patterns depends on the diffusion coefficients as (see figure 1.2)

$$\lambda_c \propto \sqrt{D}. \tag{1.22}$$

The Brusselator system is known to develop certain spatial patterns for different values of χ, of which hexagons, inverted hexagons, and stripes (figure 1.2)[14]. Not all values for the parameters of the Brusselator allow for these patterns to be stable. Peña *et al.* have mapped out the stability thresholds in the parameter space $(a/\sqrt{D}, \chi)$ for the same parameters taken here[14]. For the value of $a/\sqrt{D}$ that we take, the authors found that an inverted hexagon pattern is stable for $0 < \chi \lesssim 0.1$, a stripe pattern is stable for $0.05 \lesssim \chi \lesssim 1.3$, and that a hexagon pattern is stable for $1.3 \lesssim \chi \lesssim 0.6$. Note that these stability bands overlap. We will set $\chi = 0.1$ henceforth unless otherwise stated. For this value, the system develops a striped pattern.

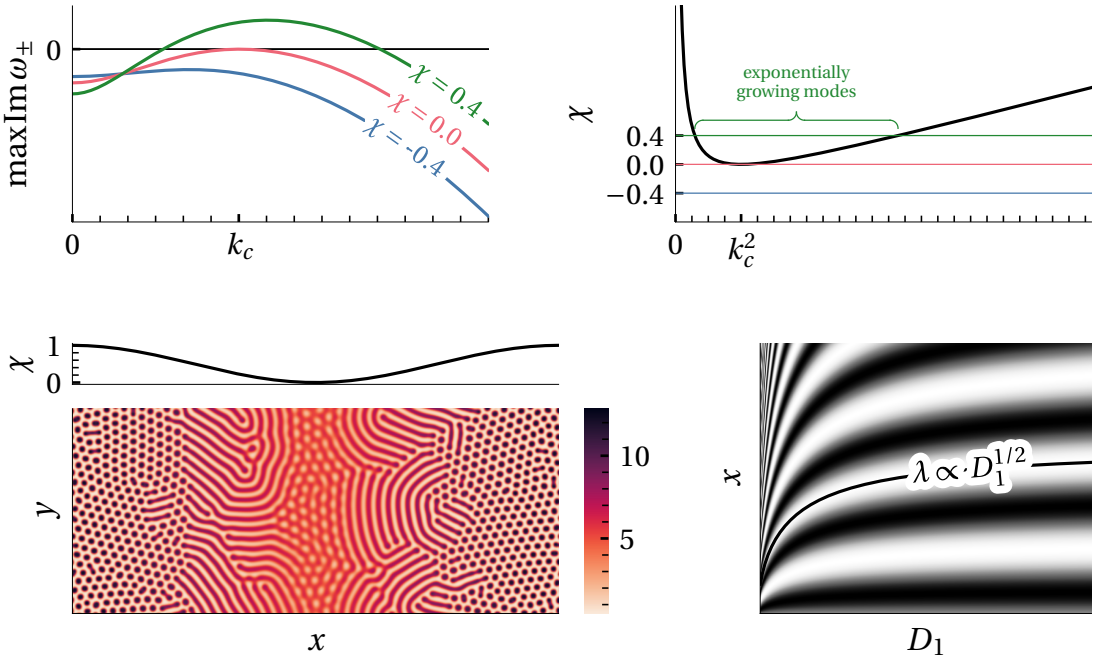

Figure 1.2: (top left) The maximum imaginary part of ω for various values of χ. The real part is not depicted as it is zero everywhere for all three bifurcation parameters. At instability, $\chi = 0$ and there is precisely one wavenumber for which the imaginary part of ω is zero. An infinitesimal increase in χ will mean that a spatial pattern of that wavenumber can develop. This mode will grow exponentially until the nonlinear part of the system comes to dominate the behaviour. Any plane wave for which the real part of ω is greater than zero is likewise unstable. The curve $\chi = 0.4$ has a range of such wavenumbers, enclosed between the two intersections with the zero line. (top right) The dispersion curve (equation (1.21)) for the values $a = 4.5, c = d = 1, D = 8$. The curve has a minimum at a non-zero wavenumber $k^2 = (b_c - d)/2 - ca^2/2d^2D$, hence the system will develop a spatial pattern. (bottom left) The Brusselator reaction-diffusion system is solved for sinusoidally varying χ along x. Different patterns emerge in the concentration of the chemicals for different values of χ; only the first chemical is shown. The Brusselator parameters are $a = 4.5$, $c = d = 1$, and $D_1 = 8D_2$ (recall that b is a function of χ). (bottom right) The chemical wavelength of the Brusselator increases as the square root of the dimensionless diffusion coefficient. Plotted along each slice of D is the critical plane wave $\sin(k_c x)$.

Chapter 2

Continuum Mechanics of Active Systems

Mechanicals stresses are known to have an effect on the chemical patterns resulting from the Turing instability; so much was predicted when the instability was discovered[5]. Since then, at least one mechanism was discovered by which similar pattern formation can occur via mechanical means: active stress produces a flow, which itself acts as both the local activator and lateral inhibitor, forming stable spatial patterns in the absence of chemical reactions[27]. Another study unveils pulsatory patterns in an active-stress reaction-diffusion-advection system, patterns which are not possible with a reaction-diffusion system on a static substrate[28].

A dynamic substrate, one that flows, demonstrably alters the patterns that would form on a static substrate. And in a biological context, it is the norm rather than the exception that the substrate is dynamic. Consider for example protein motors such as myosin, which give rise to gradients of activity in the cell cortex, and thus cause the substrate in which they are embedded to flow[29]. This section will be spent coupling of the reaction-diffusion equations to a dynamic substrate: a fluid.

Fluid flow is a subject with a long and rich history[30]. The case of conservative and incompressible fluids was formalised by Leonhard Euler in 1757[31]. In 1821, Claude-Louis Navier incorporated dissipation into the model by introducing viscosity, the internal friction of the fluid[30]. The mathematical description of viscosity was already worked out by Sir Isaac Newton in his famous book Philosophiæ Naturalis Principia Mathematica. This is an essential addition, as most phenomena observed in real fluids occur due to viscous effects[32]. Such phenomena include the creation of circulation, or of vortices, or the experimental fact that the flow speed tends to zero near walls[32]. Throughout the middle of the 19th century, these equations have been refined and improved upon by Sir George Gabriel Stokes[30].

Hence, we have the well known Navier-Stokes equations, which apply to incompressible Newtonian fluids, and which read

$$\overbrace{\underbrace{\frac{\partial \boldsymbol{u}}{\partial t} + \boldsymbol{u}\cdot\boldsymbol{\nabla}\boldsymbol{u} = -\frac{1}{\rho}\boldsymbol{\nabla}p + \frac{\mu}{\rho}\nabla^2\boldsymbol{u}}_{\text{Navier-Stokes}},}^{\text{Euler}} \tag{2.1}$$

where $\boldsymbol{u} = (u_x, u_y, u_z)$ is the fluid velocity vector, p is the fluid pressure (which is distinct from the thermodynamic pressure[33]), ρ is the fluid density, and μ is the kinematic viscosity. Here we will take the two-dimensional variant of the Navier-Stokes equations.

These equations can be derived from a more general principle of momentum transport through a continuum, starting from the Cauchy momentum equations. It is of interest to show the broad lines of a derivation of the Cauchy momentum equations in order to motivate and understand the stress tensor, as it will play a key part in subsequent analysis. The derivation that will result in a system of equations for the flow of the fluid rests on two basic principles: conservation of mass, and Newton's second law. This suffices, because we will only consider incompressible flows. *

2.1 Transport Laws of Passive Fluids

The principle of conservation of mass states that the rate of increase of mass in a region $\mathscr{D}$ is balanced by the rate at which mass crosses the boundary $\partial\mathscr{D}$ in the inward direction

$$\frac{\mathrm{d}}{\mathrm{d}t}\int_{\mathscr{D}} \rho \,\mathrm{d}V = -\int_{\partial\mathscr{D}} \rho\boldsymbol{u}\cdot\boldsymbol{n}\,\mathrm{d}A. \tag{2.2}$$

Using the divergence theorem, and that the region $\mathscr{D}$ is arbitrary, we can write the continuity equation

$$\frac{\partial\rho}{\partial t} + \boldsymbol{\nabla}\cdot\left(\rho\boldsymbol{u}\right) = 0, \tag{2.3}$$

or

$$\frac{\mathrm{D}\rho}{\mathrm{D}t} + \rho\boldsymbol{\nabla}\cdot\boldsymbol{u} = 0. \tag{2.4}$$

Newton's second law $m\boldsymbol{a} = \boldsymbol{F}$ resolves to

$$\frac{\mathrm{d}}{\mathrm{d}t}\int_{\mathscr{D}_t} \rho\boldsymbol{u}\,\mathrm{d}V = -\int_{\partial\mathscr{D}_t} (p\boldsymbol{n} - \boldsymbol{\tau}\cdot\boldsymbol{n})\,\mathrm{d}A, \tag{2.5}$$

where $\mathscr{D}_t$ is the volume $\mathscr{D}$ moving with the fluid, p is the static fluid pressure, and $\boldsymbol{\tau}$ is the deviatoric stress tensor, which will henceforth be called the stress tensor. Here

* For a more complete derivation, refer to Chorin (2000).

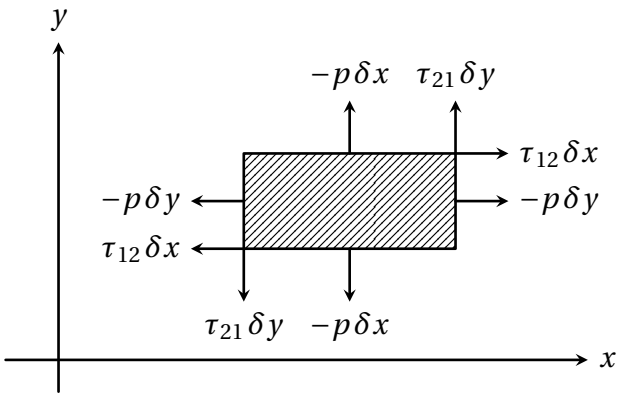

Figure 2.1: The forces acting on the surfaces of a rectangular fluid element of width δx and height δy. This representation is only an approximation as the rectangle is to be infinitesimally small. Adapted from Batchelor[34].

we decompose the force into an isotropic part (the pressure) and a part that depends on the force due to the relative motion of neighboring regions in the fluid (the stress tensor), see figure 2.1. The sign convention picked here is motivated by the tendency of fluids at rest to be at a state of compression[34].

The pressure and stress tensors represents molecular momentum diffusion: fast moving particles transfer their momentum to neighboring particles if their momentum is smaller or not aligned with the latter[33].

Consider now a fluid particle which traces a path $\boldsymbol{x}(t) = (x(t), y(t))$, and a general function of position and time $f(\boldsymbol{x}(t), t)$. By the chain rule, we obtain an expression for the material derivative $\mathrm{D}/\mathrm{D}t$

$$\frac{\mathrm{d}f}{\mathrm{d}t} = \frac{\partial f}{\partial t} + \boldsymbol{u}\cdot\boldsymbol{\nabla} f = \frac{\mathrm{D}f}{\mathrm{D}t}. \tag{2.6}$$

The material derivative can be thought of as a regular derivative from the point of view of a reference frame that moves with the fluid.

The Transport Theorem states that for any function $f(\boldsymbol{x}, t)$, we have[33]

$$\frac{\mathrm{d}}{\mathrm{d}t}\int_{\mathscr{D}_t} \rho f \,\mathrm{d}V = \int_{\mathscr{D}_t} \rho \frac{\mathrm{D}f}{\mathrm{D}t}\,\mathrm{d}V. \tag{2.7}$$

Using the Transport Theorem, Newton's second law can be re-written

$$\int_{\mathscr{D}_t} \rho \frac{\mathrm{D}\boldsymbol{u}}{\mathrm{D}t}\,\mathrm{d}V = -\int_{\partial\mathscr{D}_t} (p\boldsymbol{n} - \boldsymbol{\tau}\cdot\boldsymbol{n})\,\mathrm{d}A, \tag{2.8}$$

and using the divergence theorem, we can write the differential form of Newton's second law

$$\rho\frac{\mathrm{D}\boldsymbol{u}}{\mathrm{D}t} = -\boldsymbol{\nabla} p + \boldsymbol{\nabla}\cdot\boldsymbol{\tau}. \tag{2.9}$$

For Newtonian fluids, the stress tensor depends linearly on the velocity gradient $\nabla \boldsymbol{u}$; Further making the assumption that $\boldsymbol{\tau}$ is invariant under SO(n) (that is, rigid body rotations, which ought to have no effect on diffusion of momentum), and that $\boldsymbol{\tau}$ is symmetric (as a consequence of balance of momentum), leads to $\boldsymbol{\tau}$ depending only on the symmetric part of $\nabla \boldsymbol{u}$, which is defined as the deformation tensor $\dot{\boldsymbol{\gamma}} = \left[\nabla \boldsymbol{u} + (\nabla \boldsymbol{u})^T\right]/2$[33].

Hence we can deduce that

$$\boldsymbol{\tau} = \lambda(\nabla \cdot \boldsymbol{u})\mathrm{I} + 2\mu\dot{\boldsymbol{\gamma}}, \tag{2.10}$$

where I is the identity. This defines the constants λ and μ. Rewriting so to have one traceless term, we get

$$\boldsymbol{\tau} = 2\mu\left[\dot{\boldsymbol{\gamma}} - \frac{1}{2}(\nabla \cdot \boldsymbol{u})\mathrm{I}\right] + \zeta(\nabla \cdot \boldsymbol{u})\mathrm{I}, \tag{2.11}$$

where μ and $\zeta = \lambda + \mu$ are, respectively, the first and second coefficients of viscosity, or the shear and bulk viscous coefficients. We identify the shear viscous coefficient with the kinematic viscosity coefficient from before.

We will only consider incompressible fluids, such that $\nabla \cdot \boldsymbol{u} = 0$ everywhere. With this constraint, we can compile and simplify the above equations (namely equation (2.4) and equation (2.9)) to recover equation (2.1):

$$\boxed{\begin{aligned} \rho\frac{\mathrm{D}\boldsymbol{u}}{\mathrm{D}t} &= -\nabla p + \nabla \cdot \boldsymbol{\tau}, \\ \frac{\mathrm{D}\rho}{\mathrm{D}t} &= 0, \\ \nabla \cdot \boldsymbol{u} &= 0, \end{aligned}} \tag{2.12}$$

with the boundary condition $\boldsymbol{u} = 0$ everywhere on the interface containing the fluid where that interface is not moving. This is commonly called the no-slip condition; it is experimentally motivated by observations of dye-tainted water coming to a stop as it approaches a wall, and it serves to close the system of equations[33]. The density ρ will be taken to be constant henceforth, and as such the second member of equation (2.12) will be omitted. However, the last member will be kept, as it is a less obvious constraint in comparison.

Other terms can be added to equation (2.12) as necessary to model the problem at hand. For example, one may want to consider gravity, in which case a term $\boldsymbol{f}_g$ needs to be added to the right hand side of the first member of equation (2.12). Such a term is called a body force, as it acts on the bulk of the fluid. Likewise we will later consider surface tension and acceleration due to chemical gradients to act on the fluid as body forces by supplementing equation (2.12) with similar terms.

Note that for incompressible Newtonian fluids, like water, taking the divergence of equation (2.11) results in

$$\boldsymbol{\nabla} \cdot \boldsymbol{\tau} = \mu \nabla^2 \boldsymbol{u}, \quad \text{(incompressible, Newtonian)}. \tag{2.13}$$

The behaviour of more complex fluids such as mud, snow during an avalanche, blood, and oil, to name a few examples, is contained in the stress tensor. These complications will be detailed as they are introduced.

2.2 Active Stresses

An active system is one whose constituents receive energy from their surroundings—that which is not considered part of the system. In other words, active systems receive a continuous influx of energy from their surroundings. Passive systems do not; those can only dissipate energy, and will therefore eventually cease to exhibit any dynamics and reach a stationary state. One example of a passive system is a recently stirred cup of tea, which will eventually dissipate all kinetic energy in the tea by molecular friction and stop whirling. An active system might consist of living elements, consuming food to propel themselves, thereby injecting chemical energy in the food into the system in the form of kinetic energy.

On a more general setting, the stress on an active system can respond to the composition of the fluid itself, both in the hydrostatic or deviatoric parts of the stress tensor. In this work we focus on the assumption that such an active stress is encoded on the hydrostatic term. Furthermore, the stress tensor can be decomposed into a passive part, which is the only part considered so far, and an active part

$$\boldsymbol{\tau} = \boldsymbol{\tau}_p + \boldsymbol{\tau}_a. \tag{2.14}$$

The passive part of the stress tensor $\boldsymbol{\tau}_p$ can be derived from a Ginzburg-Landau free-energy functional of some order parameter ϕ[35,36]

$$F[\phi] = \int \frac{1}{2}(\boldsymbol{\nabla}\phi)^2 + V(\phi)\,\mathrm{d}\boldsymbol{x}, \tag{2.15}$$

where $V(\phi)$ is a double-well potential function with degenerate minima at $\phi = \pm 1$. It is called passive since it does not inject energy into the system; at most, it can dissipate energy. This is the basis for the so-called Model A, which models the evolution of the order parameter in a system without conservation laws, and Model B, which models systems where the order parameter is conserved[37].

Models like those assume the existence of a free-energy functional. But if it exists, then the system will evolve to minimize it, and once the system reaches a minimum, it will cease to evolve. While this formulation does result in a stress tensor that depends on a chemical potential, we are not interested in such a system. On the contrary, our interest lies in systems that are constantly driven out of equilibrium, and therefore systems that cannot be represented by a free-energy functional[37].

Hence we are interested in the active part $\boldsymbol{\tau}_a$, which represents the system constituents which get their energy from their surroundings in order to do work[37]. This continuous injection of energy from the external environment into the system keeps it from reaching equilibrium, allowing for the formation of spatio-temporal patterns[37].

In general, the specific form of the stress tensor is obtained by coarse graining a microscopic description of the system[38]. However, the approach taken here is a phenomenological one. The form of the active stress tensor was decided by the consideration that its divergence, representing a force, would be proportional to the gradient of one or more of the chemicals.

We expand the force due to the active stress in the gradients of the chemical concentrations, successively considering terms of higher order and halting once the first term is reached that is expected to yield interesting behaviour. Disregarding homogeneous terms, a term of the form $\boldsymbol{\nabla} C_1$ would be the simplest term in the gradient expansion of a general function of the chemical concentrations. However, an acceleration term of the form $\boldsymbol{\nabla} C_1$ would amount to a correction to the pressure, as it can be grouped in with the non-deviatoric part of the stress tensor. Since we assume incompressible fluids, such a pressure term does not result in interesting dynamics.

The next simplest term would be $C_1 \boldsymbol{\nabla} C_1$, but, this term can be written $\boldsymbol{\nabla} C_1^2/2$, and will therefore also be a correction to the pressure. The first term in the gradient expansion for which this does not hold, is $C_1 \boldsymbol{\nabla} C_2$. So in the spirit of choosing the simplest model that displays novel behaviour, this term is chosen as a basis for the active stress, so that it takes the form

$$\boldsymbol{\nabla} \cdot \boldsymbol{\tau}_a = \boldsymbol{f}_\alpha = \alpha C_1 \boldsymbol{\nabla} C_2, \tag{2.16}$$

where α is the activity coefficient.

Another way to circumvent this limitation is to consider boundary conditions that explicitly involve the stresses, thus fixing the gauge. However interesting in potential future considerations such an approach may be, it lies outside the scope of the present model.

2.3 Beyond Newtonian Fluids

The eukaryotic cell contains a nucleus floating in a complex fluid called the cytoplasm, consisting of smaller units (organelles) suspended in a substance consisting mostly of water. However, the organelles and other smaller floating bits or network structures interact in complicated ways that change the properties of the cytoplasm, so that it can no longer be said to be simply Newtonian. The cytoplasm has in fact been argued to be an active viscoplastic body, as opposed to a passive viscoelastic material as previously thought[39]. For the minimal model constructed in this work, this complication has the potential to produce dynamics that are otherwise inaccessible with Newtonian rheology. Hence, this section will be spent incorporating viscoplastic rheology into the model.

While every bit of a typical fluid flows to fill its container, a viscoplastic fluid can contain rigid regions that resist deformation. They behave as a solid body and so are only able to translate and rotate as a whole. Arrested regions will behave like a liquid again once the stress that is enacted upon them exceeds a critical threshold, named the yield-stress. Likewise, liquid regions solidify under low stress. This phenomenon is therefore not a phase transition, but rather mechanical in nature, and not a rare one at that[40].

Besides the hypothesis that the cell may exhibit this viscoplastic behaviour, many active systems in nature are known to exhibit this trait. One such biological system is mucus, which is likely key for both adhesion and locomotion for slugs and snails[41]. The underside of these creatures is host to displacement waves that propagate forward, causing the organism to move[41]. Force is exerted on the surface by means of adhesion through the mucus yield stress[41].

Marine organisms such as limpets must be able to resist ambient water flows, which they do by anchoring themselves to solid objects; but they must also be capable of releasing themselves at will in order to move[41]. They achieve this through mucus, much like slugs and snails. Evidence suggests that limpets manipulate mucus properties through chemical secretions, thereby actuating yield stress to control adhesion[41].

Viscoplastic rheology can evidently substantially alter the dynamics of active systems, which makes it an interesting complication to consider for the minimal model presently under construction. We will introduce viscoplastic effects by means of the Bingham model, which is a special case of the more general Herschel-Bulkley model. This model has a power-law dependence on shear rate in the yielded regions, allowing for both shear-thinning and shear-thickening behavior depending on model parameters[41]. We will implement the Herschel-Bulkley model in simulations since the added complexity is minimal, but we will always take the special case that reduces to the Bingham model.

The passive stress tensor in the Herschel-Bulkley model is given by

$$\begin{cases} \boldsymbol{\tau} = 2\mu_0 \left[k(\sqrt{2}\left|\mathrm{II}_{\dot{\gamma}}\right|^{1/2})^{n-1} + \dfrac{\tau_0}{\sqrt{2}\left|\mathrm{II}_{\dot{\gamma}}\right|^{1/2}\mu_0} \right] \dot{\boldsymbol{\gamma}} & \text{if } |\mathrm{II}_{\tau}|^{1/2} \geq \tau_0, \\ \dot{\boldsymbol{\gamma}} = 0 \quad \text{otherwise,} \end{cases} \tag{2.17}$$

where $\dot{\boldsymbol{\gamma}} = [\boldsymbol{\nabla u} + (\boldsymbol{\nabla u})^T]/2$ is the deformation tensor, $\boldsymbol{\tau}$ is the deviatoric part of the stress tensor, μ_0 is the coefficient of viscosity, τ_0 is the yield-stress, k is the consistency index, and $\mathrm{II}_A = \sum_i \sum_j A_{ij} A_{ji}$ is the second invariant of A[42]. The fluid is shear-thickening for $n > 1$ and shear-thinning for $n < 1$, but we will always take $k = 1$ and $n = 1$ so that we recover the Bingham model.

The location of solid-liquid interfaces is in general impossible to predict analytically, so numerical simulations are used instead[40,41]. But for viscoplastic fluids that exhibit complex flows or for complex geometries, typical computational methods for solving fluid flow problems fail[40]. It therefore becomes necessary to develop methods specific for viscoplastic fluids.

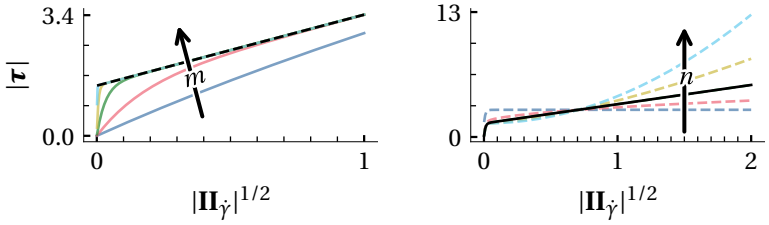

Figure 2.2: (left) The shear stress of a Bingham fluid is plotted against the rate of strain for varying values of the regularisation parameter m. A dashed line represents the un-regularised model. (right) A similar plot is repeated with dashed curves for varying values of the Herschel-Bulkley parameter n. A solid curve represents the value $n = 1$ which corresponds to the Bingham model.

One such method is the regularisation method, which will be used throughout this thesis. An alternative approach, the augmented Lagrangian method, rigorously enforces the yield-stress constraint, but is computationally expensive in comparison[40]. The regularisation method circumvents numerical singularities by modifying the constitutive equations so that they map onto standard Newtonian fluid dynamics formulations, allowing the reuse of existing, efficient solvers[40]. This involves introducing a regularisation parameter that smooths the discontinuous yield stress behavior; as the parameter approaches its theoretical limit, the ideal Bingham response is asymptotically recovered[40].

The regularised model remains well-defined even in unyielded regions (where the deformation tensor vanishes), rendering the fluid quasi-Newtonian[40]. This approximation eliminates rigid zones entirely, blurring the distinction between rigid and flowing regions. Consequently, simulations may predict unphysical phenomena, such as the inevitable onset of catastrophic flows in otherwise stable natural hazard scenarios[40]. As this limitation is of no great concern for this work, the regularisation method's computational efficiency and compatibility with existing solvers justify its adoption.

This regularised model is given by the continuous equation[43]

$$\boldsymbol{\tau} = 2\mu_0 \left[1 + \frac{\tau_0 (1 - e^{-m|\mathrm{II}_{\dot{\gamma}}|^{1/2}})}{\sqrt{2}|\mathrm{II}_{\dot{\gamma}}|^{1/2}} \right] \dot{\boldsymbol{\gamma}}, \quad \forall \dot{\boldsymbol{\gamma}}. \tag{2.18}$$

In choosing the regularisation parameter m, a few considerations must be made. First, a large enough value is needed to recover accurate dynamics, which is evident from the regularised stress tensor as in the limit $m \to \infty$, the un-regularised model is recovered. Note that this un-regularised model is singular when the deformation tensor vanishes. The limit $|\mathrm{II}_{\dot{\gamma}}| \to 0$ gives $\boldsymbol{\tau} = \mu_0 \left(2 + \sqrt{2} m \tau_0\right) \dot{\boldsymbol{\gamma}}$, showing that in order to recover solid body dynamics in this limit, m must be taken as large as possible, as it takes the form of a viscosity multiplier. Unfortunately, the computational complexity increases rapidly with increasing values of m[41]. It is therefore necessary to perform a convergence study so that one can choose the smallest value of m that yields an acceptable deviation from the expected results.

2.4 Mechano-Chemical Coupling

The active stress will cause the substrate to flow, sometimes sustaining an acceleration in one direction for long stretches of time, yielding unrealistically large velocities. One candidate mechanism to combat this behaviour is a simple friction term

$$\frac{1}{\lambda}\boldsymbol{f}_\lambda = -\frac{1}{\lambda}\boldsymbol{u}, \tag{2.19}$$

where λ is the damping time scale. This mechanism, known to be a consequence of the force-balance condition in thin-film-like active fluids, penalises large velocities more heavily than intermediate or weak velocities[27,28]. It represents drag due to motion relative to the substrate.

A fluid under the influence of the leading order terms of an active stress tensor, as argued above, gives the following deviatoric stress tensor:

$$\boldsymbol{\nabla}\cdot\boldsymbol{\tau} = \boldsymbol{\nabla}\cdot\boldsymbol{\tau}_p - \frac{1}{\lambda}\boldsymbol{u} + \alpha C_1 \boldsymbol{\nabla} C_2, \tag{2.20}$$

where for a Newtonian fluid we have $\boldsymbol{\nabla}\cdot\boldsymbol{\tau}_p = \mu\nabla^2\boldsymbol{u}$, and for a viscoplastic fluid we take the Bingham model (equation (2.17)).

The dimensionless variant of equation (2.12) is obtained by defining the reference velocity U as some average velocity, and the reference length L as the domain length

$$\boldsymbol{u} := U\overline{\boldsymbol{u}}, \quad \boldsymbol{x} := L\overline{\boldsymbol{x}}, \tag{2.21}$$

giving rise to the inertial time, inertial pressure, and friction relaxation time scales

$$t := \frac{L}{U}\overline{t}, \quad p := \rho U^2 \overline{p}, \quad \lambda := \frac{U}{L}\overline{\lambda}, \tag{2.22}$$

resulting in the dimensionless incompressible momentum conservation equations for an active fluid of Newtonian rheology

$$\text{Mechanical sector} \begin{cases} \dfrac{\mathrm{D}\boldsymbol{u}}{\mathrm{D}t} = -\boldsymbol{\nabla} p + \dfrac{1}{\mathrm{Re}}\boldsymbol{\nabla}\cdot\boldsymbol{\tau}_p - \dfrac{1}{\lambda}\boldsymbol{u} + \mathrm{Ac}\, C_1 \boldsymbol{\nabla} C_2, \\ \boldsymbol{\nabla}\cdot\boldsymbol{u} = 0. \end{cases} \tag{2.23}$$

Here, $\mathrm{Re} := LU\rho/\mu$ is the Reynolds number, a ratio of the inertial timescale to the viscous timescale. Physically, the inertial and viscous timescales are, respectively, the typical time for a chunk of fluid to move a distance L, and the typical time for viscosity to diffuse momentum over a distance L. We further define the activity parameter $\mathrm{Ac} := \alpha C_0^2/\rho U^2$, a ratio of the inertial forces and the forces due to the chemical gradients, and the Bingham number $\mathrm{Bi} := L\tau_0/U\mu_0$, a ratio of the yield-stress to the viscous stress.

Since the Reynolds number is dimensionless, it is invariant under a change of unit system. Therefore it is meaningful to talk of a large, or small Reynolds number. When the entire system of equations is made dimensionless, it is likewise independent of the choice of unit system. This allows one to construct model systems for physical systems that are otherwise impractical to build.

In all simulations and most analytical calculations, we will assume the unsteady stokes limit, in which the non-linear term representing the advection of the velocity field $\boldsymbol{u}\cdot\boldsymbol{\nabla}\boldsymbol{u}$ is neglected. This is akin to an intermediary regime between stokes flow—where the entire material derivative of the velocity field vanishes—and the fully inertial case of equation (2.23). Mechanically, the unsteady stokes limit has the material derivative of the velocity replaced with a partial derivative with respect to time. And physically, it represents a scenario in which inertial forces are very small compared to viscous ones, but not yet negligible.

The reaction-diffusion system now influences the fluid itself through the coupling to the momentum conservation equations, but if the chemicals exist on the substrate, they should be advected by it. So it is necessary to replace the partial time derivative of equation (1.18) with the material derivative, giving

$$\text{Chemical sector}\begin{cases}\dfrac{\mathrm{D}C_1}{\mathrm{D}t} = \dfrac{1}{\mathrm{Pe}_1}\nabla^2 C_1 + \mathrm{Da}_1 - (\mathrm{Da}_2+\mathrm{Da}_4)C_1 + \mathrm{Da}_3 C_1^2 C_2,\\ \dfrac{\mathrm{D}C_2}{\mathrm{D}t} = \dfrac{1}{\mathrm{Pe}_2}\nabla^2 C_2 + \mathrm{Da}_2 C_1 - \mathrm{Da}_3 C_1^2 C_2.\end{cases} \tag{2.24}$$

The Damköhler numbers must be re-defined to be consistent with the present reference scales

$$\mathrm{Da}_1 \coloneqq \frac{k_1 L A}{U C_0},\quad \mathrm{Da}_2 \coloneqq \frac{k_2 L B}{U},\quad \mathrm{Da}_3 \coloneqq \frac{k_3 L C_0^2}{U},\quad \mathrm{Da}_4 \coloneqq \frac{k_4 L}{U}, \tag{2.25}$$

and the diffusion coefficients have been replaced with the Péclet numbers, each a ratio of the diffusive time scales L^2/D_1 and L^2/D_2 to the advective time scale L/U,

$$\mathrm{Pe}_1 \coloneqq \frac{LU}{D_1},\quad \mathrm{Pe}_2 \coloneqq \frac{LU}{D_2}. \tag{2.26}$$

In order to reduce the dimensionality of this large parameter space, we will henceforth fix the Reynolds number and the friction relaxation time scale to unity, and the Damköhler numbers to $\mathrm{Da}_1 = 4.5$, $\mathrm{Da}_2 = 7.38$, $\mathrm{Da}_3 = \mathrm{Da}_4 = 1$. In the absence of the mechanical sector, this corresponds to the stripe pattern of the Brusselator, where $\chi = 0.1$. Lastly, the Péclet numbers will always be related by $\mathrm{Pe}_1 = 8\mathrm{Pe}_2$, such that the remaining free parameters of the mechano-chemical system are the Péclet number Pe_1, the activity parameter Ac, and the Bingham number Bi.

Linear stability. Assuming Newtonian rheology and defining again $\mathrm{Da}_1 = a$, $\mathrm{Da}_2 = b$, $\mathrm{Da}_3 = c$, and $\mathrm{Da}_4 = d$, we can write the above by defining a state vector $\psi := (C_1, C_2, u_x, u_y)$, explicitly separating the Brusselator subsystem A, the fluid flow subsystem D, and the couplings between the two, B and C:

$$\frac{\mathrm{d}\psi}{\mathrm{d}t} = \begin{pmatrix} \mathsf{A} & \mathsf{B} \\ \mathsf{C} & \mathsf{D} \end{pmatrix} \psi. \tag{2.27}$$

These subsystems, when linearised about their stationary steady-state, are given by

$$\mathsf{A} = \begin{pmatrix} b - d + \frac{1}{\mathrm{Pe}_1}\partial_i\partial_i & \frac{c}{d^2}a^2 \\ -b & -\frac{c}{d^2}a^2 + \frac{1}{\mathrm{Pe}_1}\partial_i\partial_i \end{pmatrix}, \qquad \mathsf{B} = 0, \tag{2.28}$$

$$\mathsf{C} = \begin{pmatrix} 0 & \mathrm{Ac}\frac{1}{d}a\partial_x \\ 0 & \mathrm{Ac}\frac{1}{d}a\partial_y \end{pmatrix}, \qquad \text{and} \quad \mathsf{D} = \begin{pmatrix} \frac{1}{\mathrm{Re}}\partial_i\partial_i - \frac{1}{\lambda} & 0 \\ 0 & \frac{1}{\mathrm{Re}}\partial_i\partial_i - \frac{1}{\lambda} \end{pmatrix}. \tag{2.29}$$

We see then that the advection term does not carry into the linearised Newtonian system, by which the coupling becomes one-way. Since viscoplasticity is a non-linear phenomenon, the conclusions carry over. In other words, the linear influence of the mechanical sector on the chemical sector, B, is zero.

Generation and dissipation of vorticity. Define $\boldsymbol{\Omega} = (0, 0, \Omega) = \boldsymbol{\nabla} \times \boldsymbol{u}$ such that when taking the curl of the system of equations, all pure gradients vanish. Taking the curl of the momentum equations results in

$$\frac{\partial \boldsymbol{\Omega}}{\partial t} + \boldsymbol{\nabla} \times (\boldsymbol{\Omega} \times \boldsymbol{u}) = \frac{1}{\mathrm{Re}}\nabla^2\boldsymbol{\Omega} - \frac{1}{\lambda}\boldsymbol{\Omega} + \mathrm{Ac}\,\boldsymbol{\nabla} \times (C_1 \boldsymbol{\nabla} C_2), \tag{2.30}$$

or equivalently,

$$\frac{\mathrm{D}\Omega}{\mathrm{D}t} = \frac{1}{\mathrm{Re}}\nabla^2\Omega - \frac{1}{\lambda}\Omega + \mathrm{Ac}\,\boldsymbol{\nabla} \times (C_1 \boldsymbol{\nabla} C_2). \tag{2.31}$$

This shows that the activity term is the generator of vorticity. Note that if C_1 can be written $f'(C_2)$ for some integrable function f, since $\boldsymbol{\nabla} f(C_2) = f'(C_2)\boldsymbol{\nabla} C_2$, the term generating vorticity will vanish.

Applying the vector calculus identity $\boldsymbol{\nabla} \times (C_1 \boldsymbol{\nabla} C_2) = C_1(\boldsymbol{\nabla} \times \boldsymbol{\nabla} C_2) - \boldsymbol{\nabla} C_2 \times (\boldsymbol{\nabla} C_1)$ to the activity term, and noting that the curl of a gradient is zero, we get

$$\frac{\mathrm{D}\Omega}{\mathrm{D}t} = \frac{1}{\mathrm{Re}}\nabla^2\Omega - \frac{1}{\lambda}\Omega + \mathrm{Ac}\,\boldsymbol{\nabla} C_2 \times \boldsymbol{\nabla} C_1 \tag{2.32}$$

$$= \frac{1}{\mathrm{Re}}\nabla^2\Omega - \frac{1}{\lambda}\Omega + \mathrm{Ac}\left(\frac{\partial C_1}{\partial x}\frac{\partial C_2}{\partial y} - \frac{\partial C_1}{\partial y}\frac{\partial C_2}{\partial x}\right), \tag{2.33}$$

from which it is apparent that the activity term is invariant under the simultaneous substitution of $x \leftrightarrow y$ and $C_1 \leftrightarrow C_2$.

To summarize, the active stress was found to be an effective pressure under some circumstances, and a generator of vorticity under others, giving the conditional relation

$$\boxed{\frac{\mathrm{D}\Omega}{\mathrm{D}t} = \begin{cases} \frac{1}{\mathrm{Re}}\nabla^2\Omega - \frac{1}{\lambda}\Omega & \text{if Newtonian and } \exists f\colon C_1 = f'(C_2), \\ \frac{1}{\mathrm{Re}}\nabla^2\Omega - \frac{1}{\lambda}\Omega + \mathrm{Ac}\,\boldsymbol{\nabla} C_2 \times \boldsymbol{\nabla} C_1 & \text{if } \nexists f\colon C_1 = f'(C_2). \end{cases}} \tag{2.34}$$

Which of the two cases is more likely depends on the dynamics of the substrate. A static substrate will not alter the dynamics of the chemical sector, hence the chemical concentration fields will evolve to the steady-state of the classical Brusselator system, for which observations suggest that there exists an integrable function f which satisfies $C_1 = f'(C_2)$. This condition may hold weakly for scenarios where flows are negligible (in that there may exist a function for which this equality approximately holds), in which case the active stress is expected to be in large part a pressure and in small part a generator of vorticity.

Notice that the generator of vorticity vanishes to linear order in perturbations of the chemical concentrations (see section 1.2.1). This means that vorticity cannot affect the initial pattern formation in the chemical concentration fields. But it does affect the non-linear late-stage evolution of the system. To see how, we first write the generator of vorticity as

$$\mathrm{Ac}\,\boldsymbol{\nabla} C_2 \times \boldsymbol{\nabla} C_1 = \mathrm{Ac}\,|\boldsymbol{\nabla} C_1||\boldsymbol{\nabla} C_2|\sin\theta, \tag{2.35}$$

where θ is the local angle of alignment of the gradients; where $\sin\theta = 0$ for parallel gradients, and $|\sin\theta| = 1$ for perpendicular gradients.

This formulation leads to the following observations:

1. where the gradients are perpendicular, vorticity is generated in a direction determined by the sign of the active force;
2. where the gradients are parallel to each other, vorticity is only dissipated and damped.

On a periodic domain, the classical Brusselator tends to a stationary steady-state where the gradients are anti-aligned, preventing the generation of vorticity. This gives rise to a metastable state of zero vorticity. Any deviation from this state that generates flow that disturbs the alignment of the chemical gradients will further distance the system from this metastable state. It is unlikely that the system will come back to that state again, as that requires the global alignment of the gradients at a point in time where the vorticity field is everywhere negligible. Hence, the chemical concentrations are expected to evolve without rest.

Since the generated vorticity is stronger for a steeper gradient in the chemical concentration, it is expected that a larger Péclet number will result in a stronger vorticity field.

To see this, compare the role of the Péclet number in the chemical system to the role of the diffusion coefficient in the classical Brusselator: the spatial wavelength of the emerging patterns grows smaller with increasing Péclet number. Hence, the gradients grow larger, and vorticity is generated faster, suggesting the relation

$$\boxed{\Omega \sim \mathrm{Ac}\,\mathrm{Pe}_1.} \tag{2.36}$$

If the advection of the chemical fields is neglected, then it becomes possible to obtain an explicit steady-state solution for the vorticity field in the unsteady stokes limit, e.g., a solution to the inhomogeneous Helmholtz equation

$$\left(\nabla^2 + \kappa^2\right)\Omega(\boldsymbol{r}) = S(\boldsymbol{r}), \tag{2.37}$$

where S is a source term with compact support. We identify

$$S = -\mathrm{Ac}\,\mathrm{Re}\boldsymbol{\nabla} C_2 \times \boldsymbol{\nabla} C_1, \tag{2.38}$$

$$\kappa^2 = -\frac{\mathrm{Re}}{\lambda}. \tag{2.39}$$

In the case of homogeneous or periodic boundary conditions, the vorticity field can be written in terms of the Green's function G as the convolution of this function with the source term. The Green's function satisfies

$$\left(\nabla^2 - \frac{\mathrm{Re}}{\lambda}\right) G = \delta(\boldsymbol{r} - \boldsymbol{r}'), \tag{2.40}$$

where δ is the Dirac delta function.

Furthermore, for periodic boundary conditions we already know the eigenfunctions of the Laplacian operator: they are the harmonic modes. By the convolution theorem, the convolution of the source term with the Green's function is equivalent to multiplication of the Fourier transformed functions. Further assuming isotropy, the Fourier transform of the above entails the substitutions $\nabla^2 \leftarrow k^2$ and $\delta \leftarrow 1$.

Let $\mathfrak{F}\{f(t)\}$ denote the Fourier transform of the function $f(t)$, and let $\mathfrak{F}^{-1}\{\cdot\}$ be its inverse. The solution is then given by

$$\Omega = \mathrm{Ac}\,\mathrm{Re}\,\mathfrak{F}^{-1}\left\{\frac{\mathfrak{F}\{\boldsymbol{\nabla} C_2 \times \boldsymbol{\nabla} C_1\}}{\mathrm{Re}/\lambda - k^2}\right\}. \tag{2.41}$$

One can think of this solution as the source term with a Gaussian frequency filter applied to it. The filter amplifies spatial frequencies in the vicinity of $k^\star = \sqrt{\mathrm{Re}/\lambda}$.

Since this solution is only valid when the chemical sector is not influenced by the mechanical, it is not expected to be observed in simulations. Nonetheless, one can intuit that at each moment, the mechanical sector acts so as to bring itself closer

to this solution. The ensuing effect on the chemical sector, however, immediately alters the source term, thereby shifting the goal. To summarise, we may say that the mechanical sector has a natural wavenumber—$k^\star$.

Solution for a static substrate. Let's consider another simplified case, where we again take the unsteady stokes limit. Let us further assume a static substrate or negligible flow. In this case, a viscoplastic fluid of any non-negligible yield-stress will be arrested over the entire domain, so we will also consider Newtonian rheology for the present moment. This is in fact the more general approach, as the viscoplastic passive stress tensor vanishes under these conditions.

As a consequence of the negligible flow, the chemicals will not be affected by the momentum equation, and the solution to the chemical sector will remain unchanged (e.g. it is still the solution to the Brusselator system). Therefore we may assume that there exists an integrable function f which satisfies $C_1 = f'(C_2)$. In this case, the activity term can be written as a pure gradient, and the active stress can be absorbed into the pressure. We can also neglect friction, as the velocity is assumed negligible, giving

$$\frac{\partial \boldsymbol{u}}{\partial t} = -\boldsymbol{\nabla}\left(p - \frac{\mathrm{Ac}}{2}C_1^2\right) + \frac{1}{\mathrm{Re}}\nabla^2\boldsymbol{u}, \tag{2.42}$$

$$\boldsymbol{\nabla}\cdot\boldsymbol{u} = 0. \tag{2.43}$$

Note that even if the velocity is negligible, variations in the velocity can be quite high, so related terms must be carried along.

Taking the curl of the momentum equation above, and using the fact that the curl of the Laplacian is zero and likewise for the curl of the gradient, we infer that $\partial_t \boldsymbol{\nabla}\times\boldsymbol{u} = 0$. We take the initial velocity to be zero, and thus can deduce that the flow will remain irrotational forever.

We can use the incompressibility condition to solve for the pressure by taking the divergence of the momentum equation, and enforcing that the velocity is constant in time (assuming such a solution exists). This yields the Poisson equation

$$\nabla^2\left(p - \frac{\mathrm{Ac}}{2}C_1^2\right) = 0. \tag{2.44}$$

The strong maximum principle states that unless the parenthesised part above is constant, its maximum must lie on the boundary $\partial\mathscr{D}$ and cannot lie on the bulk $\mathscr{D}$. But $\mathscr{D}$ is topologically equivalent to a torus, which has no boundaries. Therefore, the solution to the Poisson equation is requires the term in the brackets to be constant. But we are only interested in gradients of the pressure, so we may pick the constant to be zero.

Plugging this pressure back into the momentum equation results in

$$\frac{\partial \boldsymbol{u}}{\partial t} = \frac{1}{\mathrm{Re}} \nabla^2 \boldsymbol{u}, \tag{2.45}$$

and the steady-state solution is obtained by solving the Poisson equation $\nabla^2 \boldsymbol{u} = 0$. But by the strong maximum principle, the only solution is a constant velocity field. This gives us the solution to the pressure and velocity fields in the case of a static substrate

$$\begin{aligned} p &= \frac{\mathrm{Ac}}{2} C_1^2, \\ \boldsymbol{u} &= \text{const.}, \end{aligned} \qquad \text{(static substrate).} \tag{2.46}$$

which will be compared to a numerical solution at a later point.

Dynamics on a fluid substrate. Allowing the morphogens to be advected by the flow field that their gradients generates, we arrive in a situation in which the reaction-diffusion subsystem is definitely affected by the momentum equation. We therefore no longer know the relation between C_1 and C_2 at steady-state, if such a steady-state even exists. The only modification to the reaction-diffusion subsystem is that the chemicals are now advected with the flow. But if the velocity is zero, then the above solution would apply here too. The question is then whether this solution is stable in the presence of a small perturbation in the velocity, or whether the reaction-diffusion subsystem will converge to its usual solution before a velocity field develops, thus preventing acceleration and therefore deviation from this state.

Consider a phase space diagram of Pe_1 against Ac. For very large Ac, we expect the velocity to build up very slowly, since the acceleration due to the active stress is small, and vice versa. Now recall that the critical wavenumber of the classical Brusselator is given by equation (1.10). Since $\mathrm{Pe}_2 = \mathrm{Pe}_1/8$, we can infer that $k_c^2 \propto \mathrm{Pe}_1$, and that for large Pe_1, the patterns that form are of fine features. And since the activity term is proportional to $\boldsymbol{\nabla} C_2$, we expect it to vanish in the limit $\mathrm{Pe}_1 \to 0$.

For viscoplastic rheology, it is to be expected that as the magnitude of the coefficient of the activity term |Ac| is increased, more deformation will occur, and as such the mean of the deformation tensor magnitude $\langle \left| \mathbf{II}_{\dot{\gamma}} \right| \rangle$ will increase. It is also expected that as the Bingham number Bi is increased, a stronger force will be needed to deform the fluid substantially.

The equations of the mechanical sector suggest that the evolution of a uniform velocity field would be governed by the active stress term. Assuming that the velocity field is zero everywhere initially, the chemical sector is expected to evolve (by a good approximation) as if on a static substrate. But eventually, the active stress would have contributed substantially to the velocity field, and the substrate will yield. One therefore expects a scaling relation akin to

$$|\mathbf{II}_\tau| \sim \mathrm{Bi} \left| \mathbf{II}_{\dot{\gamma}} \right|^{1/2} \sim |\mathrm{Ac}|\, C_1 \boldsymbol{\nabla} C_2, \tag{2.47}$$

and that therefore

$$\boxed{\left|\mathbf{II}_{\dot{\gamma}}\right|^{1/2} \sim \frac{|\mathrm{Ac}|}{\mathrm{Bi}}.} \tag{2.48}$$

Chapter 3

Direct Numerical Simulations

All of the numerical experiments will be performed using the partial differential equation solver Basilisk[10], the successor of Gerris. Basilisk implements the language "Basilisk C", which extends the C programming language (Basilisk C transpiles to C99); it is tailored for writing discretisation schemes on Cartesian grids. A brief introduction to the Basilisk C language is provided in appendix F.

The simulation output will be processed in the programming language Julia[44], since it offers a mature read-eval-print loop (REPL), which allows for rapid development, and since it provides macros, which enables the creation of a more succinct domain specific language (DSL) for inter-operation with Basilisk.

3.1 Validation

Simulation results from Basilisk are exported to disk as binary files encoding fields such as velocity and chemical concentration. Before running any experiment, it is necessary to verify that this saving and loading of data occurs according to expectation.

To that end, we arbitrarily define a bump function and calculate its gradient using Basilisk, once using cell-centered vector fields, and once using face-centered vector fields. We use a second order finite difference scheme, and compare the results with a calculation done purely in Julia, and with the value of the derivative sampled from the analytical solution on the same grid. The results are found to be equivalent up to machine precision (see appendix E), so we may progress to verify a classic test case.

Poiseuille flow. Here we will simulate flow in a long channel. The full problem was studied by Hagen in 1839 and Poiseuille in 1840, and as such it is called the Poiseuille flow problem[34]. In two-dimensions, it reduces to flow in a channel—the cross-section of a tube. We will consider an incompressible Newtonian fluid, governed by the equations

$$\frac{\mathrm{D}\boldsymbol{u}}{\mathrm{D}t} = -\boldsymbol{\nabla} p + \frac{1}{\mathrm{Re}}\nabla^2 \boldsymbol{u}, \tag{3.1}$$

$$\boldsymbol{\nabla}\cdot\boldsymbol{u} = 0, \tag{3.2}$$

where $\mathrm{Re} := \rho U H/\mu$ is the Reynolds number, U is a reference viscosity, and H is the channel half-height.

We enforce a linear pressure gradient between the ends of the channel to stimulate flow

$$\frac{\mathrm{d}p}{\mathrm{d}x} = -\frac{\Delta P}{L}. \tag{3.3}$$

Since the pressure gradient is along the x direction, we suppose that the flow is directed purely along the length of the pipe ($\boldsymbol{u} = (u_x, 0)$). The incompressibility condition coupled with the no-slip boundary conditions then implies that $u_x(x,y) = u_x(y)$. The momentum equation then reduces to

$$\frac{1}{\mathrm{Re}} u_x'' = p' = -\frac{\Delta P}{L}, \tag{3.4}$$

with as solution

$$u_x(y) = -\left(\frac{\mathrm{Re}\Delta P}{2L} y + C_1\right) y + C_2. \tag{3.5}$$

Now in the possession of an analytical solution to the flow profile, we implement a simulation for this problem and compare the analytical solution to the numerical. We base this simulation on the `navier-stokes/centered` solver.

```
#include "navier-stokes/centered.h"
```

This solver approximates the incompressible, variable-density Navier-Stokes equations

$$\rho\frac{\mathrm{D}\boldsymbol{u}}{\mathrm{D}t} = -\boldsymbol{\nabla} p + \mu\nabla^2\boldsymbol{u} + \boldsymbol{a}, \tag{3.6}$$

$$\boldsymbol{\nabla}\cdot\boldsymbol{u} = 0, \tag{3.7}$$

where μ is the kinematic viscosity, ρ is the variable density, and $\boldsymbol{a}$ is an acceleration term. The approximation is second-order accurate.

Since we solve the dimensionless equations, we need to instruct Basilisk that the domain size `L0` and time step `DT` are unitless. * This we do by assigning them the dimensional index 0. We additionally center the y coordinate.

* Core variables such as these are better set with compiler arguments, which we denote by a prefix M. This avoids side effects due in the parsing of the Basilisk C code, because compiler arguments bypass this step altogether.

```
int main(int argc, char * argv[]) {
  L0 = ML [0]; // unit [x^0] = [1] = [unitless]
  origin(0, -L0/2.0);

  init_grid(1 << 7); // 2^7

  DT = 1e-1 [0];
```

We then initialise the viscosity variable `mu`, and call `run()`. This will kick off the simulation when the program is executed.

```
  mu   = new face vector;
  mu[] = {1.0/Re, 1.0/Re}; // load Re from argv

  run();
}
```

We declare the boundary conditions and initial values in an `init` event, which should be called once before the first iteration. The geometry is a long channel of height 2, so we declare a mask * which sets to the region $y < -1$ the value `bottom`, and to the region $y > 1$ the value `top`. In this way we have defined the location of the top and bottom boundaries.

```
event init(i = 0) {
  mask(y < -1.0 ? bottom : (y > 1.0 ? top : none));
```

We now declare Neumann boundary conditions for the x component of the velocity field on both ends of the channel: $\partial_n u|_{x=0} = \partial_n u|_{x=L} = 0$ with $\boldsymbol{u} = (u, v)$. Basilisk C defines a shorthand for the normal component of a vector: instead of specifying `u.x[left]` and `u.x[right]`, we can write `u.n[left]` and `u.n[right]`, and the correct component of $\boldsymbol{u}$ will be selected based on the specified boundary.

```
  u.n[left]  = neumann(0);
  u.n[right] = neumann(0);
```

We also set Dirichlet boundary conditions on the velocity field at the top and bottom of the channel: $a|_{y=\pm 1} = 0$ where $a \in \{u, v\}$, using the shorthand for the tangential component `u.t`. And lastly, we set Dirichlet boundary conditions on the pressure field at the right side of the channel, $p|_{y=1} = 0$, and at the left, $p|_{y=-1} = \Delta p = 1$.

```
  u.n[top]    = dirichlet(0);
  u.t[top]    = dirichlet(0);
  u.n[bottom] = dirichlet(0);
  u.t[bottom] = dirichlet(0);

  p[left]  = dirichlet(MDeltaP);
  p[right] = dirichlet(0);
}
```

* The implementation of the function mask is known to be error prone for anything but very simple geometries, and as such should be avoided when possible. Specifically, mask should only be used for boundaries that are aligned with the cells. One should otherwise use the embed header instead.

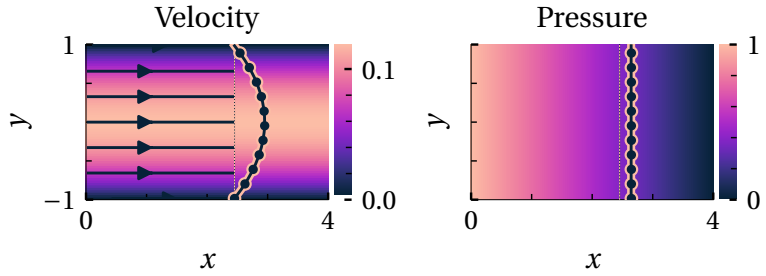

Figure 3.1: (a) The velocity field, depicted as a heatmap representing the magnitude of the field, overlayed with a streamplot, and a cross section of the field. The cross section consists of the (subsampled) numerical data as a scatter plot, and the analytical prediction as a solid graph. (b) The pressure field. The numerical value of both fields converges to the analytical prediction.

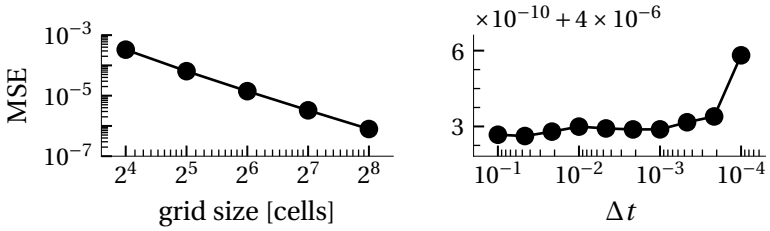

Figure 3.2: The mean square error of the numerical solution with respect to the analytical decreases as the grid resolution is increased (left), and is relatively constant with decreasing timestep size (right).

When the simulation is finished, we should like to save the value of the velocity and pressure fields. But only the region occupied by the channel is of interest, so we define the corresponding rectangular bounding box.

```
event final(t = end) {
  //                          -----------(X2, Y2)
  //                                channel
  //                          (X1, Y1)-----------
  coord bounding_box[2] = {{0, -1.0}, {L0, 1.0}};
  output_matrix(p, box=bounding_box, file="p") // likewise for u.x and u.y
}
```

This test case can be extended to verify that a body force such as the activity term $\boldsymbol{f}_\alpha$ drives the flow as expected. For the present case we will assume that the activity term amounts to a correction to the pressure. It stands to reason that if we set the pressure to zero and require that $C_1^2 = -x\Delta p/L$, we should recover a pressure field identical to that of the previous simulation.

The only changes to be made are: redeclaring the acceleration term as variable in the `centered` solver so we may assign it a value, setting Neumann a boundary condition on the left opening of the channel, and constructing the field $\phi \equiv -x\Delta p/L$.

```
int main(int argc, char * argv[]) {
  ...
```

```
  a = new face vector; // must be called after init_grid()
  ...
}

event init(i = 0) {
  ...

  p[left] = neumann(0);

  foreach() {
    phi[] = MDeltaP * x / L0;
  }
  phi[left]  = dirichlet(0);
  phi[right] = dirichlet(MDeltaP);
}
```

Finally we hook into the acceleration event defined in the `centered` solver to set the value of the acceleration field. * Since it is a face vector field, we iterate over the stencil using `foreach_face`. And since we only wish to set the x component, we iterate using `foreach_face(x)`. We can use the predefined gradient function for `foreach_face` loops, `face_gradient_x`. Refer to appendix F for more details.

```
event acceleration(i++) {
  foreach_face(x) {
    a.x[] += face_gradient_x(phi, 0);
  }
}
```

Indeed, the results are identical to the pressure driven case. We have arbitrarily decided to terminate the simulation once the velocity field changed less than a multiple of 1×10^{-5} of its value at the previous iteration, at which the pressure field was a perfect gradient up to deviations from an ideal gradient of the order of 1×10^{-7}.

Poiseuille flow of a viscoplastic fluid. In order to validate the viscoplastic rheology implementation, we compare an analytical solution to the Poiseuille flow problem with a numerical solution for the limiting case of a Bingham fluid, that is, we take $n \to 1$ in the Herschel-Bulkley model.

We implement this model in Basilisk by extending the `two-phase` solver to reflect the deviatoric stress tensor of a Herschel-Bulkley fluid. First, we declare and initialise the variables and fields.

```
#include "vof.h"

scalar f[], * interfaces = {f};

double rho1 = 1.0, rho2 = 1.0;
double mu1  = 0.0, mu2  = 0.0;
double tauy = 0.0;
double n    = 1;
```

* We add to the acceleration field as opposed to just setting its value, so to avoid interfering with other solvers. This is a good practice, but not strictly necessary here.

```
double vp_regularization = 1e-3;

event defaults(i = 0) {
  alpha = new face vector; // (variable) specific volume alpha=1/rho
  rho   = new scalar; // cell-centered density

  if (mu1 || mu2) {
    mu = new face vector; // face-centered viscosity field
  }
}
```

Then, we define a macro to interpolate the value of fluid properties across the interfaces using a simple arithmetic average. We smear the sharp interface by defining a smeared fraction field `sf`, which is the vertex averaged fraction `f`. We will say more on the subject of interfaces shortly, but for now it suffices to think of these as the layer separating two fluids, like olive and water, for example.

```
// The density and viscosity are defined using arithmetic averages by
// default. The user can overload these definitions to use other types of
// averages (i.e. harmonic).
#define fraction_interp(f, a, b) (clamp(f, 0., 1.) * (a - b) + b)

scalar sf[]; // we "smear" the density/viscosity jump

event tracer_advection(i++) {
  foreach() { // we initialise sf with the vertex-average of f
    sf[] = (4.0 * f[] +
                2.0 * (f[0,1] + f[0,-1] + f[1,0] + f[-1,0]) +
                f[-1,-1] + f[1,-1] + f[1,1] + f[-1,1]) / 16.0;
  }
}
```

We now define three variations of the second order accurate derivative of a field `a` with respect to the coordinate y, each of which can be evaluated at an arbitrary offset from a given cell:

`face_gradient_displaced_y` the value of which is defined at cell centers;

`center_gradient_displaced_y` defined at cell faces; and

`face_gradient_trans_y` defined at cell centers, and averaged across two consecutive cells.

```
// face_gradient_x(a, i), predefined
// 2nd order accurate derivative of a wrt x
// offset on x by i faces
// when i=0, value is defined at cell center

// 2nd order accurate derivative of a wrt y
// offset on y by i faces and on x by j faces
// when i=j=0, value is defined at cell center
#define face_gradient_displaced_y(a,i,j) ((a[j,i] - a[j,i-1]) / Delta)

// 2nd order accurate derivative of a wrt y
```

```
// offset on y by i faces and on x by j faces
// when i=j=0, value is defined at cell face
#define center_gradient_displaced_y(a,i,j)      \
  ((face_gradient_displaced_y(a,i,j) +          \
    face_gradient_displaced_y(a,i+1,j)) / 2.)

// 2nd order accurate derivative of a wrt y (averaged)
// offset on y by i faces
// when i=0, value is defined at cell center
#define face_gradient_trans_y(a,i)                  \
  ((center_gradient_displaced_y(a, i, 0) +          \
    center_gradient_displaced_y(a, i, -1)) / 2.)
```

These definitions allow us to write the deformation tensor

$$\dot{\gamma} = \begin{pmatrix} \frac{\mathrm{d}u}{\mathrm{d}x} & \frac{1}{2}\left(\frac{\mathrm{d}v}{\mathrm{d}x} + \frac{\mathrm{d}u}{\mathrm{d}y}\right) \\ \frac{1}{2}\left(\frac{\mathrm{d}v}{\mathrm{d}x} + \frac{\mathrm{d}u}{\mathrm{d}y}\right) & \frac{\mathrm{d}v}{\mathrm{d}y} \end{pmatrix} \tag{3.8}$$

directly in terms of its constituent primitives. The deviatoric stress tensor is then given by equation (2.18), and calculated in an event named `properties`. After calculating the new values of the various fields, it is necessary to re-apply the boundary conditions, which we do with a call to the `boundary` function.

```
face vector D_second_inv[]; // second invariant of deformation tensor

event properties(i++) {
  if (mu1 || mu2) {
    foreach_face() {
      // u_vector = (u.x, u.y) = (u, v)
      double dudx = face_gradient_x(u.x, 0);
      double dvdx = face_gradient_x(u.y, 0);
      double dudy = face_gradient_trans_y(u.x, 0);
      double dvdy = face_gradient_trans_y(u.y, 0);

      double D11 = dudx;
      double D22 = dvdy;
      double D12 = (dvdx + dudy) / 2.0;

      D_second_inv.x[] = sqrt(sq(D11) + sq(D22) + 2.0 * sq(D12));
    }

    (const) face vector mu_hb = unityf;
    if (n != 1) {
      mu_hb = new face vector;
      foreach_face() {
        mu_hb.x[] = pow(sqrt(2.) * D_second_inv.x[], n - 1);
      }
    }

    foreach_face() {
      double m = 1.0 / vp_regularization;
      double Dsi = D_second_inv.x[];
      double apparent_visc =
```

```
        (mu1 * mu_hb.x[]
         + tauy / (sqrt(2) * Dsi + 1e-10) * (1.0 - exp(-m * Dsi)));

      double ff = face_value(sf, 0);
      mu.x[] = fm.x[] * fraction_interp(ff, apparent_visc, mu2);
    }
  }

  foreach_face() {
    double ff = face_value(sf, 0);
    alpha.x[] = fm.x[] / fraction_interp(ff, rho1, rho2);
  }

  foreach() {
    rho[] = cm[] * fraction_interp(sf[], rho1, rho2);
  }

  boundary((scalar *){mu, D_second_inv.x, D_second_inv.y, alpha, rho});
}
```

For one-dimensional flow this model simplifies to

$$\tau_{xy} = \left[1 + \frac{\left(1 - e^{-m|u'_x|}\right)\mathrm{Bi}}{|u'_x|}\right] u'_x. \tag{3.9}$$

Since the problem is symmetric across the length of the channel, it suffices to find a solution for half of the height of the channel. We continue with the half for which $|u'_x| = u'_x$, and we work in vertically centered coordinates aligned to the left of the channel.

Like in the Newtonian Poiseuille flow problem, in terms of the dynamic pressure $p/U^2\rho$, the momentum equation reduces to

$$\frac{2}{\mathrm{Re}}\frac{\mathrm{d}}{\mathrm{d}y}\left[\mu(u'_x)u'_x\right] = p' = -\frac{\Delta P}{L}, \tag{3.10}$$

or since in this case $\mu(u'_x) = 1 + \mathrm{Bi}/u'_x$,

$$u''_x = -\frac{\mathrm{Re}\,\Delta P}{2L}. \tag{3.11}$$

In the yielded region, the solution to the above is

$$u_x(y) = -\frac{\mathrm{Re}\Delta P}{2L}(y + C_1)y + C_2. \tag{3.12}$$

The boundary conditions impose that $u_x(y_p) = u_p$ and $u_x(1) = 0$. But the solution must be continuous and smooth across the plug-yield interface, therefore $u'_x(y_p) = 0$ and

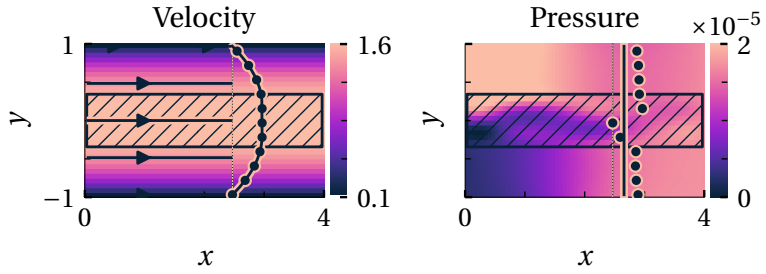

Figure 3.3: Continuation of figure 3.1 for the viscoplastic case. (a) The velocity field, overlayed with a dashed region representing the plug (effectively arrested domain). (b) The pressure field.

$$u_x(y) = \begin{cases} -\frac{\mathrm{Re}\Delta P}{2L}(y-1)(y-2y_p+1) & \text{if } y > y_p, \\ u_x(y_p) & \text{otherwise.} \end{cases} \tag{3.13}$$

Equating the forces acting on a test area centered in the channel, of height $2y_p$ and length $\mathrm{d}x$, gives

$$2y_p \mathrm{d}x \frac{\Delta P}{L} = 2\mathrm{d}x \frac{\tau_{xy}(y_p)}{\mathrm{Re}}, \tag{3.14}$$

which in combination with $\tau_{xy}(y_p) = u_x'(y_p) + \mathrm{Bi} = \mathrm{Bi}$ gives

$$y_p = \frac{L}{\Delta P}\frac{\mathrm{Bi}}{\mathrm{Re}}. \tag{3.15}$$

We include the new solver and initialise it with a yield stress and a regularisation parameter. The simulation is otherwise identical to the Newtonian case.

```
// remove: #include "two-phase.h"
#include "two-phase-hb.h"

int main(int argc, char * argv[]) {
  vp_regularization = 1e-3; // a reasonable default
  tauy = Bi; // load Bi from argv
  ...
}

scalar vector_to_scalar(vector a) {
  return * ((scalar *) ((vector *) {a}));
}

event final(t = end) {
  ...

  scalar Dnorm = vector_to_scalar(D_second_inv);
  save_field(Dnorm);
}
```

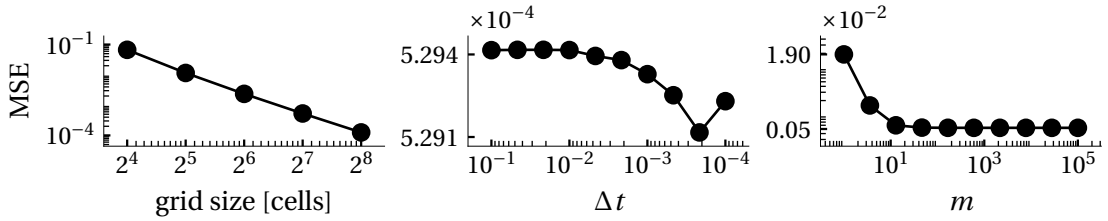

Figure 3.4: The mean square error (MSE) of the numerical solution with respect to the analytical decreases as the grid resolution is increased (first from left); decreases with decreasing timestep up to a small enough value, after which the MSE increases again (second from left); and the MSE decreases with increasing regularisation parameter m (third from left).

Besides picking an appropriate grid resolution or time step—that is, just small enough for the required accuracy, but no smaller—a proper value must be picked for the regularisation parameter m. A parameter sweep reveals that a value of 1×10^{-3} suffices for this problem (figure 3.4). But this will differ as the problem statement is altered, for example by changing the geometry, boundary conditions, or driving forces. It is therefore necessary to repeat this measurement for each problem statement. But to avoid cluttering the narrative, the choices made for these values will be tabulated in appendix C.

3.2 Numerical Integration of the Chemical Sector

The Poiseuille flow problem served as a test for the numerical integration program, since it was possible to find an analytical solution to compare the results to. The same program can be modified to integrate the Brusselator system.

We will integrate the dimensionless Brusselator system on a two-way periodic domain $\mathscr{D} = \mathbb{T}^2$ of size $L \times L$ (see equation (1.18)). The independent parameters of this system are the diffusion coefficient ratio $D = D_2/D_1$, and the four Damköhler numbers $\mathrm{Da}_{1,2,3,4}$. Analogously to the mechano-chemical system, we set $\mathrm{Da}_1 = 4.5$, $D_1 = 1$, $D = 8$, and the third and fourth Damköhler numbers will be taken to be unity. The only remaining free parameter of the reaction-diffusion system is the bifurcation parameter

$$\chi = \frac{\mathrm{Da}_2 - \mathrm{Da}_2^{(\mathrm{crit})}}{\mathrm{Da}_2^{(\mathrm{crit})}}. \tag{3.16}$$

For this simulation, we will make use of the `diffusion` solver, which solves the reaction-diffusion equation

$$\theta \frac{\partial f}{\partial t} = \boldsymbol{\nabla} \cdot \left(D_b \boldsymbol{\nabla} f \right) + \beta f + r, \tag{3.17}$$

where $\beta f + r$ is a reactive term, D_b is the diffusion coefficient, and θ can be interpreted as a density term. For the present case, we identify $\theta = 1$, and two instances of the above equation:

$$\frac{\partial C_1}{\partial t} = \nabla \cdot (\nabla C_1) + \overbrace{(C_1 C_2 - \mathrm{Da}_2 - 1)}^{\beta} \overbrace{C_1}^{f} + \overbrace{4.5}^{r}, \tag{3.18}$$

$$\frac{\partial C_2}{\partial t} = \nabla \cdot (D \nabla C_2) \underbrace{- C_1^2}_{\beta} \underbrace{C_2}_{f} + \underbrace{\mathrm{Da}_2 C_1}_{r}. \tag{3.19}$$

Unlike the `centered` solver, the `diffusion` solver does not imply the inclusion of the `run` header, so we include the latter explicitly.

```
#include "diffusion.h"
#include "run.h"
```

We declare the concentration fields of the two chemicals, the Brusselator parameter Da_2, and the diffusion coefficient ratio D.

```
scalar C1[], C2[];

double Da2 = 6.0;
double D   = 8.0;
```

The `main` function is written much like before, so we skip ahead to the `init` event, where we declare two-way periodic boundary conditions, set the initial value of the concentration fields to their homogeneous steady-state with a small amplitude noise perturbation, and initialise the random number generator with an unknown seed.

```
event init(i = 0) {
  periodic(left); periodic(top);

  srand(time(NULL));

  foreach() {
    C1[] = Da1 / Da4;
    C2[] = (Da2 / Da1) * (Da4 / Da3) + 0.01 * noise();
  }
}
```

To use the `diffusion` header, we call the `diffusion` function at every iteration. We do need to take care to set the timestep using the same scheme that the momentum equation solver uses, for consistency.

```
event integration(i++) {
  dt = dtnext(DT);

  scalar r[], beta[];
  foreach() {
    r[]    = Da1;
    beta[] = Da3 * C1[]*C2[] - Da2 - Da4;
  }
  diffusion(C1, dt, r=r, beta=beta);

  foreach() {
```

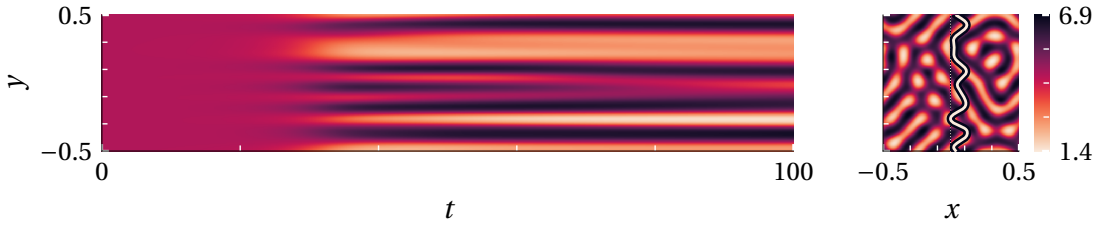

Figure 3.5: The concentration of C_1 at the final timestep (left), and the value of the former along the right edge as a function of time (right). The chemicals evolve according to the classical Brusselator equations, with no coupling to a momentum equation. For simulation parameters refer to row 2 of appendix C.

```
    r[]    = Da2 * C1[];
    beta[] = - Da3 * sq(C1[]);
  }
  const face vector d[] = {D, D};
  diffusion(C2, dt, d, r=r, beta=beta);
}
```

We then save the chemical concentration fields at the end of the simulation. The results are presented in appendix E. Only C_1 is depicted since it has been observed that C_2 roughly is equal to C_1 up to normalisation, by which it is meant that $C_2 \approx aC_1 + b$ with arbitrary constants a and b, or alternatively, $\tilde{C}_2 \approx \tilde{C}_1$. It is observed that $\left|\tilde{C}_1 - (1 - \tilde{C}_2)\right| \approx 0.1$, from which we infer that C_1 equals C_2 up to normalisation with an error of 10% (figure E.3).

Two programs have been created so far: one that can solve the momentum conservation equations for an incompressible Newtonian fluid, and one that can integrate the Brusselator system on a static substrate. The following section will detail the formation of a program that solves the reaction-diffusion system on a flowing substrate, making this a reaction-diffusion-advection system. To complete the coupling between the mechanical and chemical sectors, we will let chemical concentration gradients generate flow via an active stress.

3.3 Coupling the Mechanical and Chemical Sectors

It is useful to first analyse the effects of the active stress in the absence of advection, to gain a clearer picture. We will therefore continue with the program that integrates the Brusselator on a static substrate. A spatio-temporal plot of C_1 shows that this program eventually converges to a quasi-stationary state (figure 3.5). But this will no longer be the case once the chemicals are allowed to advect and the flow is accelerated by gradients in the chemical concentrations.

Since the substrate is static, we may let the chemical sector evolve while neglecting the activity term, greatly reducing the simulation runtime. Once the reaction-diffusion subsystem reaches a quasi-stationary state, the activity term is considered and the entire system is allowed to evolve until it reaches a stationary state.

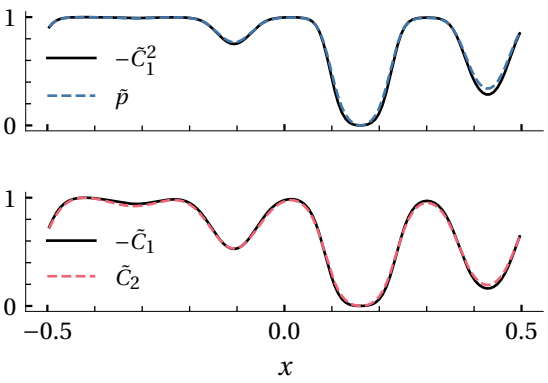

Figure 3.6: (top) A normalized slice of the pressure field plotted against a normalized slice of the first chemical's concentration squared shows that p is approximately proportional to C_1^2. (bottom) A similar plot but for $\tilde{C}_1$ and $\tilde{C}_2$. Numerical integration where C_2 is forced to be proportional to C_1 up to a constant results in exact proportionality between p and C_1^2.

Taking the program of section 3.2 as a basis, we include the `centered` solver and hook into its acceleration event to implement the activity term $\boldsymbol{f}_\alpha$.

```
#include "navier-stokes/centered.h"

double t0 = 3000.0 [0]; // once t > t0, we allow the fluid to be accelerated

double alph = 1.0; // coefficient of the activity term
// the above is not called alpha to avoid collision with an existing variable

... // define reaction rates k1, k2, k3, k4; diffusion coefficients D1, D2

event acceleration(i++) {
  if (t > t0) {
    foreach_face() {
      a.x[] += alph * face_value(C1, 0) * face_gradient_x(C2, 0);
    }
  }
}
```

It is critical to account for the differing stencil representations of the different fields. The concentration fields are defined on grid centers but the acceleration field is defined on grid faces; one could calculate the relation between the two, but there exists utility functions to handle this already. We use `face_value` to access a variable defined on grid centers inside a `foreach_face` loop, and likewise `face_gradient_x` for the second order accurate derivative with respect to `x`. *

There is one subtlety to note, namely that we let the chemical sector evolve to a quasi-stationary state before introducing the activity term in the simulation. While it appears that there exists a function f such that $C_1 = f'(C_2)$ at steady-state, and that therefore the vorticity generator vanishes, this is not the case at early times. The numerical solution to the velocity and pressure fields is therefore an approximation unless the system has reached a stationary steady-state. When the relation between C_1 and C_2 is artificially enforced, the results are found to be similar to the case presented here and show that $\tilde{p} = \tilde{C}_1^2$ exactly (see figure 3.6). Such an approximate solution is furthermore useful as it helps build intuition about the system.

* Functions ending with the suffix x result in the generation of corresponding code for the other dimensions (in this case, y).

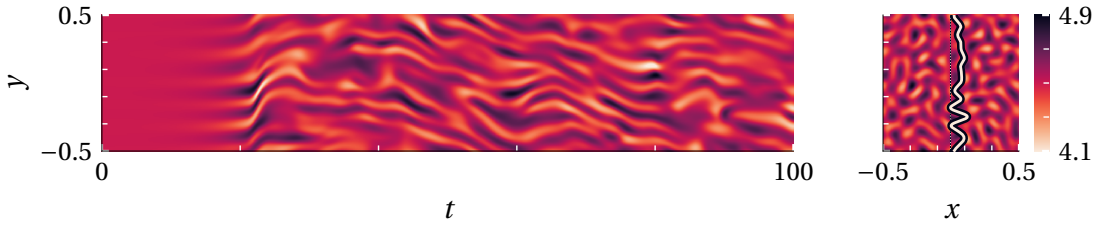

Figure 3.7: The concentration of C_1 at the final timestep (right), and the value of the former along the dashed line as a function of time (left). The chemicals evolve according to the classical Brusselator equations, with two-way coupling to the momentum equation. After a transient period of about twenty time units, a spatial pattern spontaniously develops in C_1. For simulation parameters refer to row 4 of appendix C.

Advection of the chemicals. Extending the existing program, we introduce the `tracer` solver which integrates the advection equation

$$\frac{\partial C_n}{\partial t} + \boldsymbol{u} \cdot \boldsymbol{\nabla} C_n = 0, \tag{3.20}$$

where C_n is a tracer: a field that is advected by the velocity field $\boldsymbol{u}$. This solver exposes the list `tracers`, which we set to include the two morphogens C_1 and C_2.

```
#include "tracer.h"

scalar * tracers = {C1, C2}; // advect C1 and C2
```

The rest of the code is largely unchanged, with the exception of two points. First, the `tracer` header provides the `tracer_diffusion` event, which we must use instead of our arbitrarily named `integration` event in order to solve the diffusion equation. And second, since we are considering unsteady Stokes flow, we must set the `stokes` variable to `true`.

But this prevents the `centered` solver from reducing the time-step when the velocity field grows, requiring the manual invocation of the suppressed function. The latter ensures the Courant–Friedrichs–Lewy (CFL) condition, which is necessary for the solutions of a difference equation to converge to those of the hyperbolic PDE[45]. The condition states that the time step should be proportional to the space step, where the proportionality constant depends on the velocity magnitude[45]. The CFL condition is defined for hyperbolic PDEs, but the unsteady stokes limit makes the momentum equation a parabolic PDE, bringing the usage of the CFL condition into question. Nevertheless, we found that enforcing this condition stabilises the simulation.

```
event stability(i++, last) {
  dt = dtnext(timestep(uf, dtmax));
}
```

Running the simulation reveals a significant flow that develops due to the active stress, advecting the chemicals (figure 3.7). The fluid is out of equilibrium at all times, with the spatial pattern in the chemical concentration perpetually swishing about. Because

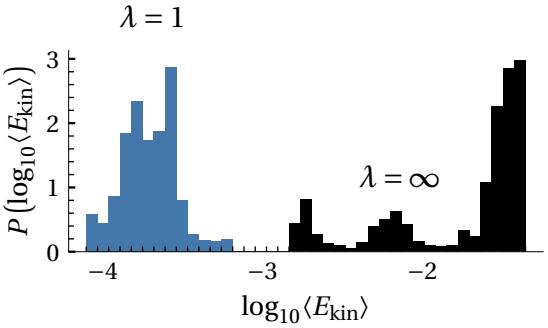

Figure 3.8: A histogram of the logarithm of the spatially averaged kinetic energy is shown for two cases: (blue, left) a friction term inhibits the accumulation of a net velocity, and (black, right) no such friction term is implemented, hence large mean velocities are observed. For simulation parameters refer to row 5 of appendix C.

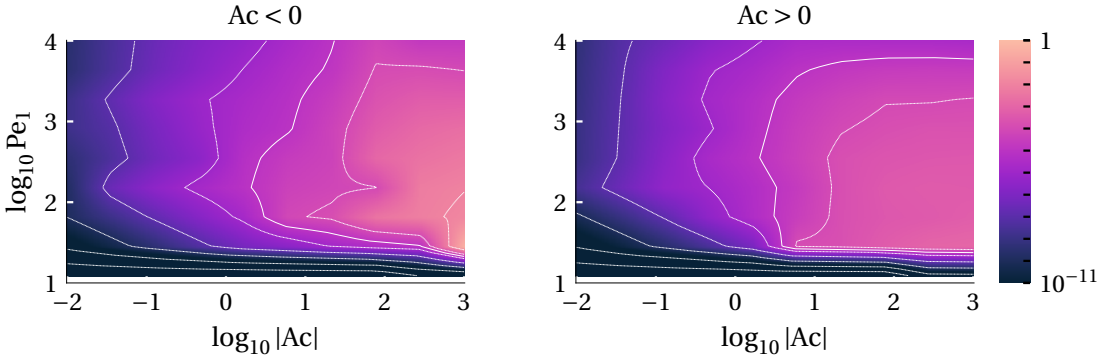

Figure 3.9: The mean velocity field $\langle \boldsymbol{u} - \langle \boldsymbol{u} \rangle_x \rangle_t$ is averaged over a duration of 100 time units and mapped for varying Péclet numbers Pe_1 and activity numbers Ac. A high value indicates a dynamic substrate, and a low value indicates that the substrate is static.

we take the unsteady stokes limit, we may infer that the flow and dynamics observed are at all times in the largest part due to the active stress generated at the moment observed, and not much prior.

One can calculate a histogram of the kinetic energy, that is, tally how often the system finds itself having a certain kinetic energy, in order to obtain more insight on the friction term. The kinetic energy is given by

$$E_{\mathrm{kin}} = \frac{\rho}{2} \int_\Omega |\boldsymbol{u}|^2. \tag{3.21}$$

A histogram of the logarithm of the spatially averaged kinetic energy succinctly displays the effect of the friction term (figure 3.8). With its inclusion, events of high kinetic energy are no longer observed, and the distribution of the kinetic energy is more concentrated about the mean. This is in contrast to the case without a friction term, where the kinetic energy distribution is concentrated at the high-end of the distribution.

This friction term only contributes significantly when the velocity is sufficiently large, which is not the case of interest in this work. As such, it can be regarded as a numerical technique to avoid extreme velocities. The large mean velocities that develop in the absence of friction obscure the more interesting dynamics present in both cases.

It was predicted that low Péclet numbers would not allow for a spatial pattern to develop, and that therefore no flow would ensue; it was also predicted that a low magnitude activity number |Ac| would not result in flow. Those predictions are shown to be accurate in figure 3.9, where the deformation tensor is shown for varying activity and Péclet numbers. Interestingly, the results are slightly dependent on the sign of the active force: more deformation occurs at for the same parameters for a negative sign on the active force.

Two notable behaviours were observed across a wide range of parameters. The first—where the active force has a positive sign—is shown in figure 3.7. The concentration of the first chemical forms short stripes oriented at random angles of width related to the chemical wavelength, perpetually moving around and morphing into and out of existence (see appendix E for a visualisation). This leads to an isotropic power spectrum with a peak at the chemical wavelength of the classical Brusselator.

In the case of a negative sign on the active force, rather than forming stripes in the chemical concentrations, the system appears to favour a regular grid of circular dips in the concentration (see appendix E for a visualisation). In the case that the chemical wavelength is such that this grid of circles does not fit an integer number of cells in the simulation domain, the circles that form are either too large, and tend to shrink, or too small, and tend to grow. In the second case, the circles move towards each-other and combine to form a larger circle. These circles are larger in diameter than the chemical wavelength dictates, and they soon begin to shrink. The area between them grows larger all the while, and new circles begin to form in the space between the existing, shrinking circles. Eventually, the initial grid of circular dips is restored, and the cycle repeats.

Viscoplastic rheology. With a sense of the system's behaviour for various combinations of activity and Péclet numbers, we continue to explore the remaining degree of freedom in the parameter space: the Bingham number. We restrict the analysis to a slice of this parameter space along the Ac—Bi plane by fixing the Péclet number at $\mathrm{Pe}_1 = 10^3$, since a number smaller than this would have a chemical wavelength too large, obscuring larger scale phenomena, and a number much larger would have spatial patterns not resolvable on the current mesh.

A parametric study of the spatio-temporal mean of the deformation tensor magnitude confirms the predictions made earlier—namely that for increased Bingham number, a larger activity number would be required for substantial deformation to occur (figure 3.10). The predicted arrested regime is present in the data, however precisely what threshold on the deformation tensor magnitude should count as arrested is left up to interpretation.

As for the scaling, a least-squares fit of the isoline marking $\langle \left|\mathbf{II}_{\dot\gamma}\right| \rangle = 1 \times 10^{-3}$ suggests the relation

$$\left|\mathrm{II}_{\dot\gamma}\right| \sim \begin{cases} \frac{|\mathrm{Ac}|^{1.2}}{\mathrm{Bi}} & \text{if } \mathrm{Ac} < 0, \\ \frac{|\mathrm{Ac}|^{1.1}}{\mathrm{Bi}} & \text{if } \mathrm{Ac} > 0. \end{cases} \tag{3.22}$$

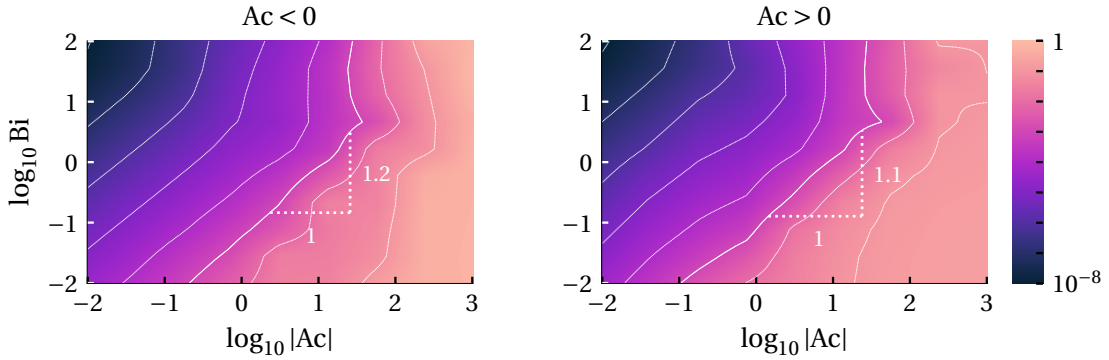

Figure 3.10: The spatio-temporal mean of the deformation tensor magnitude $\langle |\mathbf{II}_{\dot{\gamma}}| \rangle_{x,t}$ is shown for logarithmically increasing activity |Ac| and logarithmically increasing Bingham number Bi. Both signs of the active force are shown, negative on the left and positive on the right. The line for which $\langle |\mathbf{II}_{\dot{\gamma}}| \rangle = 1 \times 10^{-3}$ is drawn for both signs of the active force. The slope of this line is fitted, and is 1.1 for a positive sign and 1.2 for a negative sign.

This reveals a slight peculiarity: the relation depends on the sign of the active force. This difference is too slight to be claimed a feature of the system, and could likely arise due to numerical inaccuracies.

The introduction of a yield-stress results in a never ending cycle where the chemical sector develops independently to the mechanical sector on an unyielded domain, building up an active stress and eventually causing the fluid to yield. But before long the friction term dominates, allowing a portion of the fluid to return to an arrested state. The cycle then repeats, resulting in a dynamic sea of yielded and arrested domains perpetually flowing past each other. This is the case for a positive sign on the active force, and it largely resembles the Newtonian counterpart.

A histogram of the typical length of these arrested domains reveals a bimodal distribution when Ac < 0 and a trimodal distribution when Ac > 0 (figure 3.11). This complicated emergent phenomenon is a prime avenue for further research; we will only briefly touch upon it. As the behaviour appears fundamentally different between the choices of sign of Ac, it is best to separate the two.

Ac < 0. For low Bingham numbers, by far the most of the arrested domains are smaller than a fifth of the simulation domain in length. The next most frequent arrested domains nearly span the entire system, and decrease in length with increasing Bi. At a certain critical Bi (which appears to be a function of Ac), the distribution sharply divides between these two modes.

Ac > 0. A similar phenomenon occurs, but three modes are identified. The first mode is the most frequent and similar in nature to the Ac < 0 case. The second is also reminiscent of the previous case, but the typical domain length is significantly smaller. Interestingly, a third mode of opposite trend to the second manifests. The latter has domain lengths growing with increasing Bi, eventually saturating to the system size.

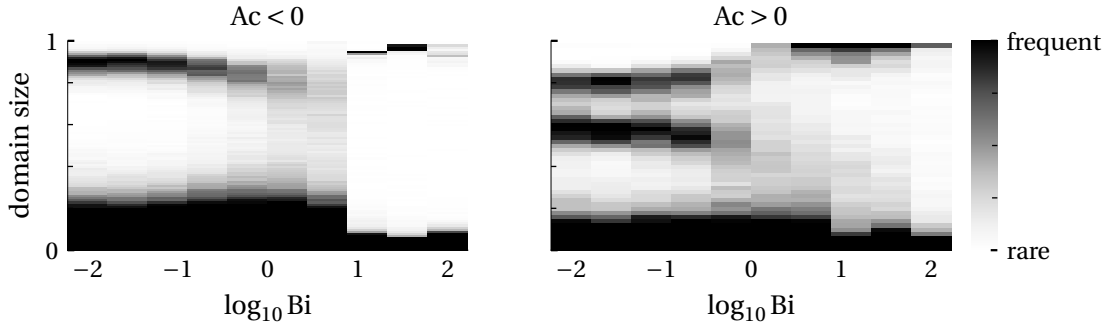

Figure 3.11: A histogram of typical linear lengths of the arrested domains, separated by thin flowing edges, is shown for increasing Bingham numbers. The colour scale has been truncated at the maximum value of the upper bands; the lowest band is two orders of magnitude larger. (left) A negative sign on the active force mostly gives rise to small domains, but also to domains nearly spanning the system size. The size of the latter decreases with increasing Bingham number, until a critical point, past which the most likely arrested domain sizes are either very small, or ones that span the entire system. The band of smaller sizes is attributed to dynamic periods in the evolution, while the other band is associated with relatively longer lived domains. (right) A similar relationship occurs for a positive sign on the active force, with the complication of a third band of arrested domain sizes. The latter grows in size with increasing Bingham number.

Two distinct kinds of chemical concentration patterns occur in the Bi—Ac space of positive active force depicted in figure 3.10—a highly structured, largely static, and anisotropic zig-zag stripe pattern; and a dynamic, isotropic sea of features of wavelength related to the chemical wavelength of the classic Brusselator. Examples from both classes of patterns are shown in figure 3.12. A transitional period exists between the two regimes, resembling the stripe pattern of the classical Brusselator (see appendix D). Defects in the stripe pattern appear more frequently in this transition region than in the high yield-stress regime at steady state, even though both contain similar defects at some point in the pattern's evolution. Interestingly, all of the observed patterns for a negative sign on the active force were roughly isotropic. The only deviation from isotropy seems to be the tendency to form hexagonal patterns rather than circles. This is not the case for a positive active force, as is evident in figure 3.12.

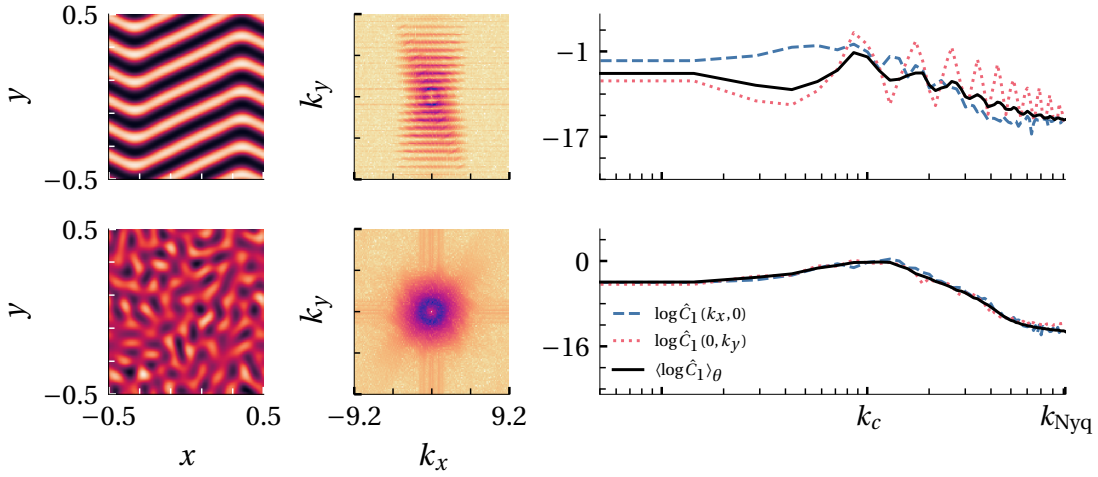

Figure 3.12: Each row shows: (left) the concentration of the chemical species at $t = 100$; (middle) the power spectrum of this concentration field, truncated at the Nyquist frequency, where the frequency has been rescaled by the chemical wavelength of the classical Brusselator; and (right) horizontal and vertical slices, and a radial average of this power spectrum. The two-dimensional spectrum has been tallied into bins of constant wavenumber. (top row) A high yield-stress results in a concentrated and anisotropic distribution of spatial wavelengths in the chemical concentration. (bottom row) A low yield-stress has a wide, spread out and isotropic distribution of spatial wavelengths. For simulation parameters refer to row 20 of appendix C.

Chapter 4

Deformable Interface Systems

Macroscopic living organisms largely settled on the cell as an atomic building block, likely as a means to organise biochemical reactions in space[46]. These cells contain a large number of coexisting systems that are all perpetually out of equilibrium. This dynamic soup of organelles—the cytoplasm—could perhaps in part be abstracted as an active reaction-diffusion-advection system. A simplified model of this extremely complicated system may shed light on cell migration, a process known to play an essential part in wound healing, immune response, embryonic development and cancer spreading[47–49].

The cell is but one example of a more general phenomenon of phase separation. It is likely that many processes in biological systems are dominated by the interplay between interfacial dynamics, and bulk forces and flows. The mere introduction of a finite domain separated from the bulk by an interface opens the door to countless phenomena, like swimming, fingering, rotation, and emergent behaviour in the case of a great number of domains.

Another example of an interface-bound active fluid is the *Drosophila* (a fruit fly) during its gastrulation phase, which exhibits pulsatory contraction cycles leading to whole-tissue extension[50]. Those contraction cycles arise from feedback between advection, contractility, and the binding of motor proteins and their activators, suggesting the use of a reaction-diffusion-advection model[50].

We will transition from a doubly periodic domain to a finite cell in a stepwise fashion, starting with a static substrate before re-introducing the mechanical sector and allowing the interface to deform. After having studied the interplay of a dynamic interface with the active fluid, we will incorporate surface tension into the model, finally forming a two-dimensional model of an active viscoplastic fluid confined to a deformable droplet.

In order to demonstrate the reaction-diffusion system's solution dependence on the boundary conditions, we briefly revisit the classical Brusselator system and let it

evolve in a static domain of circular geometry. The interface will be made deformable shortly. The confinement can be achieved by making the diffusion coefficients and the reaction rates spatially variable, and non-zero (but uniform) only within the circular domain. As will be shown momentarily, the solution of the chemical sector depends heavily on the boundary conditions.

The dimensionless Brusselator equations are adapted to take the circular domain into account by defining a smooth and continuous field which takes the value unity inside the domain, and zero everywhere else. This so called fraction field ϕ defines the domain and hence the interface; the location of the latter is determined by the equipotential $\{\boldsymbol{x}|\phi(\boldsymbol{x}) = 0.5\}$. One multiplies the diffusion coefficient, reaction terms and concentration fields by the fraction field to restrict the dynamics to the domain it represents:

$$\frac{\partial(\phi C_1)}{\partial t} = \boldsymbol{\nabla}\cdot\left(\phi\boldsymbol{\nabla}C_1\right) - \phi\left[(\mathrm{Da}_2+1)C_1 + C_1^2C_2 + 4.5\right], \tag{4.1}$$

$$\frac{\partial(\phi C_2)}{\partial t} = \boldsymbol{\nabla}\cdot\left(\phi D\boldsymbol{\nabla}C_2\right) + \phi\left[\mathrm{Da}_2C_1 - C_1^2C_2\right]. \tag{4.2}$$

The fraction field ϕ will be denoted `f` in Basilisk in order to comply with community standards. It is defined in the range $[0,1]$, so when performing operations that may bring its value outside this range, its value needs to be constrained accordingly. The program written in section 3.2 will be taken as a basis.

```
scalar f[]; // the fraction field

event init(i = 0) {
  ...

  foreach() {
    double r = L0/2.0 - 0.05*L0; // diameter just a bit smaller than L0
    f[]  = sq(x) + sq(y) < sq(r);
    C1[] = Da1 / Da4 * f[];
    C2[] = ((Da2 / Da1) * (Da4 / Da3) + 0.01 * noise()) * f[];
  }
}

event integration(i++) {
  dt = dtnext(DT);

  scalar r[], beta[];
  foreach() {
    r[]    = Da1 * f[];
    beta[] = (Da3 * C1[]*C2[] - Da2 - Da4) * f[];
  }
  face vector d1[];
  foreach_face() {
    d1.x[] = D1 * clamp(face_value(f, 0), 0, 1);
  }
  diffusion(C1, dt, d1, r, beta);
```

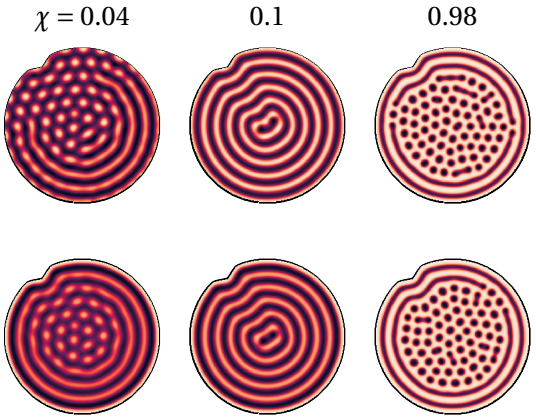

Figure 4.1: The classical Brusselator is integrated numerically on a circular domain with a small kink to demonstrate that the solution is negligibly dependent on the underlying grid. (top) The diffusion coefficients and reaction rates are zero everywhere outside the domain. (bottom) Additionally, it is enforced that the concentration fields vanish at the interface. This restricts the solution space; that is most apparent for $\chi = 0.04$, where stripes are formed instead of heaxagons near the boundary. For simulation parameters refer to row 6 of appendix C.

```
  foreach() {
    r[]    = Da2 * C1[] * f[];
    beta[] = - Da3 * sq(C1[]) * f[];
  }
  face vector d2[];
  foreach_face() {
    d2.x[] = D2 * clamp(face_value(f, 0), 0, 1);
  }
  diffusion(C2, dt, d2, r, beta);
}
```

The results are presented in figure 4.1, where it is clear that the boundary conditions have a dominant influence on the solution. We have additionally added a kink to the circular domain in order to demonstrate that the numerical solution does not strongly depend on the grid. A very small kink is sufficient to dictate the location of the defects in the solution, from which we infer that the symmetry is broken by the domain geometry and not by, for example, the aliasing caused by projecting a circle onto a Cartesian grid.

The chemical concentration is not necessarily zero on and near the domain boundary, and so the concentration field is not continuous across the boundary. This makes gradients of the concentrations numerically unstable. To avoid this issue, we enforce that the concentration must vanish at the boundary, and let the reaction-diffusion system give rise to a continuous solution. This restricts the solution space, and we illustrate the ensuing effect on the Brusselator system in figure 4.1. In Basilisk, this requirement is implemented by multiplying the concentration fields with the fraction field.

```
event integration(i++) {
  ...
  foreach() {
    C1[] = C1[] * f[];
    C2[] = C2[] * f[];
  }
}
```

Dynamic interface. We will now re-introduce the mechanical sector and allow the interface to be advected by the fluid, making it dynamic. Yet we should delay the inclusion of surface tension in order to investigate some features that do not depend on its presence. The fluid both inside the droplet and outside is Newtonian, for now. The droplet will shortly be made to be of a viscoplastic fluid.

As is typically the case for partial differential equations that model a physical system, the classical Brusselator PDEs are an approximation to some integral formulation regarding the chemical concentrations[51]. This approximation is generally a good one, but it fails near discontinuities of the integral formulation, which are typically present at interfaces between media. As such, these interfaces require special treatment in the numerical solver[51].

One approach to model the location and dynamics of interfaces is the volume of fluids (VOF) method, otherwise called the fractional marker volume method. For each material, each computational cell is said to have either zero volume, unity, or any value in between. The interface is identified by selecting the cells with a fractional volume, hence the name fraction field[51–54].

It may seem that the interface represented this way would end up being smeared or fuzzy, but a reconstruction step ensures that it is sharp[51]. The VOF method is not prohibitively expensive in two dimensions, but for three dimensional simulations one should consider using a recently developed sharp-interface method by Neiva and Turlier[55].

The `two-phase` solver implements the VOF method and exposes a particularly simple user interface. It is only necessary to define a distance function for the initial interface.

```
...

#define FILTERED 1 // smooths the fraction field and defines sf[]
#include "two-phase.h"

int main(int argc, char * argv[]) {
  ...
  mu1 = mu2 = 1.0 / Re;
}

event init(i = 0) {
  ...

  double r = 1.0;
  fraction(f, - sq(x) - sq(y) + sq(r));

  event("tracer_advection"); // this sets sf[]

  foreach() {
    double smeared_fraction = clamp(sf[], 0, 1);
    C1[] = (Da1 / Da4) * smeared_fraction;
    C2[] = ((Da2 / Da1) * (Da4 / Da3) + 0.01 * noise()) * smeared_fraction;
  }
}
```

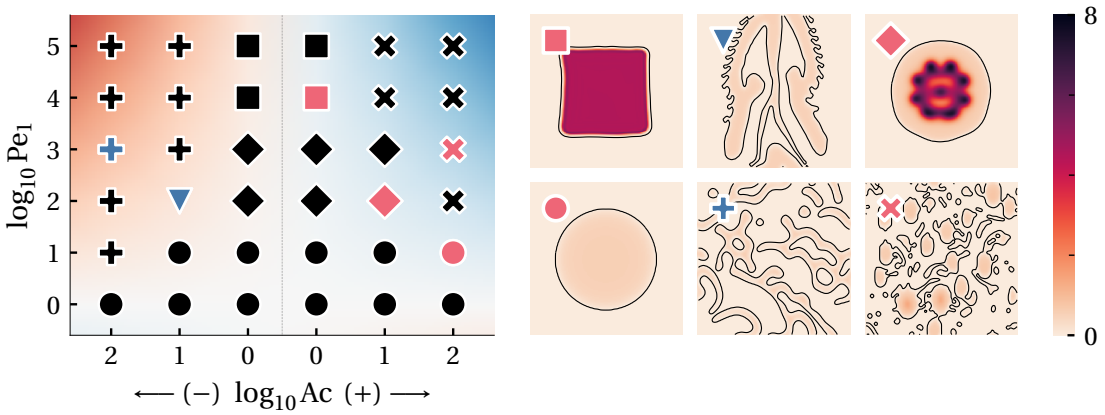

Figure 4.2: An overview of observed behaviours for different combinations of Péclet number and activity number (Ac). The negative activity numbers are plotted on the left and are marked in blue, and the positive on the right and in red. The combined "intensity" of the Péclet number and activity number are rendered in the background as an aiding visual cue. Examples are provided for notable behaviours: (square) sharp angles, (triangle) fingering, (diamond) pattern in concentration, (circle) circular, (plus) network, and (cross) spray. For simulation parameters refer to row 7 of appendix C.

Consider a diagram mapping the system's behaviour as a function of the Péclet number and the activity number. We can immediately predict that for low activity (small |Ac|), a negligible flow field will develop, if at all. Hence we predict that the chemicals will not be advected very much, the interface will not change much from its initial geometry, and the system will bear a resemblance to the classical Brusselator system on a circular domain.

Recall that if the flow field is zero everywhere, then the activity term amounts to a correction to the pressure, and the flow will remain irrotational forever (section 2.4). We can therefore expect the flow field to have little vorticity. A positive activity number would resemble a negative correction to the pressure and vice versa.

For small Péclet numbers, we expect that diffusion will dominate the system's behaviour. The chemical concentration should then be more or less uniformly distributed across the domain bounded by the interface. This prevents the active stress from driving the flow, as the activity term is proportional to the gradient of the chemical concentration. As the Péclet number increases, the chemical wavelength will decrease with the square root of the Péclet number (section 1.2.2). Eventually, the wavelength will be such that at least one node will fit in the circular domain. The chemical concentration will then develop a spatial pattern, giving rise to a non-zero gradient in the concentration and therefore a non-zero force due to the active stress.

A parameteric study of Pe$_1$ and Ac is shown in figure 4.2 and reveals numerous distinct phenomena with regards to the interface shape, behaviour, and the evolution of the chemical reaction occuring within it.

For low Péclet numbers we are comforted to see that the interface remains in its initial shape, and the chemical concentration is approximately uniform. As the Péclet number is increased while maintaining a small activity number, the interface remains

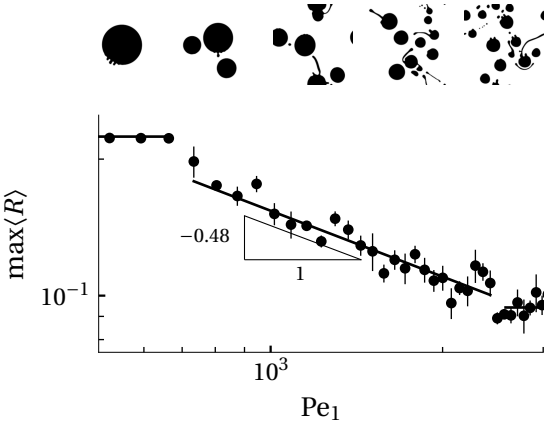

Figure 4.3: (top) Snapshots of the system for logarithmically increasing Péclet numbers. (bottom) The maximum of the average interface radius as a function of the Péclet number. This radius is calculated as the square root of the area bound by the interface, normalized so that a circular interface of area π is assigned unity radius. For simulation parameters refer to row 16 of appendix C.

roughly circular, but a spatial pattern develops in the concentration fields. Past a certain point, increasing the Péclet number even further ought to result in patterns of wavelength smaller than is resolvable in the simulation, and the concentration fields become uniform once more.

For high-magnitude activity numbers $|\mathrm{Ac}| \gg 1$ the interface undergoes a topology change, often many times over. A positive sign on the active force results in roughly circular blobs, while a negative sign results in a network-like structure. In almost all cases where a topology change occurs, the resulting domains have a uniform concentration of the chemicals.

It is in the intermediary regime that the most interesting behaviour is observed, where the active stress is strong enough to produce a flow, but not strong enough to cause a flow that is faster than the chemical reaction timescale. For a positive sign on Ac, a flower-like pattern emerges in the chemical concentration, and the droplet slightly deforms but generally maintains a circular shape. For a negative sign on the active force, fingering is observed. The slowly growing fingers are spaced regularly and have similar features.

Shifting the analysis to high-magnitude activity numbers $|\mathrm{Ac}|$, we can no longer expect the flow field to be weak and irrotational. Since there is no surface tension to hold the interface intact, eventually, a change of topology should occur. Since the chemical concentration is forced to vanish at the interface, a definite relation between the Péclet number and the size of the resulting interfaces is expected to manifest.

Since each of these resulting domains are strictly smaller than the initial domain, we can alternatively view these domains as having the same size as the initial domain, but with a decreased Péclet number. Therefore, we expect the interface to undergo a topology change many times over, until the resulting domains are similar to the case of the initial system if it were to have a smaller Péclet number. Such a diffusion dominated region will not be able to build up any further flow. All this implies the existence of stable interfaces containing an area of size related to the Péclet number, and indeed such a relation exists—see figure 4.3.

In fact, the relation mirrors the scaling of the chemical wavelength. There is plenty to suggest that the maximal interface size scales with this chemical wavelength:

$$\max R \sim \mathrm{Pe}_1^{-1/2}. \tag{4.3}$$

4.1 Surface Tension

In systems where the area spanned by the interface is large compared to the bulk that it separates, surface effects become dominant[56]. One such effect is surface tension. Molecules on the interface between two distinct fluids will form a different number of bonds on each side on average[56]. The difference in number of bonds results in the interfacial molecules having a higher energy than the bulk molecules, and consequently, it costs energy to form an interface[56].

An alternative interpretation of surface tension frames it as a force per length, here assigned the symbol σ. Basilisk includes a solver for surface tension effects, and it is this interpretation that is used in its implementation. The body force representing surface tension is then given by

$$\sigma \boldsymbol{f}_\sigma = \sigma \kappa \delta_s \boldsymbol{n}, \tag{4.4}$$

where κ is the mean curvature of the interface, σ is the constant surface tension coefficient, $\boldsymbol{n}$ is the unit vector normal to the interface, and where δ_s is the Dirac delta function centered on the interface.

With the rescaling

$$\boldsymbol{x} := R\overline{\boldsymbol{x}}, \quad t := \frac{R}{U}\overline{t}, \tag{4.5}$$

$$\boldsymbol{u} := U\overline{\boldsymbol{u}}, \quad p := \rho U^2 \overline{p}, \tag{4.6}$$

$$C_1 := C_0\overline{C}_1, \quad C_2 := C_0\overline{C}_2, \tag{4.7}$$

we obtain the dimensionless mechano-chemical system

$$\frac{\mathrm{D}\boldsymbol{u}}{\mathrm{D}t} = -\boldsymbol{\nabla} p + \frac{1}{\mathrm{Re}}\nabla^2 \boldsymbol{u} + \frac{1}{\lambda}\boldsymbol{f}_\lambda + \mathrm{Ac}\,\boldsymbol{f}_\alpha + \frac{1}{\mathrm{We}}\boldsymbol{f}_\sigma, \tag{4.8}$$

$$\boldsymbol{\nabla}\cdot\boldsymbol{u} = 0, \tag{4.9}$$

$$\frac{\mathrm{D}C_1}{\mathrm{D}t} = \frac{1}{\mathrm{Pe}_1}\nabla^2 C_1 - (\mathrm{Da}_2 + 1)C_1 + C_1^2 C_2 + 4.5, \tag{4.10}$$

$$\frac{\mathrm{D}C_2}{\mathrm{D}t} = \frac{1}{\mathrm{Pe}_2}\nabla^2 C_2 + \mathrm{Da}_2 C_1 - C_1^2 C_2. \tag{4.11}$$

Here, the independent parameters are the dynamic pressure $\overline{p} := p/U^2\rho$, the Reynolds number $\mathrm{Re} := RU\rho/\mu_0$, the Weber number $\mathrm{We} := RU^2\rho/\sigma$, the dimensionless chemical concentrations $\overline{C}_{1,2} := C_{1,2}/C_0$, the dimensionless friction relaxation time $\overline{\lambda} := \lambda U/R$, and the dimensionless activity parameter $\mathrm{Ac} := \alpha C_0^2/\rho U^2$.

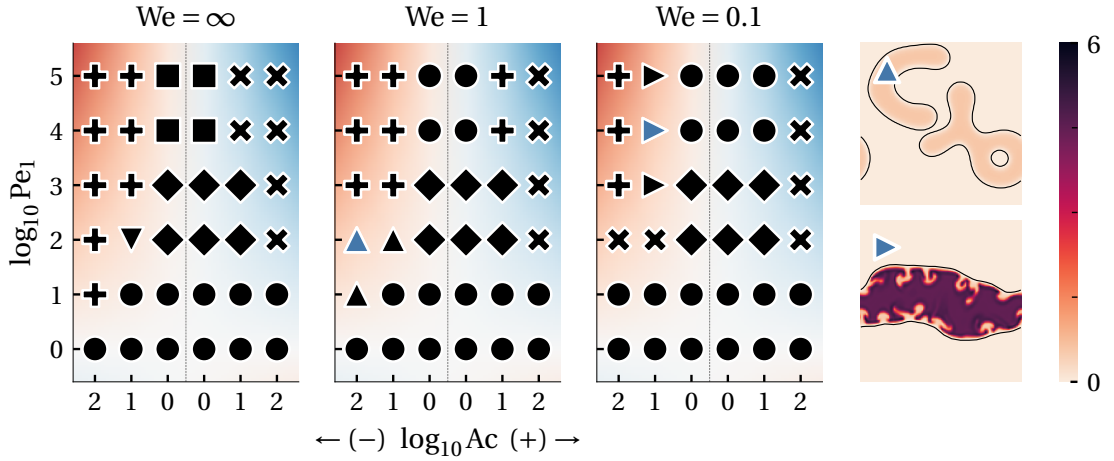

Figure 4.4: An overview of observed behaviours for different combinations of Péclet number and activity number (Ac), for three distinct Weber numbers. This is a continuation of figure 4.2. Examples are provided for notable behaviours: (up triangle) non-circular droplets, (right triangle) snaking, a finite-size effect. The other markers are exhibited in figure 4.2. For simulation parameters refer to row 8 of appendix C.

To implement surface tension in the simulation, we make use of the `tension` header, for which we must provide the constant surface tension coefficient for each fraction. Recall that we initialise the simulation with a single fraction `f`.

```
#include "tension.h"

int main(int argc, char * argv[]) {
  f.sigma = 1.0 / We;
  ...
}
```

The effect of surface tension on an interface is such that the energetically preferred configuration is that which minimises the length spanned by the interface[57]. In two dimensions, the shape which has the smallest ratio of boundary to area is the circle, hence, under no additional influence, a disc is the energetically preferred geometry of a given fluid fraction.

In the presence of other forces, the fraction may deviate from the ideal geometry of a disc. But the effect of surface tension is a stabilising one, and the stronger the surface tension, the less likely it is that the fraction geometry will deviate from a disc. The breakup into smaller domains depicted in figure 4.3 is an extreme example of such a deviation, which at one point resulted in a topology change in the fraction.

The stabilising effect of surface tension is evident in figure 4.6, in which it is shown that a change in topology is inevitable for a large enough active force. But increasing the relative importance of the surface tension (decreasing the Weber number) defers this inevitability to an even larger force. For an infinitesimally small Weber number, the surface tension would be so strong that if the other parameters were finite, the interface would never deviate from a perfect circle. It is in the intermediate regime that interesting behaviour is expected.

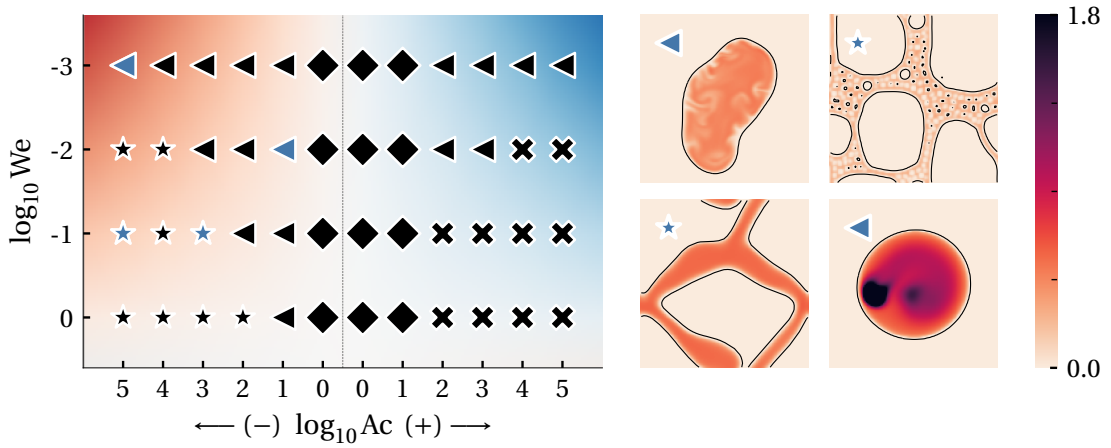

Figure 4.5: An overview of observed behaviours for different combinations of Weber and activity numbers. Examples are provided for notable behaviours: (left triangle) pulsating and motile droplet, (star) network structure, often with holes. The other markers are exhibited in figure 4.2. The chemical concentration values have been truncated from a maximal value of around 6 to better display notable features. For simulation parameters refer to row 9 of appendix C.

Figure 4.6: A thrice rendered binary map signifying whether a topological change has occured to the initial droplet, as a function of the Péclet and activity numbers (positive only). For sufficiently large activity and Péclet numbers, the droplet rips apart into smaller droplets. For simulation parameters refer to row 10 of appendix C.

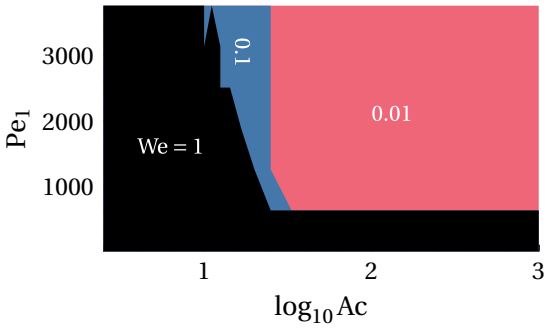

The parameteric study of Pe_1 and Ac is now repeated for varying We and is shown in figure 4.4. While in the absence of surface tension a tendancy existed for drastic and repeated topology changes in the interface, now these events are greatly oppressed. A parametric study of We and Ac is shown in figure 4.5, revealing new phenomena, the most notable of which is associated with intermediate Weber and activity numbers.

Viscoplasticity. Like surface tension, viscoplastic rheology is expected to have a stabilising effect on a droplet. Forces that are below the yield-stress criteria do not cause a flow, and as such the droplet is insensitive to such minute forces. Nevertheless, the chemical sector continues to evolve even in the absence of flow, and will eventually give rise to chemical gradients strong enough to surpass the yield-stress criteria.

In the parametric space spanned by Bi and Ac (considering only negative Ac), we observe three classes of behaviour (figure 4.7). The first is the most common: a tendency for the entire droplet to solidify, and remain solid regardless of the evolution of the chemical sector. Once the droplet remains rigid after the chemical sector has reached a steady-state, nothing remains in the system to break out of this state. This state is largely unlikely in the Newtonian limit $Bi \to 0$, but when droplet fragmentation

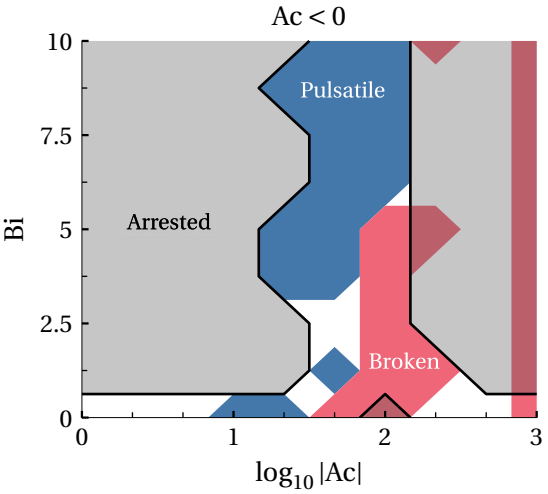

Figure 4.7: A parametric study of the Bi—Ac plane for Ac < 0. Three phenomena are singled out: (gray) the arrest of the droplet, in which no flow occurs and the interface is static; (blue) a pulsatile droplet, in which the droplet deforms at a definite temporal frequency; and (red) a change of topology in the droplet occurs. When a droplet is both pulsatile and fragmented, it is marked broken. All cases that do not fall into these categories are coloured white. For simulation parameters refer to row 15 of appendix C.

occurs, it is possible for the chemical wavelength to fall beyond the droplet diameter, thereby leading to static droplets. For all shown Bi, and up to a certain Bi, there is a band of Ac in which the droplet is not arrested and is rather dynamic.

These dynamic droplets form the second phenomenon: a periodically pulsating droplet with a net velocity in semi-random directions. This rich phenomenon is the subject of the next section.

Lastly, the final notable phenomenon is fragmentation. Since the resulting smaller droplets effectively have a smaller Péclet number, we refrain from analysing the dynamics any further and simply mark the droplet as broken.

4.2 Pulsating Motile Droplet

It has been shown by Camley *et al.* that a minimal model that abstracts the cell as a reaction-diffusion equation that evolves inside a droplet is capable of movement by virtue of surface tension, and picking a direction through polarisation by virtue of the chemical concentration gradient[58]. The authors argue that actin (a protein) polymerisation at the front of the cell and contraction driven by myosin (a motor protein) at the rear are the dominant forces acting on the cell's interface. Which part of the cell is made to be rear or front is determined by a wave pinning reaction-diffusion equation, resulting in a polar distribution of one of the morphogens (the polarity protein Rho GTPhase)[58,59]. That is, this protein tends to concentrate in half of the cell geometry, and the region of high concentration is the cell front. The authors do not consider advection effects inside the cell.

For a specific set of parameters, the cell motility model of Camley *et al.* results in a stationary state inside the cell, while the forces acting on the cell's interface propel it forward[58]. Such a stationary state may not be expected to occur often in the presence of advection and an active stress tensor. This section will exhibit our model's ability to represent motility via a mechanism distinct from that of Camley *et al.*

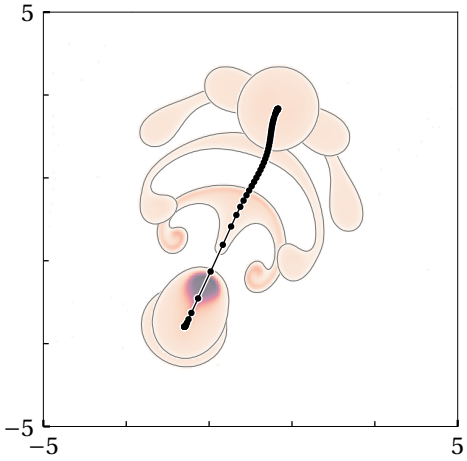

Figure 4.8: Snapshots of a periodically pulsating Newtonian droplet shown for the duration of one period (not at equidistant times). The droplet's trajectory is marked with a circle every 1/16 time units. For simulation parameters refer to row 12 of appendix C.

When the chemical wavelength is of the order of the droplet diameter, the system is expected to develop a single region of high concentration in C_1. This feature allows studying the essential properties of the system without the complications of a spatial pattern in the morphogen concentration. The active force will then stem from a single region inside the droplet, and will point outwards for negative Ac since the chemical concentrations are made to vanish at the droplet interface (recall $\boldsymbol{f}_a \propto \boldsymbol{\nabla} C_2$).

A realisation of this setup with We = 0.1 and Newtonian rheology is shown in figure 4.8. A region of high concentration slowly forms in C_1: a radial pattern decreasing in amplitude towards the periphery (figure 4.9). At the same time, a concentric ring pattern forms in C_2. The product of C_1 and the ring pattern in the gradient of C_2 forms the active force, which inevitably overpowers the surface tension, pushing outwards in all directions. In the presence of minute fluctuations, the symmetry breaks in a random direction and the interface gives, starting a brief positive feedback loop where C_1 and C_2 are advected in the same direction, increasing the overlap of the concentrated spot of C_1 with the ring pattern of $\boldsymbol{\nabla} C_2$.

This brief positive feedback loop between the active force and advection effects accelerates the droplet in the direction of the bulge, causing it to travel a distance of several radii. This burst also causes the droplet to suddenly become long and thin, mixing the chemicals and settling on a geometry in which highly concentrated regions cannot occur in the chemicals. This weakens the active force, allowing surface tension to dominate again, so that the droplet slowly returns to the shape of a circle. The cycle then repeats (key moments are shown in figure 4.9).

The pulsatory behaviour only manifests for a short range of activity and Weber numbers, but is of a constant pulsation frequency for that range of activity numbers (figure 4.10). This suggests that the pulsation frequency is determined by the relative strength of the surface tension, but not by the strength of the active force. The activity number is just required to be large enough to deform the interface, but not so large so as to break it. Otherwise, it is not surprising that a stronger surface tension gives rise to a faster pulsation cycle, as the droplet is able to return to its initial shape more quickly in that case.

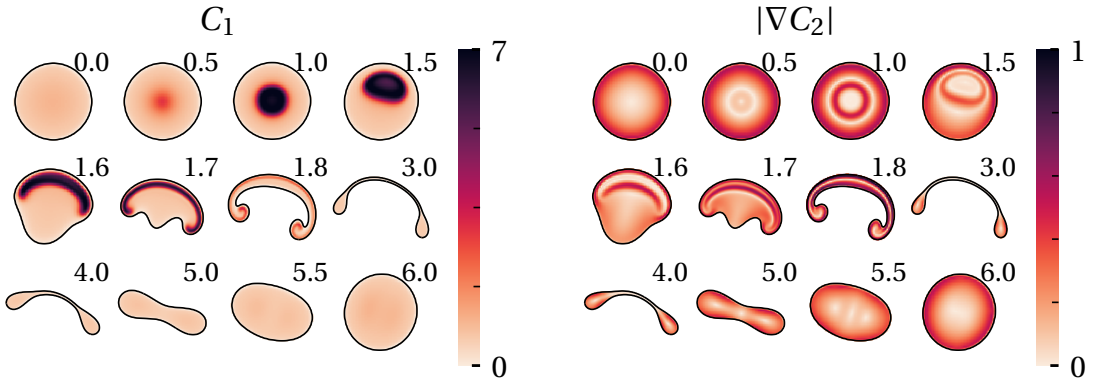

Figure 4.9: Snapshots in time of the droplet at activity number Ac = −50 depict one full pulsation cycle, for which the concentration of the first chemical species is shown (left), alongside the magnitude of the gradient of the second (right). ($t = 0$, relative) The cycle begins with $|\nabla C_2| \approx 0$ at the center of the droplet and a roughly uniform and low in value distribution of C_1. Since $\boldsymbol{f}_\alpha \propto \nabla C_2$, the interface is roughly stationary. ($t \approx 0.5$) C_1 accumulates in a concentrated spot at the center. ($t \approx 1.0$) A ring-like pattern develops in C_2, and the concentrated spot of C_1 is fully developed. A ring of ∇C_2 overlaps with a high-value region of C_1. ($t \approx 1.5$) the active force $\boldsymbol{f}_\alpha \propto C_1 \nabla C_2$ is strong enough to distort the interface, bulging outwards and further increasing the aforementioned overlap, triggering a rapid elongation of the interface. ($t \approx 3$) The chemical sector cannot sustain a region of high concentration for such a thin geometry, and so surface tension dominates again. ($t \approx 6.0$) Surface tension has restored the circular shape of the droplet, and the cycle repeats. For simulation parameters refer to row 12 of appendix C.

The dominating and competing effects in this cycle are the surface tension and active stress, hence a scaling analysis is warrented. Ignoring all other effects, a comparison of the two forces

$$\mathrm{Ac}\, C_1 \nabla C_2 \sim \frac{1}{\mathrm{We}} \kappa \delta_s \boldsymbol{n}, \tag{4.12}$$

leads to the order of magnitude relation

$$\kappa \sim \mathrm{Ac}. \tag{4.13}$$

Figure 4.10: The mean curvature of the droplet is measured across time, and the power spectrum of the resulting signal is shown for increasing activity number (left) and increasing surface tension importance (right). Harmonics are visible since the signal is not a perfectly sinusoidal. For simulation parameters refer to rows 12 and 24 of appendix C.

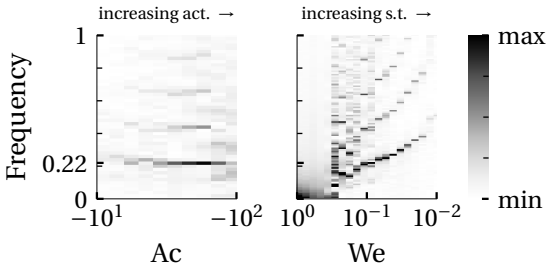

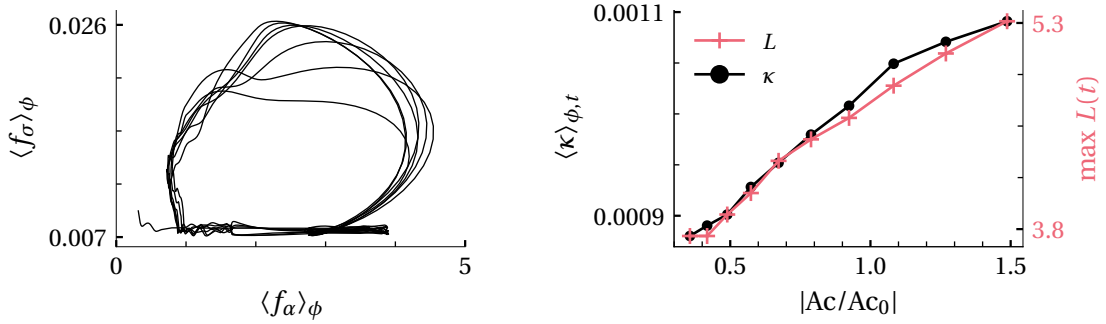

Figure 4.11: (left) The local curvature of the droplet is averaged over the interface and plotted against the mean magnitude of the active stress. (right) The temporal average of the droplet-average surface tension force magnitude is shown for increasing $|\mathrm{Ac}/\mathrm{Ac}_0|$, alongside the temoral maximum length of the droplet's bounding box. The curvature curve has an average slope of 2.0×10^{-4}; the length curve has an average slope of 1.4. For simulation parameters refer to rows 13 and 14 of appendix C.

Numerical simulations show that a definite relation of this form exists between the local curvature and the activity number (figure 4.11).

In the middle of the pulsation cycle, around 3 time units in figure 4.9, the droplet reaches maximum elongation. We can crudely approximate its shape as a long thin rod with round ends of length L and thickness R_1, where R_1 is also the radius of curvature of the round ends. Calling the droplet radius at rest R_0, we can claim the following by conservation of matter thus also of area

$$\pi R_0^2 \approx \pi R_1^2 + L R_1, \tag{4.14}$$

or

$$L \approx \frac{\pi (R_0^2 - R_1^2)}{R_1}. \tag{4.15}$$

But since $R_1 \ll R_0$, we may write

$$L \approx \frac{\pi R_0^2}{R_1} \sim \frac{1}{R_1}. \tag{4.16}$$

The average curvature of the interface $\langle \kappa \rangle_\phi$ is dominated by the far ends of the long shape, relating the local radius of curvature at the ends to the average curvature, giving (see figure 4.11)

$$L \sim \langle \kappa \rangle_\phi \sim \mathrm{Ac}. \tag{4.17}$$

Curiously, the droplet tends to occasionally turn left or right with equal probability, mostly travelling straight ahead (figure 4.13). The tendancy to travel straight is likely

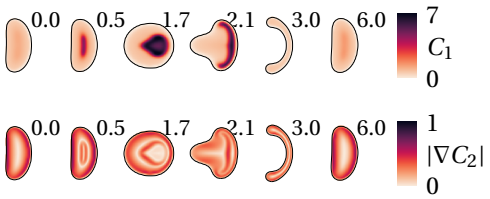

Figure 4.12: Continuation of figure 4.12 for a viscoplastic droplet. Note the inhibition of a return to circular shape due to arrest of the droplet. This less symmetric shape leads to a preferred direction for the subsequent pulsation. For simulation parameters refer to row 17 of appendix C.

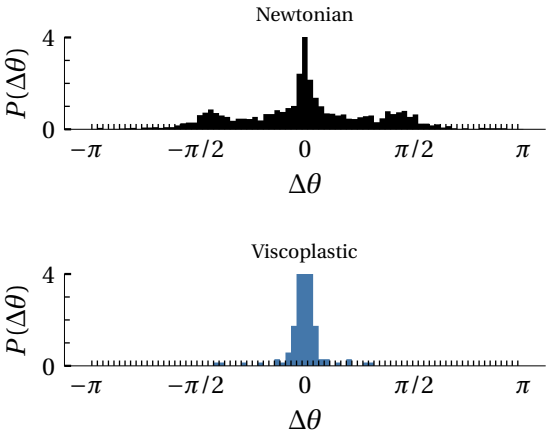

Figure 4.13: The probability of change of direction is shown for one Newtonian (top) and one viscoplastic (bottom) pulsatory droplet. The former mostly travels straight but sometimes makes a right or left turn with equal probability, while the viscoplastic droplet maintains the same direction of travel for many periods in a row. Both graphs have been truncated; the Newtonian case peaks at a value of 7.3, and the viscoplastic at 20. For simulation parameters refer to row 17 of appendix C.

due to weak flow in the same direction inside the droplet, which advects the chemical pattern as it forms. And the left and right turns appear to be due to the chemical pattern forming before the droplet has returned to a circular shape, so that the pattern develops in an ellipsoid that has its major axis aligned perpendicularly to the direction of travel.

A similar effect is certainly dominant in the case of viscoplastic droplets (figure 4.12), which for certain yield-stress and activity combinations, tend to travel straight ahead indefinitely (figure 4.13). A direct consequence is that such viscoplastic motile droplets travel much further than their Newtonian counterparts.

To conclude, it is fascinating that an active droplet under the influence of but the leading order terms of the active stress gradient expansion displays such rich phenomena. This minimal model gave rise to a pulsatory motile droplet, and the addition of viscoplasticity stabilised the dynamics to the effect of the droplet being able to travel indefinitely in a single direction.

Chapter 5

Conclusion

In this work we explored the dynamics of an incompressible two-dimensional active fluid of viscoplastic rheology, both on a periodic domain and confined to a droplet having surface tension, by constructing a direct numerical simulation using the open-source PDE solver Basilisk. To the extent of our knowledge, a direct simulation of such a system does not exist in literature. Even when restricting oneself to Newtonian rheology, a plethora of distinct phenomena resulted from the coupling of the Brusselator reaction-diffusion model with the mechanics of fluid flow. These include fragmentation, network structures, pulsations, motile droplets, pattern formation in the chemical concentration different to the static substrate case, stable non-circular droplet shapes, phase-separation dynamics, and more. And indeed, the complication of viscoplasticity resulted in dynamics not observed in the Newtonian case, such as pulsatory motile droplets that can maintain their direction of travel across many pulsations.

We provide a didactic and accessible presentation of the simulation implementation to support comprehension and complement the existing documentation of the excellent Basilisk solver. As the latter implements a highly domain specific language, invariably some unique conventions in the language design become a point of struggle for new users. Care has been taken to elaborate on such pain points, so as to form a complete and educational example for the construction of a Basilisk program.

The two-dimensional nature of the model developed here requires interpretation in order to justify its application to a physical system. It has not been the focus of this thesis to provide the connection to a physical system, but rather the focus has been to develop a minimal model to facilitate emergent phenomena. Nevertheless, this model and the simulation program that implements it both are readily modifiable to accommodate a closer connection to physical systems. One particular research avenue appears promising: cell motility and locomotion. In that scenario, one would consider this model to represent the contact layer of the cell with the substrate, such that the interface bound domain in the model would correspond to the cell membrane.

The reaction-diffusion system can be substituted for other reactions that may be more representative for this application. This demonstrates a key strength of the approach taken in developing this model: the ease with which one can prototype adjustments that would otherwise require large-scale revisions in implementation.

Many phenomena have been observed but were out of scope for the present work. Those include the bimodality of arrested domain length distribution in the active fluid, the splitting of droplets into smaller, similarly dynamic ones, the formation of stable and static droplets of non-circular geometry, finger formation, and the formation of flower-like patterns in the chemical concentration. Each of these would make for interesting follow up works. One could also implement elasticity in the model, to bring it even closer to the realm of biology, or study different chemical reactions to the same effect. Moreover, it would prove interesting to study clusters formed of a large number of motile droplets, which would perhaps give rise to unique emergent phenomena.

When exploring the large parameter space of this system, we opted to consider pairs of parameters at a time, fixing one member at the most dynamic or interesting value and substituting it for another parameter for consideration. This funnel led to the detailed exploration of a pulsatory motile droplet, but it is clear that many more phenomena are accessible with different parameter choices. For brevity, those phenomena have been mentioned in passing only (but representations of these parameter subspaces are provided in appendix D).

It is fascinating that such a rich spectrum of life-like behaviour emerges from a minimal model concerning but the leading order terms in the gradient expansion of the active stress.

Bibliography

[1] R. Hoyle, *Pattern formation: an introduction to methods* (Cambridge University Press, 2006).

[2] M. Golubitsky and I. Stewart, *The symmetry perspective : from equilibrium to chaos in phase space and physical space*, eng, Progress in mathematics vol. 200 (Birkhäuser, 2002).

[3] R. K. Yadav and J. Bloxham, "Deep rotating convection generates the polar hexagon on saturn", Proceedings of the National Academy of Sciences **117**, 13991–13996 (2020).

[4] M. Rietkerk and J. van de Koppel, "Regular pattern formation in real ecosystems", Trends in Ecology & Evolution **23**, 169–175 (2008).

[5] A. M. Turing, "The chemical basis of morphogenesis", eng, Philosophical transactions of the Royal Society of London. Series B, Biological sciences **237**, 37–72 (1952).

[6] H. Nakao and A. S. Mikhailov, "Turing patterns in network-organized activator–inhibitor systems", Nature Physics **6**, 544–550 (2010).

[7] H. Othmer and L. Scriven, "Instability and dynamic pattern in cellular networks", Journal of Theoretical Biology **32**, 507–537 (1971).

[8] R. Schnabel, M. Bischoff, A. Hintze, A.-K. Schulz, A. Hejnol, H. Meinhardt, and H. Hutter, "Global cell sorting in the c. elegans embryo defines a new mechanism for pattern formation", Developmental Biology **294**, 418–431 (2006).

[9] F. A. Bignone, "Structural complexity of early embryos: a study on the nematode caenorhabditis elegans", eng, Journal of biological physics **27**, 257–283 (2001).

[10] S. Popinet, *Basilisk: a free software for partial differential equations on adaptive cartesian meshes*, Source code, Version 25-02-26. Successor to Gerris, developed for multiphase flows, fluid dynamics, and environmental modeling. Includes adaptive mesh refinement and validated solvers for Saint-Venant equations, compressible flows, and non-Newtonian fluids., 2025.

[11] A. M. Turing and P. T. Saunders, *Morphogenesis*, eng, Collected works of A. M. Turing (North-Holland, Amsterdam, 1992).

[12]C. W. WARDLAW, "A commentary on turing's diffusion-reaction theory of morphogenesis", New Phytologist **52**, 40–47 (1953).
[13]B. N. Belintsev, "Dissipative structures and the problem of biological patter formation", Soviet Physics Uspekhi **26**, 775 (1983).
[14]B. Peña and C. Pérez-García, "Stability of turing patterns in the brusselator model", Phys. Rev. E **64**, 056213 (2001).
[15]S. A. Newman and R. Bhat, "Activator-inhibitor dynamics of vertebrate limb pattern formation", eng, Birth defects research. Part C. Embryo today **81**, 305–319 (2007).
[16]M. P. Harris, S. Williamson, J. F. Fallon, H. Meinhardt, and R. O. Prum, "Molecular evidence for an activator–inhibitor mechanism in development of embryonic feather branching", Proceedings of the National Academy of Sciences **102**, 11734–11739 (2005).
[17]Z. R. Sudderick and J. D. Glover, "Periodic pattern formation during embryonic development", en, Biochem Soc Trans **52**, 75–88 (2024).
[18]R. B. Bird, W. E. Stewart, and E. N. Lightfoot, *Transport phenomena*, 2nd ed. (J. Wiley, New York, 2002).
[19]P. Érdi and J. Tóth, *Mathematical models of chemical reactions: theory and applications of deterministic and stochastic models*, Nonlinear science: theory and applications (Manchester University Press, 1989).
[20]V. K. VANAG and I. R. EPSTEIN, "Cross-diffusion and pattern formation in reaction-diffusion systems", eng, Physical chemistry chemical physics : PCCP **11**, 897–912 (2009).
[21]W. A. Strauss, *Partial differential equations: an introduction*, 2nd ed. (Wiley, 2018).
[22]M. C. Cross and P. C. Hohenberg, "Pattern formation outside of equilibrium", Rev. Mod. Phys. **65**, 851–1112 (1993).
[23]A. Madzvamuse, H. Ndakwo, and R. Barreira, "Stability analysis of reaction-diffusion models on evolving domains: the effects of cross-diffusion", Discrete and Continuous Dynamical Systems **36**, 2133–2170 (2016).
[24]I. Prigogine and R. Lefever, "Symmetry breaking instabilities in dissipative systems. ii", eng, The Journal of chemical physics **48**, 1695–1700 (1968).
[25]I. Prigogine and G. Nicolis, "On symmetry-breaking instabilities in dissipative systems", eng, The Journal of chemical physics **46**, 3542–3550 (1967).
[26]I. R. Epstein, "The role of flow systems in far-from-equilibrium dynamics", Journal of Chemical Education **66**, 191 (1989).
[27]J. S. Bois, F. Jülicher, and S. W. Grill, "Pattern formation in active fluids", eng, Physical review letters **106**, 028103–028103 (2011).
[28]K. V. Kumar, J. S. Bois, F. Jülicher, and S. W. Grill, "Pulsatory patterns in active fluids", eng, Physical review letters **112** (2014).
[29]G. Salbreux, J. Prost, and J. F. Joanny, "Hydrodynamics of cellular cortical flows and the formation of contractile rings", eng, Physical review letters **103**, 058102–058102 (2009).
[30]O. Darrigol, *Worlds of flow: a history of hydrodynamics from the bernoullis to prandtl* (Oxford University Press, 2008).
[31]L. Euler, "Principes généraux du mouvement des fluides", Mémoires de l'Académie des Sciences de Berlin, 274–315 (1757).

[32]R. Feynman, R. Leighton, and M. Sands, *The feynman lectures on physics, vol. ii: the new millennium edition: mainly electromagnetism and matter*, The Feynman Lectures on Physics (Basic Books, 2011).
[33]A. Chorin and J. Marsden, *A mathematical introduction to fluid mechanics*, Texts in Applied Mathematics (Springer New York, 2000).
[34]G. K. Batchelor, *An introduction to fluid dynamics*, eng, 1st Cambridge mathematical library ed., Cambridge mathematical library (Cambridge University Press, Cambridge ; 2000).
[35]P. Chaikin and T. Lubensky, *Principles of condensed matter physics* (Cambridge University Press, 2000).
[36]A. Bray, "Theory of phase ordering kinetics", eng, Physica A **194**, 41–52 (1993).
[37]L. Meissner and J. M. Yeomans, "An introduction to phase ordering in scalar active matter", eng, The European physical journal. ST, Special topics (2024).
[38]J. Prost, F. Jülicher, and J.-F. Joanny, "Active gel physics", eng, Nature physics **11**, 111–117 (2015).
[39]E. Sackmann, F. Keber, and D. Heinrich, "Physics of cellular movements", Annual Review of Condensed Matter Physics **1**, 257–276 (2010).
[40]P. Saramito, *Complex fluids : modeling and algorithms*, eng, 1st ed. 2016., Mathématiques et Applications, 79 (Springer International Publishing, Cham, 2016).
[41]N. J. Balmforth, I. A. Frigaard, and G. Ovarlez, "Yielding to stress: recent developments in viscoplastic fluid mechanics", Annual Review of Fluid Mechanics **46**, 121–146 (2014).
[42]C. Beverly and R. Tanner, "Numerical analysis of three-dimensional bingham plastic flow", eng, Journal of non-Newtonian fluid mechanics **42**, 85–115 (1992).
[43]T. C. Papanastasiou, "Flows of materials with yield", eng, Journal of rheology (New York : 1978) **31**, 385–404 (1987).
[44]J. Bezanson, A. Edelman, S. Karpinski, and V. B. Shah, "Julia: a fresh approach to technical computing", SIAM Review **59**, 65–98 (2017).
[45]C. A. d. Moura, C. S. Kubrusly, C. A. de Moura, and C. S. Kubrusly, *The courant-friedrichs-lewy (cfl) condition: 80 years after its discovery*, eng, 1. Aufl. (Birkhäuser, Boston, MA, 2013).
[46]A. A. Hyman, C. A. Weber, and F. Jülicher, "Liquid-liquid phase separation in biology", Annual Review of Cell and Developmental Biology **30**, 39–58 (2014).
[47]N. O. Winkler, O. M. Drozdowski, F. Ziebert, and U. S. Schwarz, *Active gel theory for cell migration with two myosin isoforms*, 2025.
[48]R. Alert and X. Trepat, "Physical models of collective cell migration", Annual Review of Condensed Matter Physics **11**, 77–101 (2020).
[49]D. Bray and J. G. White, "Cortical flow in animal cells", Science **239**, 883–888 (1988).
[50]Y. Maroudas-Sacks and K. Keren, "Mechanical patterning in animal morphogenesis", Annual Review of Cell and Developmental Biology **37**, 469–493 (2021).
[51]J. M. Hyman, "Numerical methods for tracking interfaces", eng, Physica. D **12**, 396–407 (1984).
[52]R. Scardovelli and S. Zaleski, "Direct numerical simulation of free-surface and interfacial flow", Annual Review of Fluid Mechanics **31**, 567–603 (1999).
[53]S. Popinet, "An accurate adaptive solver for surface-tension-driven interfacial flows", Journal of Computational Physics **228**, 5838–5866 (2009).

[54]S. Popinet, "Gerris: a tree-based adaptive solver for the incompressible euler equations in complex geometries", Journal of Computational Physics **190**, 572–600 (2003).
[55]E. Neiva and H. Turlier, "Unfitted finite element modelling of surface-bulk viscous flows in animal cells", (2025).
[56]H. Bruus, *Theoretical microfluidics*, 1st, Oxford Master Series in Physics (Oxford University Press, Oxford, 2007).
[57]L. Landau and E. Lifshitz, *Fluid mechanics: volume 6*, v. 6 (Pergamon, 2013).
[58]B. A. Camley, Y. Zhao, B. Li, H. Levine, and W.-J. Rappel, "Crawling and turning in a minimal reaction-diffusion cell motility model: coupling cell shape and biochemistry", Phys. Rev. E **95**, 012401 (2017).
[59]M. C. Wigbers, T. H. Tan, F. Brauns, J. Liu, S. Z. Swartz, E. Frey, and N. Fakhri, "A hierarchy of protein patterns robustly decodes cell shape information", eng, Nature physics **17**, 578–584 (2021).
[60]G. W. Bluman and G. W. Bluman, *Symmetry and integration methods for differential equations*, eng, 2nd ed. 2002., Applied mathematical sciences ; v. 154 (Springer, New York, United States, 2002).

Appendix A

Linear Stability

Consider the steady-state of a reaction-diffusion system

$$D_n \nabla^2 C_n + f_n(C_1, \ldots, C_N) = 0. \tag{A.1}$$

If the system is at a homogeneous steady-state and is unstable to a plane wave perturbation of non zero spatial frequency, then there is the possibility for spontaneous pattern formation.

To analyze the stability of this system with regards to a small deviation from a homogeneous stationary state $(\overline{C}_1, \overline{C}_2)$, we will linearise it with regards to that state by defining $\delta C_1 \coloneqq C_1(\boldsymbol{r}, t) - \overline{C}_1$, $\delta C_2 \coloneqq C_2(\boldsymbol{r}, t) - \overline{C}_2$, which can be cast as

$$\frac{\partial \boldsymbol{\Phi}}{\partial t} = \mathsf{A}\boldsymbol{\Phi}, \tag{A.2}$$

with $\boldsymbol{\Phi} \coloneqq (\delta C_1, \delta C_2)^T$ and

$$\mathsf{A} = f_{ij} + D_{ij}\nabla^2 = \begin{pmatrix} f_{11} + D_1\nabla^2 & f_{12} \\ f_{21} & f_{22} + D_2\nabla^2 \end{pmatrix}. \tag{A.3}$$

Here, D_{ij} is are the diffusion coefficients, and the matrix formed by f_{ij} is the Jacobian of the reaction terms f_n, and is given by

$$f_{ij} = \left.\frac{\partial f_i}{\partial C_j}\right|_{(\overline{C}_1, \overline{C}_2)}. \tag{A.4}$$

We assume translational symmetry, and so the solution to this equation can be given as a superposition of harmonic modes[2]

$$\delta C_1 = \sum_{l=0}^{\infty} a_l^{(1)} e^{i\boldsymbol{k}_l \cdot \boldsymbol{r} - i\omega_l(\boldsymbol{k}_l)t} + c.c., \tag{A.5}$$

where c.c. stands for complex conjugate, and we include it to ensure that the chemical concentration is real valued. We can say the same for δC_2 (with different weights $a_l^{(2)}$). The dispersion law is found upon substitution of this solution and solving for ω_l as a function of $\boldsymbol{k}_l$.

To solve for a single harmonic mode, we note that any solution

$$\det(\mathsf{A}_l + i\omega_l \mathsf{I}) = 0, \tag{A.6}$$

where, defining $k^2 = |\boldsymbol{k}|^2 = k_x^2 + k_y^2$,

$$\mathsf{A}_l = \begin{pmatrix} f_{11} - D_1 k_l^2 & f_{12} \\ f_{21} & f_{22} - D_2 k_l^2 \end{pmatrix}. \tag{A.7}$$

We will again drop the subscript l. Since A is a 2×2 matrix, we may reduce the above to

$$\omega^2 - i(\operatorname{tr}\mathsf{A})\omega - \det\mathsf{A} = 0, \tag{A.8}$$

with as solution the dispersion relation of the linearised model

$$\omega(k^2) = \frac{i}{2}\left(\operatorname{tr}\mathsf{A} \pm \sqrt{\Delta}\right). \tag{A.9}$$

It is now possible to see why a one-component reaction-diffusion equation can never leave the spatially homogeneous state through an instability. One needs only to linearise the system, given by

$$\frac{\partial C}{\partial t} = D\nabla^2 C + f(C), \tag{A.10}$$

and solve for ω to obtain

$$-i\omega = -Dk^2 + f_1, \tag{A.11}$$

where f_1 is analogous to the Jacobian of the reaction term. It is evident that for $f_1 \leq 0$, the system is linearly stable. And otherwise, the system could only lose stability at zero wavenumber (which would classify it as type-III-s). But the exponential suppression grows as k^2, so by the time a wavenumber is reached that is meaningfully inhomogeneous, this suppression completely inhibits it. Hence, any spatial pattern that may develop is of long wavelength and slowly growing, rendering it homogeneous for all intents and purposes.

The Turing instability. The reaction-diffusion systems we will consider are those that are stable in the absence of diffusion ($D_i \to 0$). Turing predicted that diffusion can destabilise such a system[5]; to show this, we first write the criteria for linear stability in the absence of diffusion

$$f_{11} + f_{22} < 0, \tag{A.12}$$

$$f_{11} f_{22} - f_{12} f_{21} > 0. \tag{A.13}$$

Now in the presence of diffusion again, we see that since the diffusion coefficients are non-negative, we have that $\operatorname{tr} \mathsf{A} < 0$. Therefore, the reaction-diffusion system is destabilised if and only if $\det \mathsf{A} < 0$.

We conclude that since the trace of A is negative, the transition to instability happens when its determinant vanishes. This determinant is a parabola in k^2 that opens upwards. The first mode to flip the sign will then be at the minimum of this parabola. That mode is given by

$$k_c^2 = \frac{D_1 f_{22} + D_2 f_{11}}{2 D_1 D_2}. \tag{A.14}$$

We can therefore predict that the initial pattern that will grow exponentially in amplitude will have a spatial wavelength of

$$\boxed{\lambda_c = 2\pi \sqrt{\frac{2 D_1 D_2}{D_1 f_{22} + D_2 f_{11}}}.} \tag{A.15}$$

From equation (A.14) and since $k_c^2 \geq 0$, we know also that $D_1 f_{22} + D_2 f_{11} \geq 0$. And taking equation (A.12) into account, we infer that for the Turing instability to occur, it must hold that $\operatorname{sign} f_{11} = -\operatorname{sign} f_{22}$. This is most readily seen by contradictions arising from assuming otherwise. In combination with equation (A.12), this also implies that $\operatorname{sign} f_{12} = -\operatorname{sign} f_{21}$.

We now recall that for diffusive instability, the following must hold

$$\det \mathsf{A} = f_{11} f_{22} - f_{12} f_{21} - \frac{(D_1 f_{22} + D_2 f_{11})^2}{4 D_1 D_2} < 0, \tag{A.16}$$

which we can alternatively write as

$$D_1 f_{22} + D_2 f_{11} > 2\sqrt{D_1 D_2 (f_{11} f_{22} - f_{12} f_{21})}. \tag{A.17}$$

If the system is stable in the absence of diffusion, then this is a necessary and sufficient condition for the diffusive instability of a homogeneous steady state[22].

Observe that if one diffusion coefficient is a multiple of the other, $D_2 = \alpha D_1$, this condition becomes true at a critical diffusion coefficient $D_1^{\text{crit}} = 0$ when the Jacobian of the reaction terms is taken to be fixed. In that case, any strictly positive diffusion coefficient will allow for the Turing instability to occur.

Defining the two lengths $l_1 = \sqrt{D_1/|f_{11}|}$ and $l_2 = \sqrt{D_2/|f_{22}|}$, this condition can be written as

$$\frac{1}{2}\left(\pm\frac{1}{l_1^2} \mp \frac{1}{l_2^2}\right) > \sqrt{\frac{f_{11}f_{22} - f_{12}f_{21}}{D_1 D_2}}, \tag{A.18}$$

from which it is evident that one length must be sufficiently larger than the other, so as to satisfy the above condition. This condition is considered restrictive, but is relaxed when considering a non-stationary domain, which is in fact more representative for a biological system[23].

Since these lengths involve the diagonal elements of the reaction matrix, and the two rates have opposite signs, one is given the name *inhibitor* and the other *activator*. The rate of the inhibitor is negative and so inhibits its own growth, while the rate of the activator is positive and so it amplifies its growth. When $\operatorname{sign} f_{11} = \operatorname{sign} f_{21}$, the activator amplifies the production of both chemicals, and the inhibitor, likewise, affects both.

It has hereby been shown that diffusion can destabilise a reaction-diffusion system, given that its linear representation takes the form

$$\frac{\partial}{\partial t}\begin{pmatrix}\delta C_1 \\ \delta C_2\end{pmatrix} = \begin{pmatrix} f_{11} - D_1\nabla^2 & f_{12} \\ f_{21} & f_{22} - D_2\nabla^2\end{pmatrix}\begin{pmatrix}\delta C_1 \\ \delta C_2\end{pmatrix}, \tag{A.19}$$

with the conditions

$$\begin{aligned} \operatorname{sign} f_{11} \operatorname{sign} f_{22} &= -1, & f_{11} + f_{22} &< 0, \\ \operatorname{sign} f_{21} \operatorname{sign} f_{12} &= -1, & f_{11}f_{22} - f_{12}f_{21} &> 0, \end{aligned} \tag{A.20}$$

and

$$D_1 f_{22} + D_2 f_{11} > 2\sqrt{D_1 D_2 (f_{11}f_{22} - f_{12}f_{21})}. \tag{A.21}$$

The Brusselator. Only some choices of parameters will result in spontaneous pattern formation. We can use the linear stability analysis detailed previously to determine the criteria for which pattern formation occurs. The Brusselator equations are linearised around their trivial homogeneous steady state of $(\overline{C}_1, \overline{C}_2) = (\frac{a}{d}, \frac{d}{c}\frac{b}{a})$; assuming harmonic solutions, we get

$$\mathsf{A}_l = \begin{pmatrix} b - d - k_l^2 & \frac{c}{d^2}a^2 \\ -b & -\frac{c}{d^2}a^2 - Dk_l^2\end{pmatrix}, \tag{A.22}$$

but we will again drop the subscript l.

In the absence of diffusion, equation (A.12) implies that

$$b < \frac{ca^2}{d^2} + d, \tag{A.23}$$

$$a \neq 0. \tag{A.24}$$

Note that in the absence of diffusion, $\mathrm{tr}\,\mathsf{A} = a^2 c/d$. Therefore, now in the presence of diffusion, the condition that $\det \mathsf{A} > 0$ corresponds to

$$b \geq \left(\sqrt{d} + \frac{a}{d}\sqrt{\frac{c}{D}}\right)^2. \tag{A.25}$$

Appendix B

The Buckingham Pi Theorem

Let an arbitrary physical quantity q be represented by the n measurable quantities or parameters $W_1, W_2, \ldots, W_n$

$$q = f(W_1, W_2, \ldots, W_n). \tag{B.1}$$

These quantities are measured in terms of m fundamental dimensions $L_1, L_2, \ldots, L_m$. Unless otherwise stated, these will be taken to be $L_1 = m, L_2 = l, L_3 = t$ for mass, length, and time, respectively. It follows that the dimension of any of these quantities, say Z, can be written $[Z] = \prod_{i=1}^{m} L_i^{\gamma_i}$, for some real numbers $\gamma_1, \gamma_2, \ldots, \gamma_m$.

These numbers form a dimension vector $\boldsymbol{\gamma} = (\gamma_1, \gamma_2, \ldots, \gamma_m)^T$. The matrix with as columns the dimension vectors of all of the measurable quantities and parameters is called the dimension matrix $\mathsf{B} \in \mathbb{Q}^{m \times n}$. Each row of this matrix corresponds to a fundamental dimension, and each column to a measurable quantity or parameter.

The Buckingham Pi-theorem then states that we can write q in terms of $k = n - \text{rank}(\mathsf{B})$ dimensionless quantities. Let $\boldsymbol{x}^{(i)} = (x_{1i}, x_{2i}, \ldots, x_{ni})^T$, $i = 1, 2, \ldots, k$ represent the k vectors spanning the nullspace of B. Let $\boldsymbol{a}$ be the dimension vector of q. Finally, let $\boldsymbol{y}$ represent a solution of the system $\mathsf{B}\boldsymbol{y} = -\boldsymbol{a}$. At this point equation (B.1) can be written as

$$\pi = g(\pi_1, \pi_2, \ldots, \pi_k), \tag{B.2}$$

where $\pi = q \prod_{i=1}^{n} W_i^{y_i}$ and $\pi_i = \prod_{j=1}^{n} W_j^{x_{ji}}$. Note how f in equation (B.1) is a function of n variables, whereas g in equation (B.2) is a function of k variables. We have managed to represent the physical system in a way that requires knowing rank(B) less variables. For a proof, refer to[60].

B.1 Poiseuille Flow

Newtonian rheology. Starting with the equations for incompressible Newtonian fluids

$$\rho \frac{\mathrm{D}\boldsymbol{u}}{\mathrm{D}t} = -\boldsymbol{\nabla} p + \mu \nabla^2 \boldsymbol{u}, \tag{B.3}$$

$$\nabla \cdot \boldsymbol{u} = 0, \tag{B.4}$$

we should like to eliminate unnecessary parameters, or to write these equations in dimensionless form. This time, we will make use of the Buckingham Pi-theorem. This theorem allows us to obtain the dimensionless parameters of the system by solving a linear system of equations. For this, we must construct the so called dimension matrix.

The obvious characteristic dimensions are H [m] for the channel half-height, and U [$\mathrm{m\,s^{-1}}$] for the average velocity. We know from the analytical solution to the dimensional equations that if the flow is forced through the pipe with average velocity U, an average pressure gradient $\Delta P/L$ [$\mathrm{m\,kg^{-2}\,s^{-2}}$] will form. Since the geometry of the pipe is determined by its aspect ratio, it is not necessary to also consider the pipe length as a parameter.

The dimension matrix is then formed by considering the density ρ [$\mathrm{kg\,m^{-3}}$] and the viscosity coefficient μ_0 [$\mathrm{kg\,m^{-1}\,s^{-1}}$] as well:

	H	U	ρ	μ	$\Delta P/L$
kg	0	0	1	1	1
m	1	1	−3	−1	−2
s	0	−1	0	−1	−2

(B.5)

which yields the dimensionless groups

$$\pi_1 = \mathrm{Re} := \frac{\rho U H}{\mu}, \tag{B.6}$$

and

$$\pi = \frac{H \Delta P}{L U^2 \rho}. \tag{B.7}$$

Rescaling the pressure by $U^2\rho$, we get

$$\frac{\mathrm{D}\boldsymbol{u}}{\mathrm{D}t} = -\boldsymbol{\nabla} p + \frac{1}{\mathrm{Re}} \nabla^2 \boldsymbol{u}, \tag{B.8}$$

$$\boldsymbol{\nabla} \cdot \boldsymbol{u} = 0. \tag{B.9}$$

The Buckingham Pi theorem further allows us to write

$$\Delta P = U^2 \rho \frac{L}{H} f(\mathrm{Re}), \tag{B.10}$$

for some function $f(\mathrm{Re})$. This function can be found by noting that from the no-slip condition, we get that $C_2 = 0$, and $C_1 = \mathrm{Re} H \Delta P / L$, and that therefore

$$u_x(y) = \frac{\mathrm{Re}\Delta P}{2L}(2H - y)y. \tag{B.11}$$

Integrating this we obtain the following expression for the average flow rate

$$\Delta P = \frac{3U}{H}\frac{L}{H}\frac{1}{\mathrm{Re}}. \tag{B.12}$$

We see that if we were to obtain an average flow speed from this average flow rate, accounting for the rescaled pressure, we would find that $f(\mathrm{Re}) \propto \mathrm{Re}^{-1}$ in equation (B.10).

Viscoplastic rheology. We start with the equations for incompressible fluids

$$\rho \frac{\mathrm{D}\boldsymbol{u}}{\mathrm{D}t} = -\boldsymbol{\nabla} p + \boldsymbol{\nabla} \cdot \boldsymbol{\tau}, \tag{B.13}$$

$$\boldsymbol{\nabla} \cdot \boldsymbol{u} = 0, \tag{B.14}$$

with

$$\begin{cases} \boldsymbol{\tau} = 2\mu \left[1 + \dfrac{\tau_0}{\sqrt{2}\left|\mathbf{II}_{\dot{\gamma}}\right|^{1/2}} \right] \dot{\boldsymbol{\gamma}} & \text{when } |\mathbf{II}_\tau|^{1/2} \geq \tau_0, \\ \dot{\boldsymbol{\gamma}} = 0 \quad \text{otherwise.} \end{cases} \tag{B.15}$$

For this problem, the system is the same as was the case for the Newtonian Poiseuille flow, but with the complication of the yield-stress $\tau_0 [\mathrm{kg\,m^{-1}\,s^{-2}}]$. The corresponding dimension matrix B is

	H	U	ρ	μ_0	τ_0	$\Delta P/L$
kg	0	0	1	1	1	1
m	1	1	−3	−1	−1	−2
s	0	−1	0	−1	−2	−2

(B.16)

and the two vectors spanning its nullspace yield the following dimensionless groups: the Reynolds number $\mathrm{Re} := HU\rho/\mu_0$, the Bingham number $\mathrm{Bi} := H\tau_0/U\mu_0$, and the dynamic average pressure gradient $\Delta P/LU^2\rho$.

B.2 Reaction-Diffusion-Advection in a Droplet

The chemical sector is given by

$$\frac{\mathrm{D}C_1}{\mathrm{D}t} = D_1\nabla^2 C_1 + k_1 A - (k_2 B + k_4)C_1 + k_3 C_1^2 C_2, \tag{B.17}$$

$$\frac{\mathrm{D}C_2}{\mathrm{D}t} = D_2\nabla^2 C_2 + k_2 B C_1 - k_3 C_1^2 C_2, \tag{B.18}$$

where the reaction rates have units $[k] = (\mathrm{kg\,m^{-3}})^{1-n}\mathrm{s}^{-1}$, and n is the order of the chemical reaction.

And the mechanical sector is given by

$$\rho\frac{\mathrm{D}\boldsymbol{u}}{\mathrm{D}t} = -\boldsymbol{\nabla} p + \mu\nabla^2\boldsymbol{u} + \frac{1}{\lambda}\boldsymbol{f}_\lambda + \alpha\boldsymbol{f}_\alpha + \sigma\boldsymbol{f}_\sigma, \tag{B.19}$$

$$\boldsymbol{\nabla}\cdot\boldsymbol{u} = 0. \tag{B.20}$$

Besides the droplet radius R, the variables and parameters of the momentum equations are $U, \rho, \mu_0, \sigma, \kappa, \alpha, C_0, \lambda$, where the dimensions of each variable ν_i are

$$[\nu_i] = \mathrm{kg}^{\mathsf{B}_{1i}}\mathrm{m}^{\mathsf{B}_{2i}}\mathrm{s}^{\mathsf{B}_{3i}}, \tag{B.21}$$

and where B is

	R	U	ρ	μ_0	p	σ	κ	α	C_0	λ
kg	0	0	1	1	1	1	0	−1	1	0
m	1	1	−3	−1	−1	0	−1	5	−3	0
s	0	−1	0	−1	−2	−2	0	−2	0	1

(B.22)

This yields the following dimensionless groups: the dynamic pressure $\overline{p} := p/U^2\rho$, the Reynolds number $\mathrm{Re} := RU\rho/\mu_0$, the Weber number $\mathrm{We} := RU^2\rho/\sigma$, the dimensionless chemical concentration $\overline{C_0} := C_0/\rho$, the dimensionless friction relaxation time $\overline{\lambda} := \lambda U/R$, the dimensionless activity parameter $\mathrm{Ac} := \alpha C_0^2/\rho U^2$, and the dimensionless curvature $\overline{\kappa} := R\kappa$.

Appendix C

Simulation Parameters

Unless otherwise specified, the following values are to be taken:

Parameter	Value
Da_1	4.5
Da_2	7.38
Da_3	1
Da_4	1
Pe_2	$Pe_1/8$
Viscoplastic regularisation parameter m	1000

#	t_{end}	cells	L	R	Δt	Ac	We	Bi	Pe_1	λ
1	500	2^8	1		0.5				4096	
2	100	2^7	1		0.1				1000	
3	100	2^7	1		0.001	1000			1000	
4	100	2^7	1		0.001	1000			1000	1
5	1000	2^7	1		0.001	1000			1000	∞, 1
6	500	2^7	1	0.5	0.5				4096	
7	20	2^7	3	1	5×10^{-4}	$\pm[1,100]$			$[1,1\times10^5]$	
8	20	2^7	3	1	5×10^{-4}	$\pm[1,100]$	∞, 1, 0.1		$[1,1\times10^5]$	
9	20	2^7	3	1	5×10^{-4}	$\pm[1,1\times10^5]$	$[0.001,1]$		100	
10	20	2^7	3	1	5×10^{-4}	$[1,1000]$	∞, 1, 0.1		$[10,4000]$	
11	100	2^8	10	1	0.001	-50	0.1	1	100	1
12	50	2^8	10	1	0.001	$[-10,-100]$	0.1		100	1
13	30	2^8	20	1	0.001	-50	0.1		100	1
14	10	2^8	20	1	0.001	$[-50,-500]$	0.1		100	1
15	300	2^8	20	1	0.001	$[-1,-1000]$	0.1	0.678	100	1
16	15	2^8	1	0.25	0.01	100			$[100,7000]$	
17	10000	2^7	20	1	0.001	-20	0.1	0, 4.16	100	1
18	100	2^7	1		0.001	$[-0.01,-1000]$			$[1,1\times10^4]$	1
19	500	2^7	1		0.001	$\pm[0.01,1000]$		$[0.01,100]$	1000	1
20	500	2^7	1		0.001	0.01, 1000		0.01	1000	1
21	100	2^7	1		0.001	1000			1000	1
22	100	2^7	1		0.001	-100			200	1
23	100	2^7	1		0.001	-100			200	1
24	100	2^8	10	1	0.001	-50	$[0.1,1]$		100	1

Appendix D

Parameter Sweeps

D.1 Periodic Boundaries

D.1.1 Pe_1—Ac, Newtonian rheology

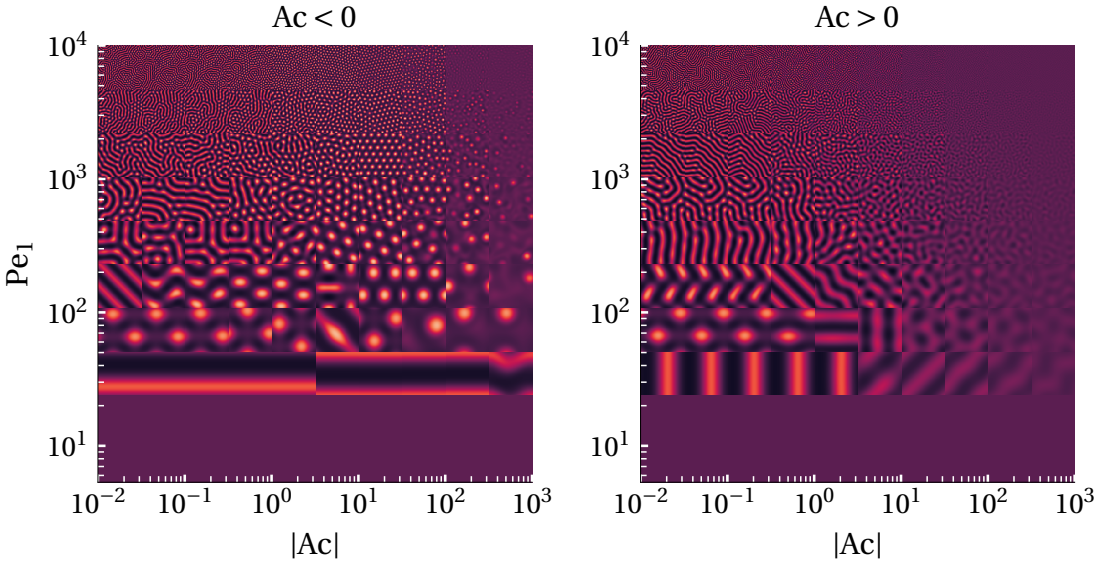

Figure D.1: Depicted: C_1 at the final timestep. For simulation parameters refer to row 18 of appendix C.

D.1.2 Bi—Ac

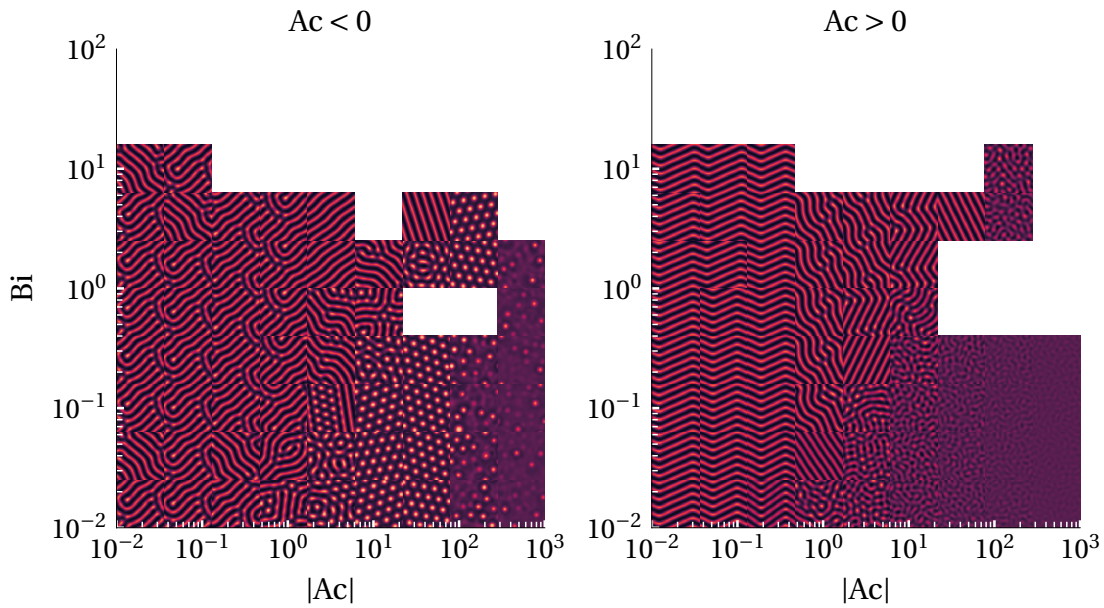

Figure D.2: Depicted: C_1 at the final timestep. For simulation parameters refer to row 19 of appendix C.

D.2 Droplet

D.2.1 Pe_1—Ac, $Ac > 0$, $We = \infty$

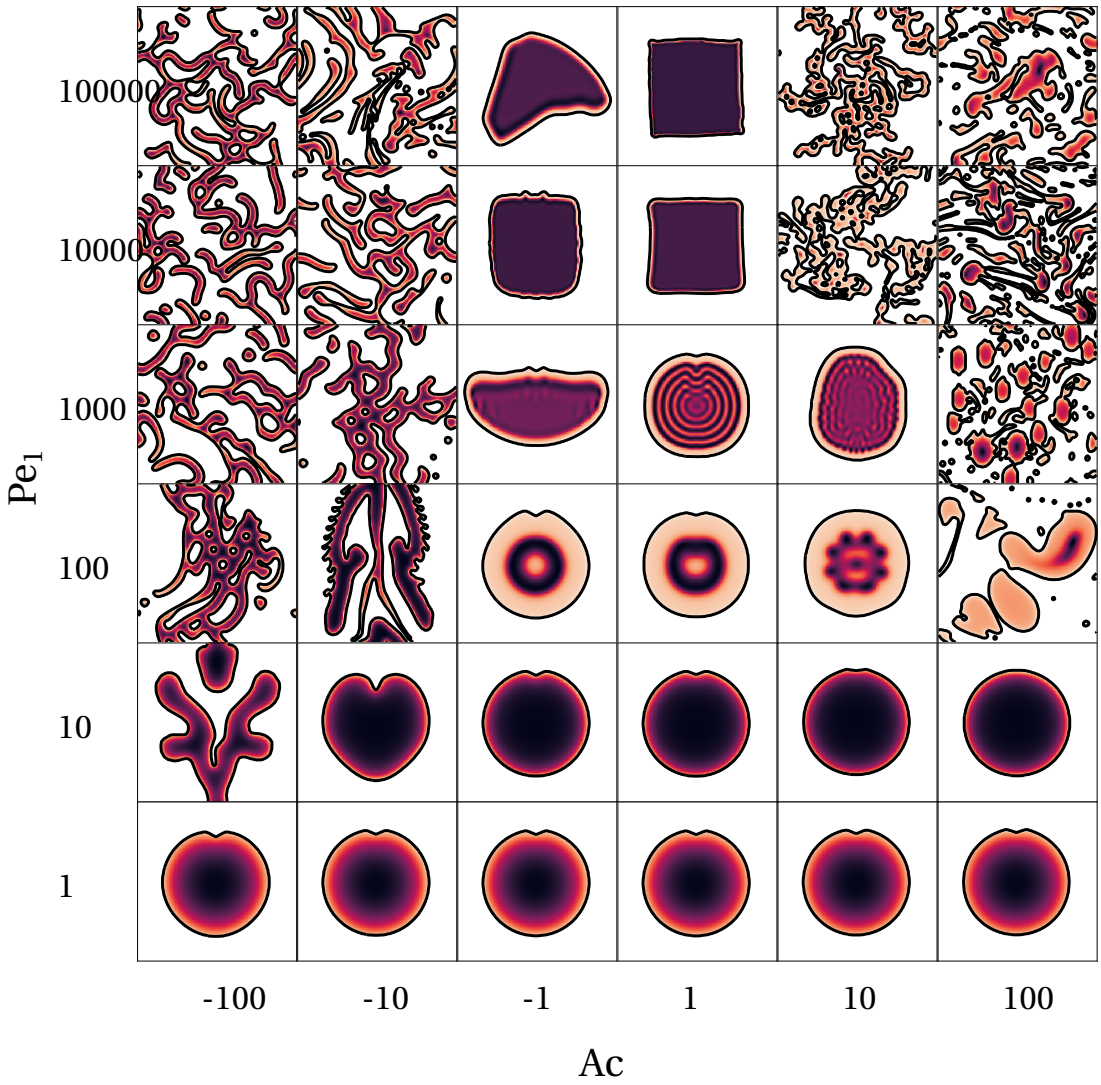

Figure D.3: Depicted: C_1 at the final timestep. For simulation parameters refer to row 8 of appendix C.

D.2.2 Pe_1—Ac, $Ac > 0$, $We = 1$

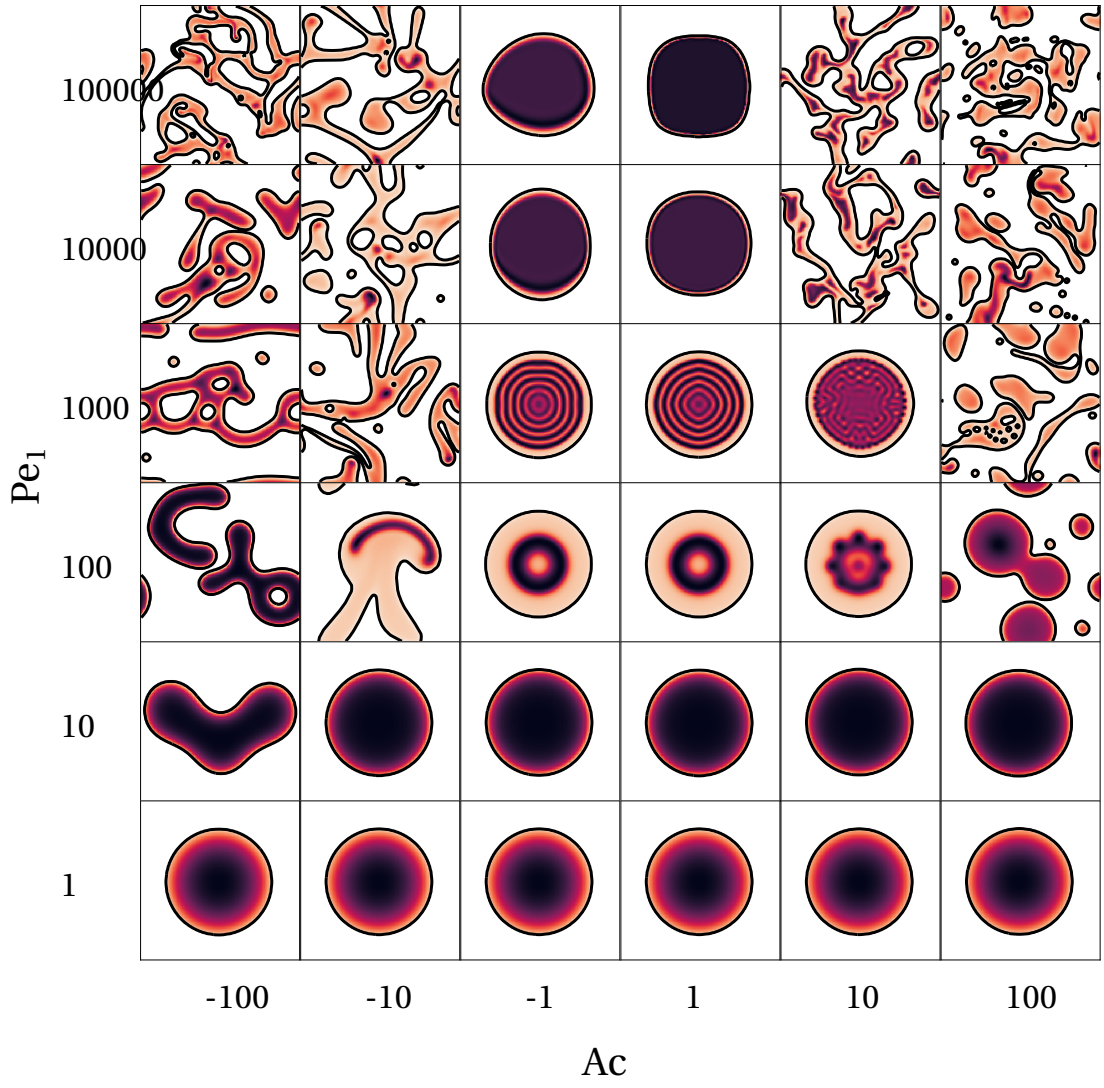

Figure D.4: Depicted: C_1 at the final timestep. For simulation parameters refer to row 8 of appendix C.

D.2.3 Pe_1—Ac, $Ac > 0$, $We = 0.1$

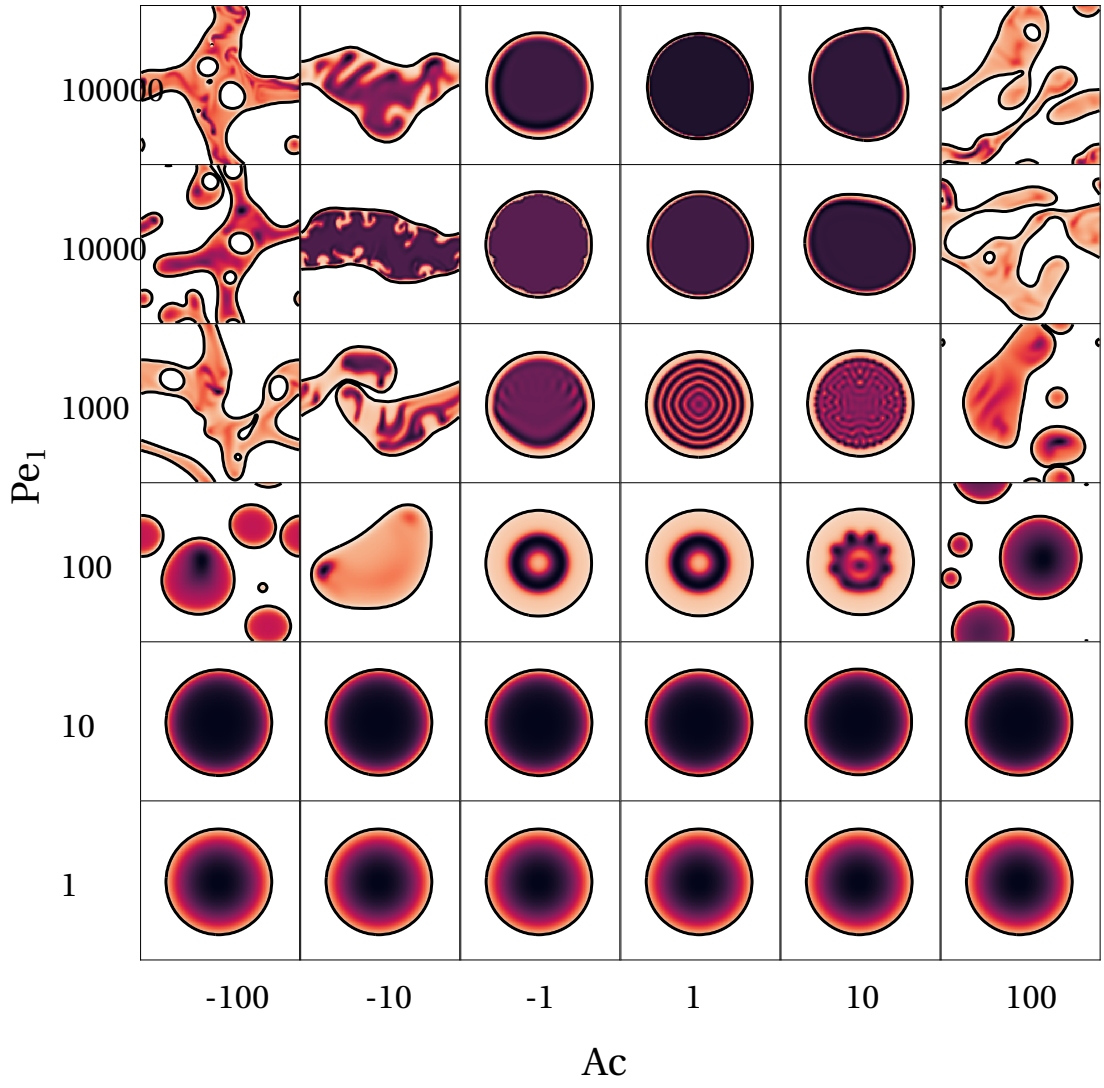

Figure D.5: Depicted: C_1 at the final timestep. For simulation parameters refer to row 8 of appendix C.

D.2.4 We—Ac, Ac > 0

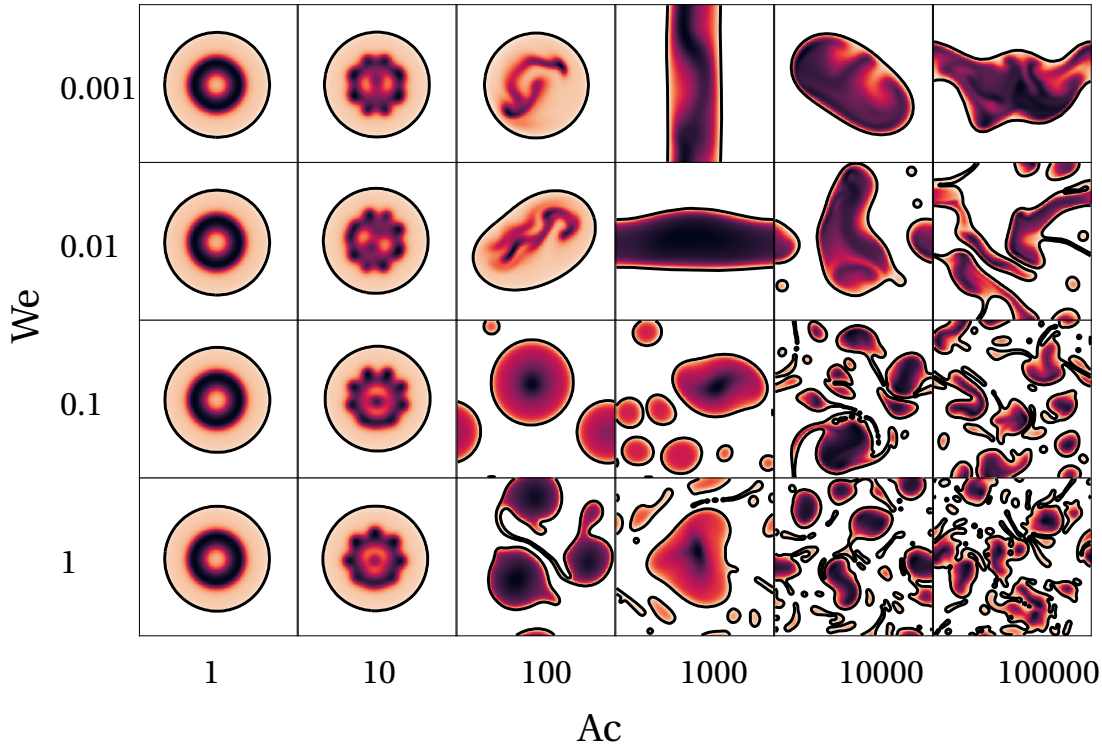

Figure D.6: Depicted: C_1 at the final timestep. For simulation parameters refer to row 9 of appendix C.

D.2.5 We—Ac, Ac < 0

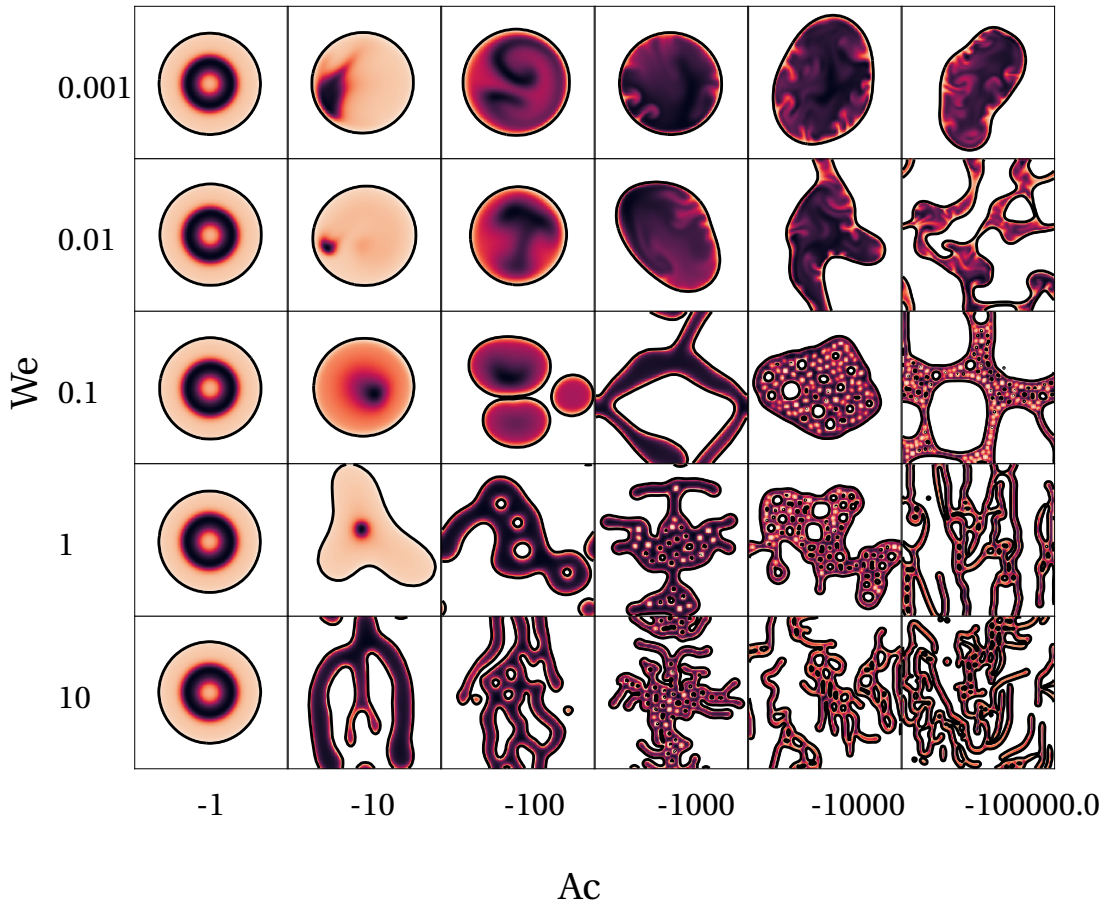

Figure D.7: Depicted: C_1 at the final timestep. For simulation parameters refer to row 9 of appendix C.

Appendix E

Extra Figures

E.1 Validation of Data Transfer Integrity

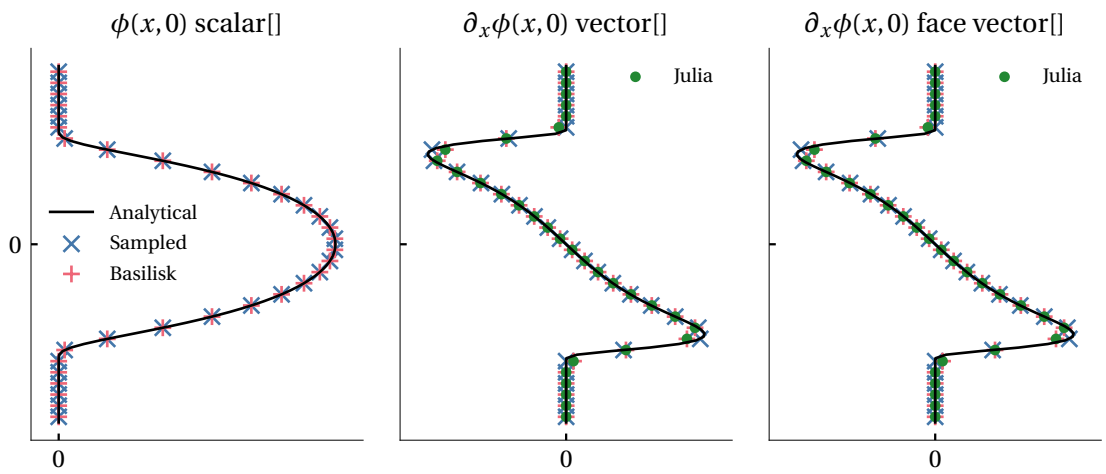

Figure E.1: (left) The cross-section of a 2D bump signal (black solid line), the signal sampled on the grid of Basilisk (red plus), the signal sampled on the same grid in Julia (blue cross). (middle) The gradient of the bump signal is calculated analytically (black solid line), by a second order accurate finite difference formulation using Basilisk (red plus), by a similar formulation using Julia (green dot), and the analytical solution sampled on the discrete grid used by Basilisk (blue cross). (right) Similarly, but using a face centered stencil.

E.2 The Classical Brusselator

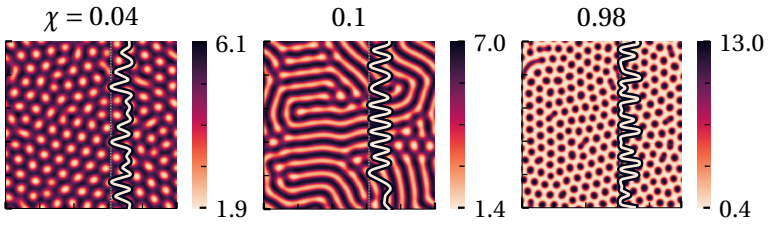

Figure E.2: The solution to the concenentration of the first morphogen for varying values of χ. From left to right, the solution takes the form of hexagons, stripes, and hexagons again. The critical parameter χ will henceforth be fixed at $\chi = 0.1$ unless otherwise stated. For simulation parameters refer to row 1 of appendix C.

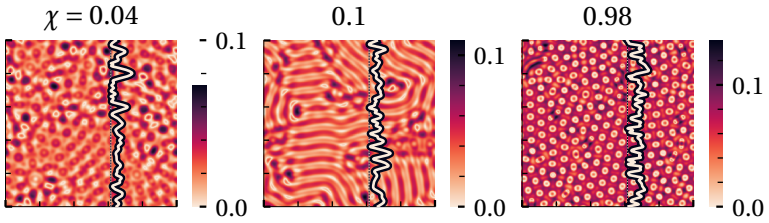

Figure E.3: The absolute difference between $\tilde{C}_1$ and $1 - \tilde{C}_2$ is shown for different values of χ. The tilde signifies that the field has been normalized. The value quantifies the error of the claim that C_2 is equal to C_1 up to normalization, which is around 10%.

E.3 Temporal Snapshots

E.3.1 Periodic Boundary Conditions

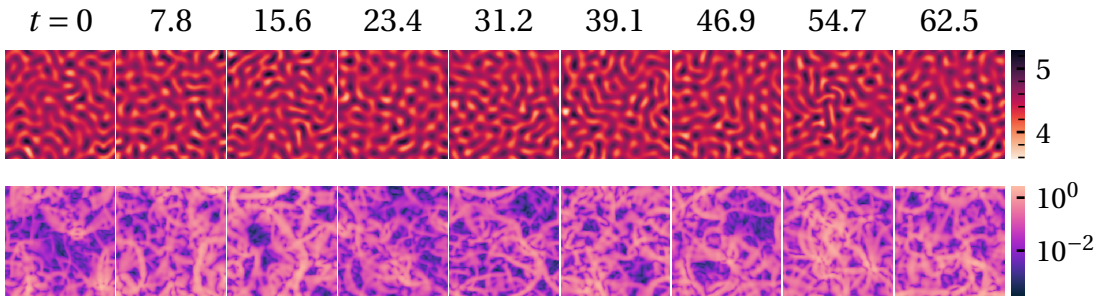

Figure E.4: For simulation parameters refer to row 21 of appendix C.

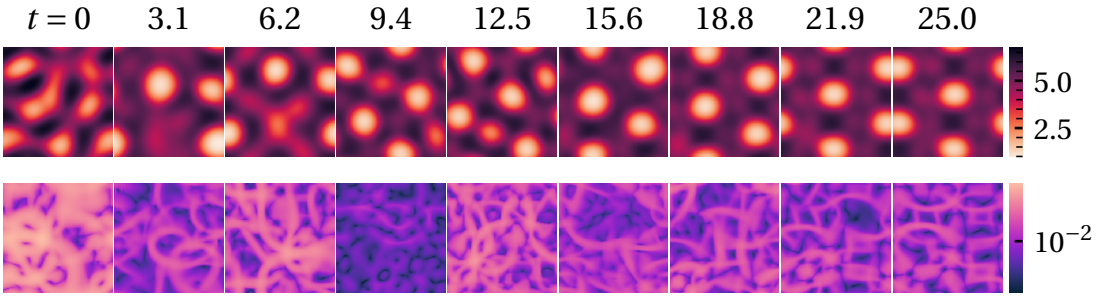

Figure E.5: For simulation parameters refer to row 22 of appendix C.

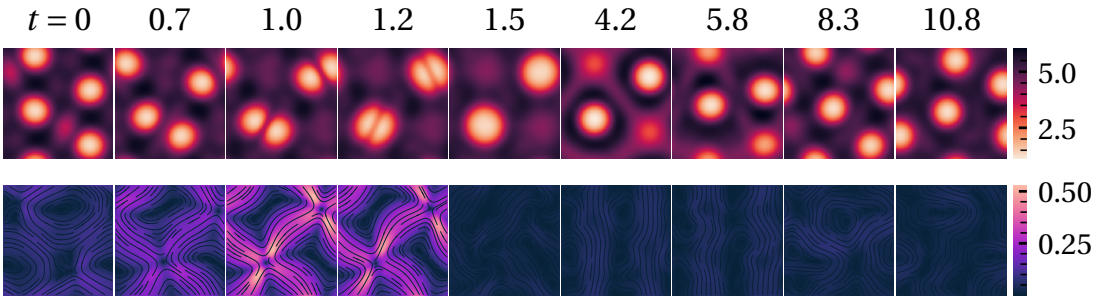

Figure E.6: For simulation parameters refer to row 23 of appendix C.

E.3.2 Motile Droplet

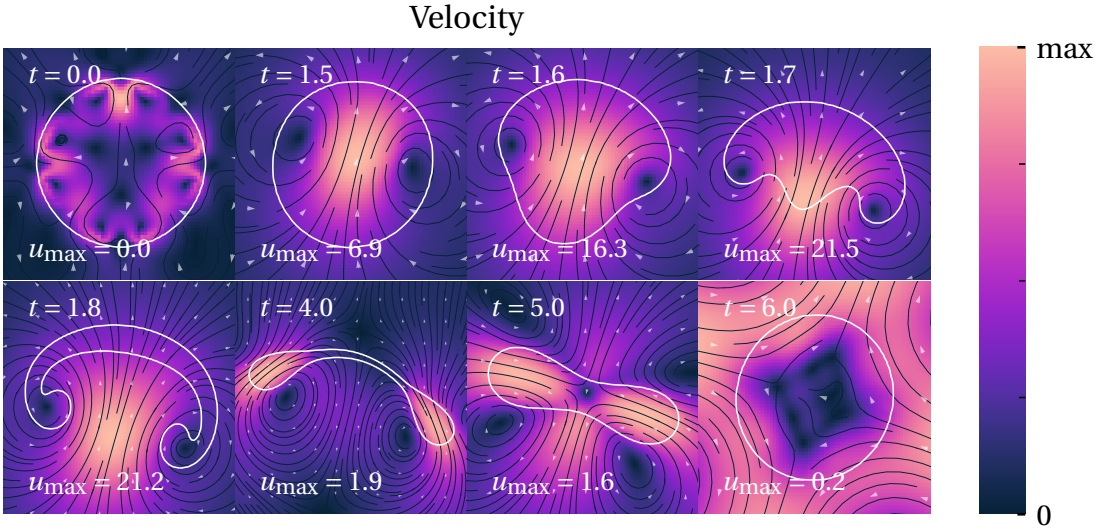

Figure E.7: The velocity field (with its mean subtracted per dimension) is depicted for one full pulsation cycle. For simulation parameters refer to row 12 of appendix C.

Appendix F

Basilisk C

A Basilisk program consists of an entry point, as is the case in C, declarations of variables and fields, and events. Variables are allocated memory automatically, so that the user only has to specify the type, name and value. An event consists of a trigger condition and a body, the former may depend on the iteration number or the simulation time.

In Basilisk, one may make use of a multitude of generic so called solvers. These are routines that solve a more general instance of the problem at hand. Examples include solvers that solve the Navier-Stokes equations, reaction-diffusion equations, and many others. Such a solver is used by including the appropriate header file and assigning values to variables defined in the solver.

We give a brief sketch of the anatomy of a Basilisk program, and detail a minimal subset of features necessary to implement the simulations that will follow.

```
#include "solver.h"

int main(int argc, char * argv[]) {
  init_grid(1 << 7); // 2^7

  // load parameters from argv
}

event init(i = 0) {
  // declare boundary conditions
  // set initial value to fields
}

event integration(i++) {
  // perform a calculation at each iteration
}

event final(t = end) {
```

```
  // save value of fields to disk
}
```

Basilisk supports three kinds of stencils for fields: centered stencils, where the field value is defined equidistant between four vertices (in two dimensions), face centered fields, where the value is defined equidistant between two vertices, and vertex centered fields, where the value is defined on a vertex.

Corresponding iterators are defined for all of these stencil types. Some iterators automatically cycle through permutations of `x` and `y` in specific cases. The conditions required for this to occur are: the code must be in the scope of a `foreach_dimension` loop, or a `foreach_face` loop, and the variable name must end with `_x` or `_y`. Each iterator exposes the coordinates `x` and `y` of the cell currently iterated upon.

```
scalar a[];
foreach() {
  a[] = ...;
}

vector u[];
foreach() {
  foreach_dimension() {
    u.x[] = function_defined_elsewhere_x(x, y);
    // automatically: u.y[] = function_defined_elsewhere_y(x, y);
  }
}

face vector uf[];
foreach_face() {
  uf.x[] = function_defined_elsewhere_x(x, y);
  // automatically: uf.y[] = function_defined_elsewhere_y(x, y);
}
```

The Basilisk preprocessor performs dimensional analysis on the variables declared in the program. This is done to enforce correctness and can be disabled, however, doing so is highly discouraged. Dimensions are assigned by providing an array of exponents of some set of base dimensions, which the user is free to choose so long as this is done in a consistent fashion. Here we will use SI units.

```
//                       [m,  s]
double distance     = 0 [1,  0];
double duration     = 0 [0,  1];
double acceleration = 0 [1, -2];
```

Events derive inspiration for their syntax from `for` loops in C. They consist of a name, a starting condition, a condition that must be true for the event to repeat, and an iteration operator. These conditions may depend only on the simulation time `t` and the iteration number `i`. An event returns the value zero by default. Should it be necessary, it is possible to halt the simulation by returning a value different from zero.

```
event name(t = 1; t <= 5; t += 1) {
  // every time step past t=1 and until t=5 inclusive
```

```
}

event name(t = 8)              // once at t=8
event name(i++)                // at every iteration
event name(t = 1; t *= 2)      // at t = 1, 2, 4, 8, ...
event name(t = {2.5, 4, 9.1}) // at t = 2.5, 4, 9.1
event name(t = end)            // once when the simulation is complete
```

Three types of boundary conditions have utility functions defined to declare them: `neumann`, `dirichlet` and `periodic`. One can refer to the boundary in question by the reserved keywords `left`, `right`, `top`, and `bottom`. We will only consider features related to two dimensional simulations; the reader may consult the Basilisk documentation for information that is omitted. It is possible to automatically select the tangent and normal directions of a vector field using, respectively, the notation `u.t` and `u.n`.

```
a[left] = dirichlet(val);
a[right] = neumann(val);

u.n[top] = dirichlet(0); // selects vertical component
u.n[left] = dirichlet(0); // selects horizontal component
u.t[top] = dirichlet(0); // selects horizontal component

periodic(left); // same as periodic(right), applies to all fields
periodic(top); // same as periodic(bottom)
```

We refer the reader to the Basilisk documentation for more information.